Politecnico di Torino

ScuDo
Scuola di Dottorato ~ Doctoral School
WHAT YOU ARE, TAKES YOU FAR

Doctoral Dissertation
Doctoral Program in Metrology (35^{th}cycle)

Ultrasound Drug Delivery through Functionalized Nanodroplets and Nanoparticles

By

Simone Galati

******

Supervisor(s):
Dr. Adriano Troia., Supervisor

Doctoral Examination Committee:
Prof. Giancarlo Cravotto, Referee, Università di Torino
Prof. Loredana Serpe, Referee, Università di Torino

Politecnico di Torino
2023

Declaration

I hereby declare that, the contents and organization of this dissertation constitute my own original work and does not compromise in any way the rights of third parties, including those relating to the security of personal data.

Simone Galati
2023

* This dissertation is presented in partial fulfillment of the requirements for **Ph.D. degree** in the Graduate School of Politecnico di Torino (ScuDo).

Acknowledgements

First and foremost, I express my sincere gratitude to my supervisor, Dr. Adriano Troia[1]. His continuous guidance, support, and patience have been invaluable to me during my PhD years. Even in moments of self-doubt, he has always encouraged me, and our constructive discussions have greatly aided in completing this project and fostering my growth as a scholar. I have greatly benefited from his extensive knowledge of the subject, amazing curiosity, and wealth of theoretical and practical expertise, which played a key role in shaping the idea behind this thesis.
I am also grateful to the university staff of the Metrology Ph.D Program at Politecnico di Torino, especially the coordinator of XXXV cycle, Prof. Marco Parvis[2]. He has often assisted me in tackling complex administrative issues.
Special thanks go to all my colleagues at the ML04 Advanced Materials Metrology and Life Sciences Department of INRiM, where the work was carried out. I am thankful to everyone who has joined me over the last three years and provided both scientific and personal support, even through simple laughs during lunch breaks.
Next, I want to express my appreciation to all my friends in Turin and around the world. Although it's difficult to name everyone, I want to thank you, the reader, for being there. It's often said that the journey matters more than the destination, more than its beginning and end, and my journey would not have been the same without you. Thank you for your friendship, for filling my days with good memories, for last-minute trips, or simply for sharing a beer. Everything is essential if done with sincerity and genuine friendship, even the smallest gesture.
Finally, I extend enormous gratitude to my Mom and Dad, Dario and Nonna Pina, for their unconditional love and support throughout this academic journey, and my life more generally. They have always trusted and encouraged me, even during my

[1]Ultrasounds & Chemistry Lab., Department of Advanced Materials and Life Science, I.N.Ri.M., Turin, Italy

[2]Department of Electronics and Telecommunications, Politecnico di Torino, Turin, Italy

darkest moments, and have shown me the other side of the coin when I couldn't. I could never have accomplished this without their guidance and support.

Abstract

Ultrasound (US) is a widely used diagnostic technique in the medical field, and in recent decades, it has also gained significant interest for therapeutic purposes. In particular, US has been shown to be effective for drug delivery due to its ability to provide better spatial confinement and reduce undesired side effects. In addition to that, phase-shift perfluorocarbon(PFC)-based formulations have been demonstrated to be promising US-sensitive platforms for controlled oxygen delivery to treat tissue hypoxia diseases. This has provided the basis for the synthesis of new oxygen delivery platforms, the oxygen-loaded nanodroplets (OLNDs), characterized by a PFC-based liquid core formulation. These new platforms have shown promising properties, including highly stability, bioinertness and biocompatibility, ease of preparation, and relatively low cost. Additionally, their nanosized dimensions enhance extravasation. The physical mechanism triggering the oxygen release by US is acoustic cavitation. In particular, interacting with the US field, OLNDs first undergo acoustic droplet vaporization (ADV), passing from liquid nanodroplets to gaseous microbubbles, and then acoustic cavitation. Cavitation is actually composed of two separate moments. As the bubbles are formed, they start growing until reaching their resonant sizes around which oscillate (stable cavitation) and release their content in a controlled way. If the acoustic pressure further increases, bubbles undergo a violent collapse (inertial cavitation). However, at present there is no complete characterization at a fundamental level of the different signals produced by US-activated sonocarriers. Therefore, the first aim of this PhD thesis is to obtain a metrological characterization of the cavitation phenomena induced by US through parallel investigation approaches.

In the first part, therefore, three different US-sensitive carriers were used, including two different PFP-based OLNDs using polyvinyl-alcohol (PVA) or chitosan as a polymeric shell, and zinc oxide nanoparticles (ZnO NPs) that behave as cavitation

nuclei for the formation of bubbles inside a liquid solution. A customized setup was developed to monitor the response to US stimuli of the carriers flowing inside a customized channel, through different sensors. A passive cavitation detector (PCD) provided information about cavitation, showing that the occurrence of both stable and inertial cavitation events in the presence of sonosensitive carriers enhanced compared to pure water. The ecographic probe was used for real-time ultrasonic imaging to monitor bubbles formation and oscillation within the channel. From the recorded videos, a novel method was developed to extrapolate quantitative information about stable cavitation activity, finding good correlation with the results obtained through PCD analysis. Finally, a high-speed camera was used for optical imaging to monitor the group behavior of bubbles related to each sample under the excitation of the acoustic field.

In the second part of the study, the focus shifted towards an improvement of the OLNDs performances in order to overcome some limitations due to the US activation source. In particular, acoustic field presents a limited ability to reach deeper zones of the human body due to absorption that US undergoes while travelling across human tissues. A possible solution to this challenge is the alternative use of the magnetic field which is characterized by a more penetrating profile. However, OLNDs first need to be functionalized through magnetic agents (nanoparticles) to become sensitive to the magnetic field for this approach to be effective.
A few studies have been found in the literature that have investigated magnetic OLNDs (MOLNDs), but their focus has mainly been on the use of the droplets as US imaging platforms during hyperthermia treatments performed by the magnetic NPs bound on their surface. This work, on the other hand, aims to obtain a dual-sensitive system capable of releasing oxygen through the use of either ultrasound or magnetic field obtaining comparable results in terms of performance. The mechanism behind the oxygen release mediated by an alternating current (AC) magnetic field is the magnetic droplet vaporization (MDV). Specifically, the nanoparticles interacting with the AC magnetic field are able to produce local heat on the droplet surface, leading to an increase of the temperature up to the boiling point of the PFC-core employed, thus enabling the vaporization and the gas release.
Six different OLNDs, differing in core and coating, were prepared for the study, and Fe_3O_4 NPs were used as magnetic functionalization agents. The optimal NPs concentration was found in order to ensure a good bounding over the droplets surface

and a detailed preparation method was presented. After a physico-chemical characterization of the MOLNDs, providing information about their morphology, shape and ζ potential, also the acoustic response was tested, in order to evaluate the NPs influence on the OLNDs behavior. It was found a shift of the cavitation thresholds, both stable and inertial, towards lower acoustic pressures due to the functionalization. Two different setups were then used to assess that correct occurrence of the functionalization phase, one based on the ecographic imaging while the other on a microfluidic setup, both evaluating the influence of a static magnetic field on the MOLNDs streaming velocity and trajectory. Finally, the oxygen released following US and AC magnetic field was monitored and compared, confirming the effectiveness of the magnetically-mediated approach as valid alternative as therapeutic method. Furthermore, the comparison between the cores and coatings allowed to perform an evaluation of the optimal carrier in terms of functionalization rate and oxygen release control.

Overall, this study provides new insights into the potential of sono-sensitive nanosystems to release oxygen. More information about OLNDs acoustic response is provided, together with a novel method for monitoring the cavitation activity. A standardized method is also proposed to make OLNDs dual-sensitive systems using as activation source also the magnetic field, proving therefore their high potential as promising and versatile oxygen delivery systems.

Contents

List of Figures **xi**

List of Tables **xvii**

Nomenclature **xviii**

1 Introduction **1**

1.1 State of the Art 2

1.1.1 Stimuli-responsive Drug Delivery 7

1.1.2 Ultrasound Drug Delivery 11

1.1.3 Phase-shift Perfluorocarbon Nanodroplets 12

1.1.4 Magnetic Nanodroplets 17

1.2 Motivation and Scope 18

1.3 Chapter Summary 19

2 Theoretical Background **21**

2.1 Acoustic Cavitation 22

2.1.1 Bubble Nucleation 24

2.1.2 Bubble and Acoustic Field 25

2.1.3 Bubble Oscillator 25

2.1.4 The onset of stable and inertial cavitation 29

2.1.5 Growth of a bubble - Rectified diffusion 31
2.1.6 The coalescence process 34
2.1.7 Inertial Cavitation and its applications: sonochemestry and ROS generation 35
2.2 Phase-shift Perfluorocarbon Nanodroplet Vaporization 37
2.2.1 Intermolecular Forces and Equilibrium Phase Behavior . . . 37
2.2.2 Laplace pressure theory 40

3 Methodology 44
3.1 Uncertainty of Measurements 44
3.1.1 Guide to the Expression of Uncertainty in Measurement . . 45
3.1.2 Direct Measurements 47
3.1.3 Indirect Measurements 49
3.2 Multiple Approaches for Ultrasonic Cavitation Monitoring 51
3.2.1 OLNDs Preparation and Characterization 52
3.2.2 Phantom Preparation 54
3.2.3 Experimental Setup 55
3.2.4 Improvement of the Optical Setup 58
3.3 OLNDs Functionalization with Magnetic NPs 59
3.3.1 MOLNDs preparation 60
3.3.2 Physicochemical Characterization 61
3.3.3 Acoustic Characterization 61
3.3.4 Functionalization Assessment 62
3.3.5 Magnetic Droplet Vaporization 64
3.3.6 Oxygen Release 64

4 Results and Discussion 66
4.1 Multiple Approaches for Ultrasonic Cavitation Monitoring 66

4.1.1 First Setup 68
4.1.2 Improvement of the Optical Setup 78
4.2 OLNDs Functionalization with Magnetic NPs 85
4.2.1 Physico-chemical Characterization 85
4.2.2 Acoustic Response of MOLNDs 89
4.2.3 Functionalization Assessment 95
4.2.4 Magnetic Droplet Vaporization and Oxygen Release 99

5 Conclusions and Outlooks **105**

References **111**

Appendix A Fe_3O_4 Nanoparticles **127**

List of Figures

1.1 Possible routes exploited for the administration of drug to a patient [1]. 2

1.2 Pharmacokinetic phases of a drug [2]. 5

1.3 Number of publications per year related to phase-shift PFCs nanodroplets [3]. 13

1.4 Schematic representation of ADV and acoustic cavitation mechanisms of a liquid nanodroplet interacting with a sinusoidal acoustic field. 14

2.1 Scheme of the bubble growth and final collapse under sinusoidal acoustic field. 23

2.2 Scheme of the cycle of gas bubbles in liquids under acoustic field [4] 25

2.3 Bubble parameters of bubble and liquid environment used to describe the oscillator system through the Reyleigh Model 26

2.4 Cavitation prediction chart for a 10 kHz system in a 100% gas saturated system taken from Apfel [5] showing the different cavitation regions bubbles can undergo. 30

2.5 Scheme of the thickness of the boundary layer (shell) of a bubble changing during its expansion and compression cycles, and showing how bubble expansion enhances the concentration gradient. 32

2.6 A) Scheme of coalescing process of two colliding bubbles and B) variables used for two bubbles in contact [6]. 35

2.7 Lennard-Jones 6-12 potential diagram [7]. 39

2.8 Plot of the reduced Van der Waals equation of state (2.36) [8]. A) Plot showing the dependence of the pressure on temperature and volume. B) Plot enhancing the isobaric line for a vapor-liquid transition at a specific temperature in which the regions A and B have the same area (equal probability), meaning equal chemical potential. C) Saturation curve (black line) built starting from the isobaric lines drawn on the pressure-volume curves. D) Reduced pressure-specific volume liquid-gas phase diagram at fixed temperature. 41

2.9 Role of the Laplace pressure in the pressure–temperature phase diagrams for C_3F_8 A) and C_4F_{10} B) [8]. 42

2.10 Theoretical ultrasound PNP trend respect to droplet size predicted through Antoine equation [8]. 43

3.1 Gaussian (Normal) probability density function showing the range of values covered for three different levels of confidence. 49

3.2 Scheme of the final OLND. 52

3.3 A) Size distribution obtained by DLS investigation of chitosan-coated OLNDs and B) Optical microscope image of PVA-coated OLNDs with a magnification of 40 $\times$. 53

3.4 A) DLS size distribution (black line) and B) TEM image of ZnO NPs [9]. 54

3.5 Customized cylindrical phantom with the channel inside. 54

3.6 Scheme of the experimental setup employed for the carriers characterization. 55

3.7 Scheme of the setup implemented in order to improve the high-speed camera recording parameters. 59

3.8 Schematic representation of the magnetic oxygen-loaded nanodroplets (MOLNDs). 61

3.9 Schematic representation of A) the setup used to record the droplet behavior by means of ecographic imaging probe and B) of the microfluidic chip employed to evaluate the steering angle and the velocity variation due to the magnet influence 63

3.10 Typical temperature trend over time measured by the fiber optic probe during the excitation of MOLNDs through an uniform AC magnetic field. 64

3.11 A) Illustration of the setup used to conduct oxygen release experiments on OLNDs samples during US exposure. B) Visual depiction of the experimental system to evaluate oxygen discharge induced by the alternating magnetic field stimulus. 65

4.1 FFT spectra of chitosan-, PVA- coated OLNDs and ZnO NPs compared with respect to pure water (black line) at different acoustic pressures: A) 0.29 MPa, B) 0.36 MPa, C)0.40 MPa, D) 0.53 MPa, E) 0.74 MPa, F) 0.79 MPa. 67

4.2 Comparison of the cavitation noise power (CNP) among pure water, ZnO NPs, chito-coated OLNDs, and PVA-coated OLNDs at varying acoustic pressures. The black dashed line in the graph represents a qualitative threshold for determining the occurrence of the inertial cavitation regime. 70

4.3 Four consecutive frames of the videos recorded by the US ecographic probe at two different acoustic pressures for pure water, ZnO NPs, chitosan- and PVA-coated OLNDs. 71

4.4 Comparison of the intensity averaged on 4.5 s of the light spots measured into the ROI (yellow box in Figure4.3) for each solution at different acoustic pressures. 72

4.5 Comparison of the instantaneous intensity of the light spots measured into the ROI (yellow box in Figure 4.3) for each solution at $P_a = 0.39$ MPa (dashed lines) and $P_a = 0.79$ MPa (continuous lines). 73

4.6 Frames recorded with the high-speed camera with a frame rate of 3000 fps at different time of ZnO NPs at acoustic pressure $P_a = 0.74$ MPa. 75

4.7 Frames recorded with the high-speed camera with a frame rate of 3000 fps at different time of chitosan-coated OLNDs at acoustic pressure $P_a = 0.74$ MPa. 76

4.8 Frames recorded with the high-speed camera with a frame rate of 3000 fps at different time of pva-coated OLNDs at acoustic pressure $P_a = 0.74$ MPa. 77

4.9 High-speed camera frames of A) ZnO NPs with a 20× objective lens, B) PVA-coated OLNDs with a 40× objective lens and C) chitosan-coated OLNDs with a 60× objective lens. 78

4.10 Frames captured by the high-speed camera with a 40 × objective lens at a recording speed of 5000 fps of the samples. Circles in the frames highlight the trajectory traveled by a single bubbles under US field. 79

4.11 Average streaming velocities evaluated for each carrier from the videos recorded by the high-speed camera at different acoustic pressures. 80

4.12 Frames captured by the high-speed camera with a 20 × objective lens at a recording speed of 10000 fps of the samples under an acoustic pressure of 0.47 MPa. For each sample, the life cycle of a single bubble (highlighted by the colored circles) is shown starting from its formation in the first frame and ending with its disappearance in the fourth frame. 81

4.13 Average lifetimes evaluated for each carrier from the videos recorded by the high-speed camera at different acoustic pressures. 82

4.14 Frames captured by the high-speed camera with a 40 × objective lens at a recording speed of 10000 fps of PVA-coated OLNDs under an acoustic pressure of 0.57 MPa. Attention is drawn to a group of adjacent bubbles that undergo the coalescence process, which is highlighted using black dashed circles. 83

4.15 Frames captured by the high-speed camera with a 60 × objective lens at a recording speed of 5000 fps of chitosan-shelled OLNDs under an acoustic pressure of 0.47 MPa. A) Consecutive frames showing the approaching of two close bubbles; B) consecutive frames of the same bubbles after ≈ 164.7 ms undergoing the coalescence process. 84

4.16 SEM images of A) chitosan-coated OLNDs and B) MOLNDs. . . . 86

4.17 TEM images of A) a group of DFP-based, chitosan-coated MOLNDs and B) a single zoomed MOLND. 87

4.18 Hydrodynamic diameter distribution obtained by DLS technique. In each graph OLNDs and correspondent MOLNDs are plotted together in order to appreciated the influence of Fe_3O_4 NPs on the distribution. 88

4.19 FFT spectra of DFP-based OLNDs and MOLNDs at different acoustic pressures. 91

4.20 FFT spectra of PFP-based OLNDs and MOLNDs at different acoustic pressures. 92

4.21 Cavitation noise power analysis for DFP-core OLNDs and MOLNDs at different acoustic pressures. 93

4.22 Cavitation noise power analysis for PFP-core OLNDs and MOLNDs at different acoustic pressures. 94

4.23 Frames depicting the movement of DFP-MOLNDs at three successive times after the application of US. The top sequence shows the droplets without the presence of a permanent magnet, while the bottom sequence regards the droplets with the magnet, indicated by a yellow box. Circles are used to track one droplet movement over time. 96

4.24 Frames depicting the movement of DFP-MOLNDs at three successive times after the application of US. The top sequence shows the droplets without the presence of a permanent magnet, while the bottom sequence regards the droplets with the magnet, indicated by a yellow box. Circles are used to track one droplet movement over time. 97

4.25 Average streaming velocities of DFP- and PFP-MOLNDs in presence and in absence of the magnet. 98

4.26 A) Mean steering angle values and B) mean streaming velocity values obtained for DFP-MOLNDs samples through the microfluidic channel setup. 98

4.27 Variation of the oxygen concentration measured during US irradiation in a solution of DFP- and PFP-OLNDs over time. 100

4.28 Variation of the oxygen concentration measured after AC magnetic field excitation in a solution of DFP- and PFP-MOLNDs at different temperatures. 102

4.29 Oxygen concentration profile measured in the 270 s following the MOLNDs sample heating by means of AC magnetic field up to DFP (red lines) and PFP (black lines) boiling points. The dashed lines represent the second order fit of the measurement data. 103

4.30 Optical images of DFP- and PFP-MOLNDs after been subjected to an AC magnetic field, demonstrating the occurred MDV. 104

A.1 A) Representative TEM picture, B) size distribution (derived from statistics on TEM images), C) and XRD pattern of Fe_3O_4 NPs [10]. 127

A.2 Magnetic properties of Fe_3O_4 nanoparticles are shown [10]. A) $M(H)$ curve of the nanoparticles at room temperature in dry form, with a portion of the hysteresis loop zoomed to highlight the coercivity. B) Dynamic minor hysteresis loops of the nanoparticles for a magnetic field with a peak amplitude $\hat{H}_a$ ranging from 13 kA m^{-1} to 32 kA m^{-1} and a fixed frequency of 69 kHz. C) Specific loss power (SLP) values for Fe_3O_4 NPs at different peak amplitudes of the AC magnetic field, with a fixed frequency of 100 kHz. 128

List of Tables

1.1 Administration routes for drug delivery. 3

1.2 Advantages and disadvantages of conventional and controlled drug delivery systems. 6

1.3 Comparison between exogenous stimuli for drug delivery systems . 10

1.4 Advantages and disadvantages of materials used as shell. 15

1.5 Perfluorocarbons used for nanodroplets core with relative boiling temperature. 16

3.1 Coverage factors and relative percentages of coverage relative to the normal distribution. 49

3.2 Residual magnetization (B) of the NdFeB magnet as function of the distance. 63

4.1 Mean hydrodynamic diameter and ζ potential for OLNDs and MOLNDs samples measured by means of DLS. 89

4.2 Acoustic pressures for entering the inertial cavitation regime. 90

4.3 % uncertainties of the measurements of the oxygen concentration in OLNDs solution evaluated at 30 s intervals for a total of 270 s. . . . 101

4.4 % uncertainties of the measurements of the oxygen concentration in MOLNDs solution evaluated at each temperature considered. 103

Nomenclature

Acronyms / Abbreviations

AC	Alternating Current
ADV	Acoustic Droplet Vaporization
API	Active Pharmaceutical Ingredient
CNP	Cavitation Noise Power
DFP	Decafluoropentane
DLS	Dynamic Light Scattering
EAPs	Electro-Active Polymers
EDL	Electric Double Layer
FFT	Fast Fourier Transform
GG	Gellan Gum
GUM	Guide to the Expression of Uncertainty in Measurement
IVIVC	In-Vivo In-Vitro Correlation
JCGM	Joint Committee for Guides in Metrology
LED	Light Emitting Diode
LPU	Law of Propagation of Uncertainty
MDV	Magnetic Droplet Vaporization

MOLNDs Magnetic Oxygen-Loaded Nanodroplets

NIR Near-InfraRed

NPs Nanoparticles

ODV Optical Droplet Vaporization

OLNBs Oxygen-Loaded Nanobubbles

OLNDs Oxygen-Loaded Nanodroplets

PCD Passive Cavitation Detector

PFC Perfluorocarbon

PFP Perfluoropentane

PRP Peak Rarefractional Pressure

PVA Polyvinyl Alcohol

ROI Region Of Interest

ROS Reactive Oxygen Species

SDT Sonodynamic Therapy

SEM Scanning Electron Microscopy

SLP Specific Loss Power

SPIONs Superparamagnetic Nanoparticles

TI Therapeutic Index

UCA Ultrasonic Contrast Agent

US Ultrasound

UV Ultraviolet

XRD X-ray diffraction

ZnO Zinc Oxide

Chapter 1

Introduction

In last decades, the interest in the development of novel drug administration techniques have shown a significant increase from the scientific world due to the limits presented by conventional methods used in standard medicine. The necessity to overcome these limits, together with the impressive improvements obtained in the nanotechnology field, has led to the development of new miniaturized drug delivery carriers (nanocarriers) able to perform treatments to specific diseases directly towards unhealthy cells and tissues, providing for the first time the so-called drug targeting [11, 12]. A crucial rise in the therapeutic activity of the drugs and, at the same time, a reduction of the problems related to their toxicity soon have shown the great potential of this innovative technology, enabling the advancement of the nanocarriers engineering so as to spread their efficacy to a variety of pathologies [13, 14].
In this first chapter, it is presented the state of the art achieved in the drug delivery branch, briefly describing the variety of approaches developed in the field. The focus then moves towards the ultrasound (US) stimuli responsive drug delivery technique, that represents the center of this work. A general overview on US field in medicine is first presented, followed by a qualitative introduction to the acoustic cavitation, i.e. the mechanism induced by US that actually enables the drug release. Perfluorocarbon (PFC)-based oxygen loaded-nanodroplets (OLNDs) are then introduced as innovative and efficient oxygen carriers for treatment of hypoxic diseases, giving an overview of their actual application and studies in the research field, including the recent development of magnetic oxygen-loaded nanodroplets (MOLNDs). These last carriers, thanks to the presence of magnetic nanoparticles on their structure are able to couple both acoustic and magnetic stimuli for their medical purpose.

To conclude, the chapter explains the motivation and scope of this work, based on the fact that most of the studies present in literature are more focused on the direct droplets treatment application without going deeper in the phenomena characterization.

1.1 State of the Art

A drug delivery system is a platform able to release active pharmaceutical molecules in order to achieve a specific desired therapy [2]. The conventional delivery techniques implies the use of a variety of different systems, such as pills, tablets, capsules, syrups, ointments, creams, gels and others, each characterized by a specific administration method. Figure 1.1 shows all the possible routes used in conventional drug delivery administration and Table 1.1 describes the respective administration method for each rout. The factors that influence the choice of the optimal method for administering a drug depend on the characteristics of the drug itself, such as its physical and chemical properties, as well as the specific disease being treated. These factors may include the site in the body where the drug is to be administered, the absorption rate of the drug, and the condition of the patient [1, 15].

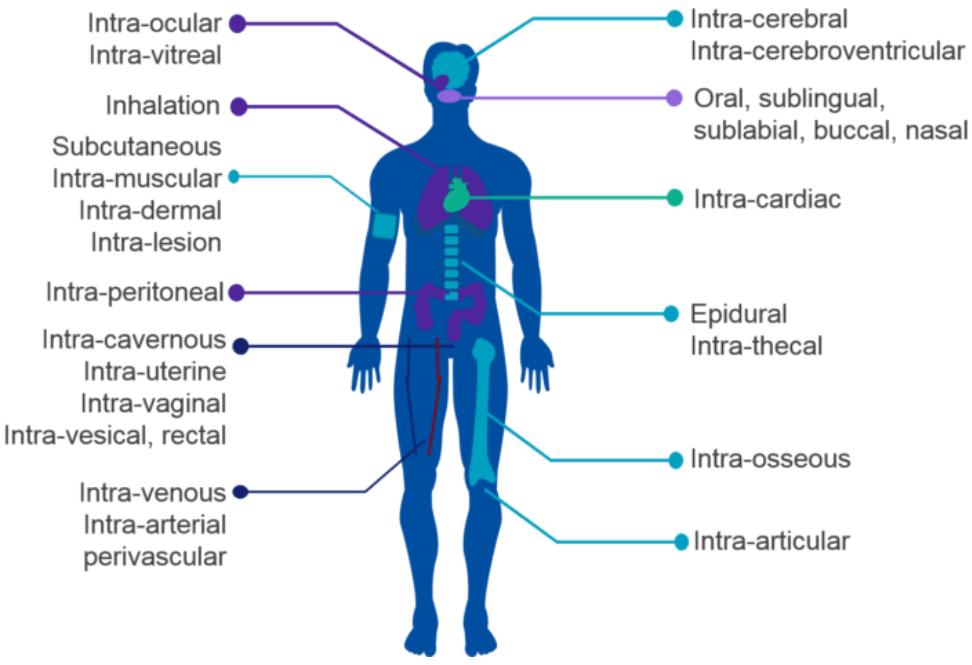

Fig. 1.1 Possible routes exploited for the administration of drug to a patient [1].

Table 1.1 Administration routes for drug delivery.

Administration route	Description
Oral	Shallowed by mouth
Buccal	Held inside the cheek
Sub-lingual	Put below the tongue
Enteral	Directly delivered into the intestine or stomach
Nasal	Breathed in
Ophthalmic	Dropped into eyes
Otic	Dropped into the ear
Rectal	Inserted into the rectal
Vaginal	Inserted into the vagina
Topical	Applied to the skin
Transdermal	Given through a patch placed on the skin
Infused	Injected into a vein and slowly dripped in over time
Intramuscular	Injected into the muscle
Intravenous	Injected into a vein
Subcutaneous	Injected under the skin

Among the others, oral administration, in which a drug is swallowed and dissolved in the stomach in order to be through the intestines, is the most common and oldest form of administering therapeutic and medical products. However, for drugs that cannot survive the stomach environment causing undesirable side effects, parenteral routes may be used to bypass the gastrointestinal tract. These routes include intravenous, subcutaneous, and intramuscular injections, which have a faster absorption rate compared to oral administration. In cases where tissues have strong barriers or poor vascularization, direct injection methods may be necessary for drug administration. However, traditional drug delivery systems often have limited bioavailability, fluctuating drug levels in circulation, and difficulties in achieving sustained drug release.

The ultimate aim of drug delivery techniques results, thus, to have a direct control in the increase of the drug concentration in a specific part of the body compared to others [16].

A drug formulation is the result of a specific dosage form obtained by mixing the active pharmaceutical ingredient (API) with the non-drug component, i.e. excipients/additives, in order to increase drug stability, enhance bioavailabilty, improve safety, allow for convenient dosage, mask the taste, etc. [17, 18]. An important aspect to consider when dealing with drug delivery systems is their pharmacokinetics,

i.e. the study of how the organism affects the drug. As schematized in Figure 1.2, a drug undergoes four phases during its administration:

1. the drug movement from its administration site towards the systemic circulation is called *absorption* and depends on different factors (route of administration, drug physicochemical properties) [19]. The percentage of adsorbed drug is called bioavailabilty and is strictly dependent on the administration method, for example in oral administration it results quite limited due to both incomplete absorption and drug metabolism in the liver, while intravenous injection is characterized by 100% of bioavailability. Furthermore, absorption can occur either by passive or active transport. In the first case, the drug movement is due to the concentration gradient present at cell membranes, inducing drug molecules to pass across it from higher concentration region to the lower one. In this case, absorption is influenced by drug solubility, molecular size, degree of ionization and the absorptive surface area available. Active transport, on the other hand, allows the transport against a concentration gradient exploiting an external energy source;

2. the transfer from the bloodstream and the extra-vascular fluids and tissues (muscles, brain, fat) is the drug *distribution* and is crucial for establishing the amount of drug able to reach target regions respect to the rest of the organism. Therefore, this phase is important for the definition of the drug efficacy and toxicity and depends on some factors, such as the blood flow, molecular sized, binding affinity with the plasma proteins and lipophilicity [20, 21];

3. in the liver and in the gut wall, drugs undergo the *metabolism* due to the activity of enzymes. During this step, the drug amount can be reduced up to $70-80\%$ before being absorbed into the systemic circulation [22];

4. the last phase regards the removal of metabolites and unchanged drugs, the so-called *excretion* that can occur through different routes, including bile, sweat, urine, tears.

The drug release profile, which refers to the variation in drug concentration in the plasma over time, is a critical element in the effectiveness of a drug delivery system [23]. This profile helps to determine the range of concentrations that should be maintained between the minimum effective level and the toxic level in order for the

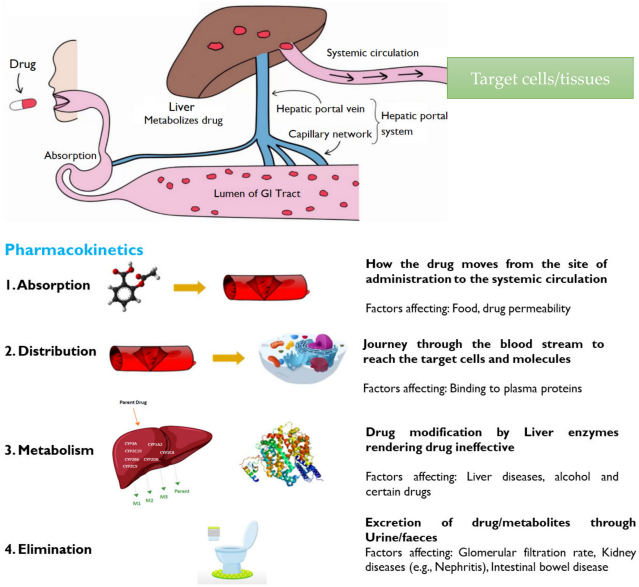

Fig. 1.2 Pharmacokinetic phases of a drug [2].

drug to be both effective and safe in its therapeutic action [24]. The therapeutic index (TI), which compares the amount of the therapeutic agent that is actually effective to the amount that causes toxicity, can be used to evaluate the relative safety of a drug [25, 26]. TI is calculated as the ratio between the toxic dose of the drug and the dose that produces a therapeutic effect.

One of the main challenges with conventional drug delivery systems is their inability to maintain drug doses within this therapeutic range. The drug level in the systemic circulation after a conventional single dose typically experiences a steep initial rise due to fast metabolism, followed by an exponential decrease. To address this issue, controlled release drug delivery systems have been developed that are able to maintain drug levels within the therapeutic window for longer periods of time. Table 1.2 compares the advantages and disadvantages of conventional and controlled drug delivery systems. The design of a controlled release drug delivery systems is crucial for achieving the improvements listed in Table 1.2, and a range of factors must be considered in this process. These factors can be divided into two categories: formulation-related and drug-related parameters. The first category includes characteristics of the biomaterials used in the system's formulation, such as biocompatibility, hydrophilicity, surface chemistry, degradation rate, and rheological properties. It also includes the route of administration, pharmacokinetics, and methods to improve stability, such as controlling dimensions, adding growth factors, and

Table 1.2 Advantages and disadvantages of conventional and controlled drug delivery systems.

	Advantages	Disadvantages
Conventional Drug Delivery	Convenience in administration Non-invasive and good IVIVC Accurate unit dosage form Higher self-life Accommodate patient variation Flexibility in dose adjustment Low cost	Poor absorption No target specificity Premature excretion Fast drug metabolism Poor bioavailabilty Repeated dosing Poor patient compliance
Controlled Drug Delivery	Controlled release Target specificity Long drug residence Metabolism protection Improved bioavailability Low dosing frequency Better patient compliance	Low toxicity Dose dumping Invasive administration Reduced efficacy Poor IVIVC Limited standards higher cost

manipulating the colloidal state [27]. The second category concerns the properties of the drug itself, such as the binding efficiency with plasma proteins, the ability to cross biological barriers and regulatory factors are the major factors [28].
Classification of controlled drug delivery systems is based on the release mechanism exploited [29]:

- **dissolution-controlled systems** - drug is coated with a dissolving polymeric membrane or matrix [30];
- **diffusion-controlled systems** - drug is trapped in a inert water-insoluble polymeric membrane or matrix and the release occurs via diffusion from higher to lower concentration sites [31, 32];
- **osmotic-controlled** - osmotic pressure is exploited using either drug which itself acts as osmogen or adding an osmogenic salt to the formulation. The water penetration into the system, controlled by the osmotic pressure generated between a rigid semipermeable and biocompatible membrane, controls the drug rate releases [33];

- **swelling-controlled** - drug is dissolved in a hydrophilic polymeric matrix in a glassy state. When the system is put in an aqueous solution, water enters the matrix lowering the glass transition point below the ambient temperature. In this way, polymer becomes swollen and rubbery, allowing drug diffusion out of the matrix [34];
- **chemically-controlled** - employing biodegradable polymers for building the structure of the drug delivery system, it is possible to initiate the release by means of spontaneous degradation of the polymers due to the exposition to the biological environment [35]. Drug can be either dissolved within the polymer or chemically conjugated to it and, in both cases, the need of excretion of the delivery system is overcome by the biodegradability of the polymers;
- **stimuli-responsive** - some biomaterials, if subjected to a physical or chemical external stimulus, undergo physico-chemical changes can be exploited for the induction of the drug release in the desired site [36, 37].

A strategic role in the design of drug delivery systems is therefore played by the choice of the biomaterial. Biomaterials are substances properly engineered, with the purpose to interact with the biological environment for therapeutic or diagnostic aims. They allow to modulate the drug pharmacokinetics, defining the physico-chemical properties and the release profile of the drug delivery systems. Polymers, proteins, polysaccharides, peptides and lipids are the usual biomaterials involved in the formulation of nanocarriers that can be characterized by diverse sizes, properties and architectures [38]. The choice of the optimal biomaterial is based on the type of drug, site and route. Furthermore, it needs to be biocompatible, non-toxic, with good mechanical strength, preferably biodegradable and hydrophilic [27].

1.1.1 Stimuli-responsive Drug Delivery

Stimuli-responsive drug delivery systems have garnered significant interest in the scientific community due to their high versatility and potential for treating a variety of difficult diseases. The ability to utilize different materials and stimuli has resulted in an exponential increase in research efforts focused on this technology, leading to important advancements in the development of a wide range of drug delivery platforms.

In the treatment of stimuli-responsive systems, a key consideration is the type of stimulus used to activate the carrier and release the drug. These stimuli can be classified as endogenous or exogenous, depending on whether they are induced by the target organic environment or an external source [38, 39].
The first category relies on the induction of a chemical reaction through the interaction between the biomaterial used for the carrier formulation and the organic environment to which the system target. For instance, pH variations can be exploited in specific organs to trigger the drug release, either using a polymer with ionizable groups that undergo solubility changes in an environment characterized by a pH gradient or designing a polymer-based system with acid-sensitive bonds whose cleavage allows the release of the bounded molecules [40–44]. Another approach is based on the exploitation of the ability of enzymes to recognize and catalyze physicochemical material changes. It is possible, thus, to perform the enzyme-mediated drug release through drug accumulation at a specific target. This mechanism is enhanced by the fact that some diseased conditions present an overexpression of specific enzymes making this systems particularly useful and effective thanks to their high specificity [45–48]. Carriers sensitive to redox chemical reactions, instead, offer a promising approach for drug delivery, as they can release the drug by degrading the polymer structure only in a reducing environment. This type of environment is typically found in tumor cells, allowing for targeted drug delivery to cancerous cells while minimizing the impact on healthy cells [49–51].
On the contrary, exogenous stimuli-responsive drug delivery systems utilize an external energy source to induce a physicochemical reaction on the carrier's polymeric structure, resulting in the release of the drug. These systems can be activated by a variety of external stimuli, including temperature changes, light, magnetic and electric fields, and ultrasound, each of which exploits a specific physical property of biomaterials. This allows for the controlled release of therapeutic agents through the application of external stimuli.
One of the most investigated stimuli-responsive strategy has been the thermoresponsive drug delivery. This is based on the non-linear sharp change in the properties of carrier biomaterial induced by a local temperature variation [52, 53]. Ideally, nanocarriers need to be characterized by a trigger temperature higher then human body value ($\sim 37\ ^{\circ}\mathrm{C}$) in order to control the release through an external thermal source. Generally, thermoresponsive materials show a low critical solution temperature and heat can be applied using temperature-controlled water sacks, radiofrequency oscillators

or microwaves applicators. Thermoresponsive drug delivery can be also obtained inducing a temperature decrease (cryotherapy). In this case, the encapsulated drug is led to spontaneously diffuse out as a consequence of the increase of the carrier porosity due to a reversible de-swelling process.
External light can be used non-invasively in case of photosensitive biomaterials allowing a delivery with high spatial and temporal precision [54–56]. Using this kind of biomaterials, the systemic drug dose can be reduced, minimizing the undesired side effects and extending the action over time only in the desired site [57]. The most common light source exploited is the ultraviolet irradiation (UV) since light-responsive biomaterials are mostly sensible to short wavelength light [58, 59], but, in order to overcome limits due to UV poor tissue penetration and damaging effects on healthy organs, recently, near-infrared (NIR) or visible-light responsive materials have been investigated [60–62].
Also magnetic stimulation has been exploited for activation of drug delivery carriers. It shows great advantages in targeting the desired sites, controlling the release rate and monitoring the concentration and distribution of the system. Usually, Fe_3O_4 superparamagnetic nanoparticles (SPIONs) with dimensions around 100 nm or less are involved in this kind of application, offering a convenient combination between magnetic responsiveness and biocompatibility [63, 64]. SPIONs are usually encapsulated in colloidal carriers or polymeric shells and, when interacting with a high-frequency alternating magnetic field, induce hyperthermia for releasing drug [65].
Systems composed of electro-active polymers (EAPs) can undergo a change in shape or volume as a consequence of electric current stimulation [66]. Specifically, under an electrical potential, EAPs can be reversibly oxidized/reduced altering polymer charge and conformation allowing either a direct repelling of the drug payload or an increase of its diffusion outside the carrier [67]. Moreover, thanks to reversibility of redox reactions, many electro-responsive carriers can be stimulated repeatedly resulting in a on-off switch [68].
Another promising source, already used in medicine for different diagnostic techniques, is US, showing great advantages respect to the others, especially regarding its cost and safety profile maintained during the interaction with health tissues. Being a central matter of this work, the description of this last US-based stimuli-responsive drug delivery method is going to be treated in detail in the following section.
Table 1.3 summarizes the main advantages and drawbacks related to each of the pre-

viously described exogenous stimuli drug delivery systems. Recent advancements in

Table 1.3 Comparison between exogenous stimuli for drug delivery systems

Stimulus	**Advantages**	**Drawbacks**
Thermal field	Design versatility Easy tunability Passive targeting	Safe and sensitive materials Poor mechanical strength Low compatibility
Light	High precision Easy tunability Low cost	Limited penetration Invasive for deep zones Challenging targeting
Magnetic field	Efficient targeting Intensity modulation High tissue penetration	Possible cytotoxicity High cost
Electric field	Significant design freedom High release control	Low tissue penetration Possible tissue damage High cost
Acoustic field	Good penetration Easy tunability Low cost	Challenging targeting Challenging homogeneous exposure

stimuli-responsive systems have resulted in the development of multi-stimuli responsive systems, which are capable of responding to multiple stimuli [69–71]. These systems can offer a range of benefits, including the ability to integrate the advantages of each strategy into a single platform, with the capacity to overcome the limitations of single-stimulus carrier through improved modularity and spatiotemporal control. In particular, one of the main problems of single-stimulus drug delivery systems comes from the various physiological and pathological barriers they meet especially when dealing with anticancer treatments. The use of co-triggered carriers allows to use a specific stimulus for different levels of the organism therefore overcoming sequential barriers. Furthermore, they exhibit more degree of freedom in their design, giving the possibility to merge together therapeutic and imaging purposes in a single system.

1.1.2 Ultrasound Drug Delivery

US application in medicine field is widely diffused since decades due to its immediate significance from a practical point of view. From a clinical aspect, indeed, US possesses great versatility in all the branches of medicine, from obstetrics to cardiology, orthopedics and so on, particularly thanks to its non-invasive characteristics and relatively easy management [72]. Historically, US find its first medical application in the 50 s for the development of a brain imaging technique, leading to the understanding of its great potential so that nowadays it results the second most used imaging methods worldwide [73].
Among the others, the use of ultrasonic contrast agents (UCAs) for enhancing the acoustic signal in US imaging techniques has demonstrated impressive advancement in image contrast and spatial resolution [74]. In this kind of technique, images are generated from the measurement of the propagation of high frequency acoustic waves interacting with materials and tissues characterized by different acoustic properties [75, 76]. UCAs exploit their high echogenicity for amplifying the acoustic signal emitted by tissues, allowing imaging also of organs with poor US contrast [77]. The agents consist typically of gas-filled microcarriers with dimensions ranging in $1 - 10$ μm that, interacting with US field, undergo acoustic cavitation phenomena that enhance the reflected US signal. The physical principles behind acoustic cavitation are exposed in detail in Section 2.1. The high sensitivity, portability, low cost and the good safety profile demonstrated by these formulations through the various studies have led researchers to spread their application beyond the imaging techniques. Indeed, in addition to their diagnostic capability and thanks to their structure, carriers can be loaded with molecules, drug or gene as well as functionalized with ligands, thereby giving the possibility to reach specific targets of the human body, hence allowing the expansion of these methods also to promising therapeutic strategies, such as gene and drug delivery [78]. The specific contents encapsulated within the carrier depend on the type of sonosensitive carrier utilized. For instance, solid nanoparticles (NPs) can store and release drug molecules or reactive oxygen species (ROS), whereas microbubbles or nanodroplets can transport pharmaceutical or gas molecules.
In general, US interacting with a biological system generates effects that can be categorized as thermal and non-thermal effects. Both thermal and non-thermal effects can have important biological consequences and are being studied extensively in

the field of medical ultrasound. Thermal effects refer to the changes in temperature that occur due to the absorption of US energy [79]. This is useful in targeted drug delivery to heat the drugs, drug carriers and/ or exposed tissues, increasing the release itself, the drug diffusion, permeation and cell uptake [80]. Non-thermal effects refer to the biological effects that are not due to a change in temperature, but rather to the mechanical effects of US waves on tissues and cells. These effects can include cavitation (the formation and collapse of gas bubbles in a liquid), microstreaming (the movement of small volumes of liquid due to the pressure gradients created by US waves), and mechanical stress on cells and tissues. Stable cavitation enables controlled drug delivery, releasing bubbles contents only at the desired site. Inertial cavitation, on the other hand, allows the use of sonosensitizers, such as solid NPs, in sonodynamic therapy (SDT) for cancer treatment, generating ROS [81]. ROS generation results from two primary mechanisms: sonoluminescence and temperature increase, both of which occur during bubble collapse [82]. Inertial cavitation generates light, activating sensitizers similarly to photodynamic therapy (PDT) [83], whereas the high temperature generated can break down the sensitizers, creating free radicals that react with endogenous substrates to produce ROS [84]. Excessive ROS levels in cells can damage proteins, nucleic acids, lipids, membranes, and organelles, potentially activating cell death processes such as apoptosis and necrosis [85].
More in general, US drug delivery, thanks to its advantages, has resolved the major constraints of conventional methods, mostly related on the accumulation in cells, nanoparticles uptake and undesired non targeting delivery [86] and, to date, has been employed to treat cancer, thrombosis, neurogenerative diseases, diabetes [87–89].

1.1.3 Phase-shift Perfluorocarbon Nanodroplets

Recently, research has shown an increased interest in the development of new oxygen carriers for treating hypoxic tissues as a consequence of a variety of diseases, such as cancer, diabetes and infections, due to the fact that the current hyperoxygenation techniques have several drawbacks [90–93]. New perfluorocarbon (PFC)-based microbubbles formulations have been proposed as they provide promising properties. These molecules possess the ability to stabilize gases, exhibit high stability, and are biologically inert [94–97].
Another advantage derives from the interaction between bubbles and acoustic field, which leads to a local modulation of permeability of both the cell membranes and mi-

crovasculature. This interaction enhances the release of oxygen and drugs in specific areas. Building upon this, researchers have developed oxygen-loaded nanobubbles (OLNBs) that have a core of perfluoropentane (PFP) and a chitosan shell. These OLNBs have demonstrated efficient, stable, and biocompatible oxygen delivery [90]. Moreover, this has paved the way for the creation of oxygen-loaded nanodroplets (OLNDs), which have a core structure of liquid decafluoropentane (DFP) at body temperature [91, 98, 99]. OLNDs have shown superior gas release efficiency compared to microbubbles while maintaining other favorable properties [100, 91, 96]. Notably, with diameters on the scale of a few hundred nanometers [101], OLNDs can traverse the vascular system and passively accumulate in targeted regions. Figure 1.3 shows the interest in the study of these nanostructures, underlining the growth in the number of publications related to OLNDs starting from 2005.

There are many principles behind the activation of nanodroplets and the consecutive

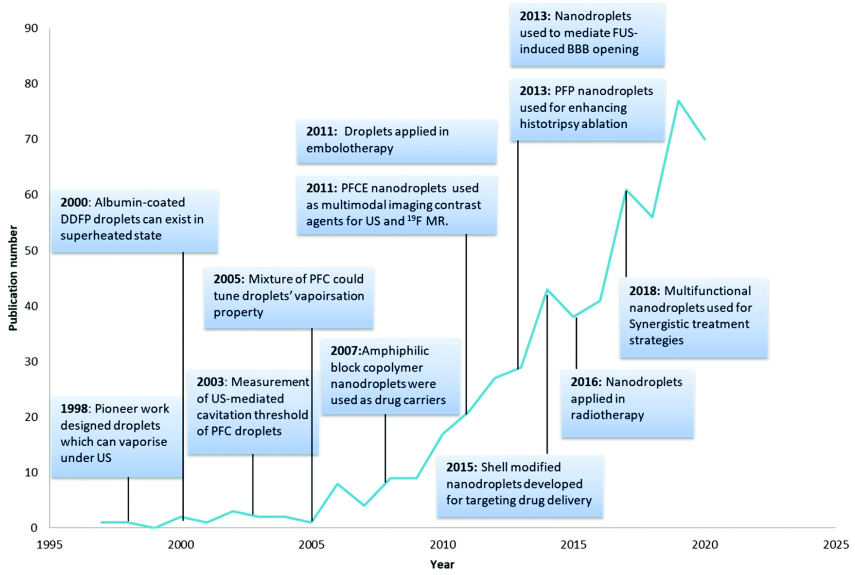

Fig. 1.3 Number of publications per year related to phase-shift PFCs nanodroplets [3].

release of gas; these are due to the interaction between acoustic field and the liquid solution. Firstly, US induces bubble formation after acoustic droplet vaporization (ADV), a phase shift of the droplets into their vapor form (bubbles) [102]. An important advantage deriving from the use of nanodroplets respect bubbles is given by the fact that, changing their physical and chemical properties, it is possible to set both the boiling temperature at which PFCs are able to vaporize into bubbles and also the diffusion velocity of the inner gas in the following gas delivery. Moreover, compared

with the microbubbles, OLNDs are able to maintain their nanometer dimensions in the bloodstream, demonstrating longer circulation time until activation is induced by US excitation [103].
After bubbles are generated, the sinusoidal acoustic pressure variation that the US field generates leads to their consecutive oscillation until the cavitation phenomenon [104]. Oscillation goes on for a few acoustic cycles leading the bubbles to reach resonance size: when it happens, they may undergo either a stable linear oscillation near the resonant size (stable cavitation) or a violent collapse (transient or inertial cavitation). During stable cavitation, oscillation is characterized by microstreaming and Bjerkness secondary forces: the first produces a vortex with shear forces that can be strong enough to break particles or to permeabilize cells; the second forces, due to their attractive and repulsive nature, can attract particles close to the bubbles and release their content. In bubble collapse, instead, a formation of shock waves with high pressure is induced and, owing to translational motion of the bubbles, a jet stream of liquid that can pass through the bubbles and hit the objects in the surrounding zones may occur. This event have been shown to result in a range of uncontrolled side effects that can be harmful to the biological environment. It is therefore important to avoid inertial cavitation in order to minimize these potential risks. To this aim, the working acoustic range needs to be defined in order to limit the inertial cavitation activity. Figure 1.4 schematizes the interaction between a liquid nanodroplet and the acoustic field, starting from ADV, up to cavitation.

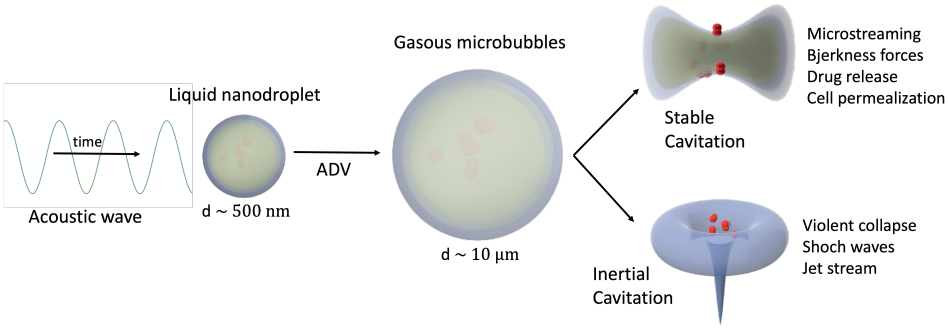

Fig. 1.4 Schematic representation of ADV and acoustic cavitation mechanisms of a liquid nanodroplet interacting with a sinusoidal acoustic field.

Chemical composition of nanodroplets is made of three main parts, the PFC core as already mentioned, the loaded drug or gas and an encapsulation shell, each influencing both the final acoustic response and also the stability of the system. The shell has to be designed to maintain the spherical shape of the droplet with a constant

diameter after injection, as well as to expand during ADV. The state of the shell strongly influences the actual surface tension of nanodroplets, while the choice of the PFC core defines the boiling point at which vaporization can be initiated. ADV process is thus promoted until sufficient acoustic energy is induced to overcome the Laplace pressure provided by the shell and, until that condition nanodroplets stay stable in liquid phase [105]. Therefore, the shell selection needs to take in consideration both the mechanical resistance for providing enough Laplace pressure and the compliance for enabling large deformation during ADV [106]. At the moment, the most popular employed materials for nanodroplets shell result polymers and lipids, although surfactants and albumin are often used. Table 1.4 describes advantages and disadvantages of each material [107, 108].

Table 1.4 Advantages and disadvantages of materials used as shell.

Material	**Advantages**	**Disadvantages**
Albumin	Easy preparation method	High rigidity
Surfactants	Appropriate droplets stabilization	Low affinity for PFCs, high energy required for ADV
Lipids	Versatile formulations	Lateral phase separation due to hydrophobic lipids mismatch
Polymers	Easy and efficient drug loading, adsorption rate enhanced by high surface to volume ratio, possibility of acting as effective targeting tool	High bubbles instability, leaking of PFC before reaching target site due to outer shell defects, high cavitation acoustic pressure

The selection of perfluorocarbons as nanodroplets liquid core comes from the necessity to satisfy important requirements. First of all the core has to be preferably hydrophobic, bioinert and with an appropriate boiling point in order to circulate safely before US are applied and all these criteria can be met by PFC employment [109]. PFCs are chemical compounds characterized by carbon-fluorine bonds and differ each other in the length of the chain that determines the specific boiling temperature. PFCs used for nanodroplets synthesis are listed in Table 1.5 with the respective boiling point. Furthermore, the PFC concentration is also fundamental for tuning the final nanodroplets sizes [110].

Final nanodroplets properties, in particular sizes and size uniformity, are also determined by the synthesis technique. In turn, droplet dimensions and uniformity influences their acoustic behavior and response, as well as the already mentioned

Table 1.5 Perfluorocarbons used for nanodroplets core with relative boiling temperature.

Compound name	**Molecular formula**	**Boiling point (°C)**
Octafluoropropane (OFP)	C_3F_8	-39
Perfluorobutane (PFB)/decafluorobutane (DFB)	C_4F10	-36.7
$2H,3H$-Decafluoropentane (DPF)	$C_5H_2F_{10}$	51-55
Perfluoropentane (PFP)/dodecafluoropentane (DDFP)	C_5F12	29
Pefluorohexane (PFH)	C_6F_{14}	58
Perfluoromethylcyclohexane (PFM)	C_7F_{14}	76
Perflorooctane (PFO)	C_8F_{18}	105.9
Perfluorodichlorooctane (PFD)	$C_8Cl_2F_{16}$	176
Perfluoro-15-crown-5-ether	$C_{10}F_{20}O_5$	146

kinetics [107, 111, 112]. To this aim, a variety of techniques there exist, including sonication, extrusion, agitation, microfluidic synthesis and bubbles condensation.
The first method developed for the production of submicrometer PFC droplets is based on commercial homogenization/agitation systems to reduce particle dimensions. Usually, droplets first are generated by mixing the shell components with an aqueous solution and then adding perfluorocarbon and homogenising into emulsions. Since all components stay within a single container, these techniques avoid material losses. However, these methods often produce droplets with a wide size distribution and low reproducibility [113].
Sonication is the most common due to its low cost and simple process. It is based on the acoustic emulsification of shell component and perfluorocarbon in a aqueous solution [91, 114]. Another advantage of this technique, respect for instance to flow based ones, is given by the fact that the system is closed during synthesis and thus the loss of components of the emulsion is quite limited. Moreover, it is also easy to incorporate other agents into droplets. On the other side, the high energy input can lead to destruction of the emulsion components from the probe [115], the probe erosion can contaminate the solution and the size distribution results quite large.
Extrusion is a more complex method for PFC droplet synthesis and often requires the development of a specific method for each formulation [116, 117]. In addition, droplets aggregation is facilitated and the addition of other compounds is quite challenging. However, this method is gentler respect sonication and allows to obtain

formulations with higher monodispersivity.
Microbubble condensation relies on the use of precursors microbubbles at the gaseous state that are then condensed reducing the temperature and rising the pressure until the core passes to the liquid phase [111]. The advantages provided by this method include the easy generation of high concentration emulsions with minimal equipment requirements and the possibility to manipulate bubbles before condensation [118]. However distributions are highly polydisperse, presenting a considerable amount of quite large droplets.
An approach demonstrating significant results in the droplet size control is based on the exploitation of a microfluidic equipment, able to directly produce monodispersive nanoscaled PFC carriers through a tip-streaming regime [119–121]. The main problems related to this approach are due to the high specialized equipment required and the low production yield, meaning that to be effective for in vivo applications, the process takes many hours.

1.1.4 Magnetic Nanodroplets

Conventional methods for causing droplet vaporization, such as ADV and optical droplet vaporization (ODV), rely on the use of US or optical sources [102, 122]. These methods are limited in their ability to reach deeper target regions in the human body, as the penetrability of these energy sources is dependent on the properties of the tissue they must pass through. To address this limitation, researchers have proposed the use of an alternating magnetic field, which has been shown to have better penetration depth, in combination with magnetically functionalized OLNDs [123]. This approach, known as magnetic droplet vaporization (MDV) [124, 125], utilizes the heat generated by the interaction between the magnetic field and the functionalized OLNDs to vaporize the droplets, potentially allowing for more effective treatment of deeper tissue regions.
Furthermore, functionalization of droplets produced using MDV with magnetic particles enables exploitation of the magnetic field for targeting desired regions, while simultaneously allowing for monitoring using US imaging capabilities [126–129]. This combination of magnetic targeting and US imaging capabilities makes MDV a powerful tool for a wide range of applications, including drug delivery, microfluidics, and particle synthesis.

1.2 Motivation and Scope

The work is divided into two main sections. The first section focuses on the study of OLNDs systems, while the second part presents the experimental results and their analysis on the OLNDs functionalization with magnetic iron-oxide nanoparticles.
While there have been several studies that examine the use of acoustic nanodroplets techniques, most of these studies have focused on in-vitro or in-vivo applications without a thorough characterization of the underlying physical processes. In order to better understand the behavior of these nanodroplets and their potential applications, this first section of the study aims to optimize a setup for inducing cavitation in specific types of droplets and to fully characterize the different signals (acoustic, ecographic, and optical) generated by the interaction with ultrasound. By thoroughly characterizing the basic phenomena involved, this study aims to provide a foundation for future in vitro and in vivo studies of acoustic nanodroplets. The results of the OLNDs are also compared to the acoustic response of zinc oxide (ZnO) porous nanoparticles. Indeed, these nanoparticles have the ability to act as cavitation nuclei under an acoustic field, which means they can facilitate the formation of gas bubbles in a solution [9]. In particular, ZnO has been widely studied for biomedical application due to its biocompatibility, bioimaging high performance properties and its ability to generate reactive oxygen species in SDT [130–132].
The second section is focused on the preparation and characterization of PFCs-based MOLNDs. Research in the field has mainly focused on the application of MOLNDs for magnetic hyperthermia treatment or in vitro biocompatibility studies, cell internalization, and magnetic hyperthermia efficacy, thus directly focusing on their application and without taking into account the oxygen delivery as therapeutic aim. In this study, a standardization of the preparation method is developed, using different PFC cores and three polymeric coatings. Furthermore, both the functionalization of the droplets and the occurracy of the magnetically induced vaporization are investigated and demonstrated, with a final comparison of the oxygen release obtained through acoustic and magnetic field.
In summary, by conducting a series of experiments to characterize the behavior of these droplets under different conditions, this study sought to fill this gap in the literature and provide insights into the potential of these systems for drug delivery and other applications.

1.3 Chapter Summary

- **Chapter 2**: the theoretical background is presented in order to give the mathematical basis for the understanding of the physical behavior of carriers interacting with an ultrasound field. Furthermore a brief description of the mechanism leading to the perfluorocarbon-based droplet vaporization is presented.

- **Chapter 3**: this chapter describes the methods and equipments implemented for each measurement together with the outline of the experiment procedure. It is divided in three main sections, the first related to the evaluation of the uncertainty in the measurements carried on this work, and the others to the experimental setups exploited during measurements. Specifically, in the second part the customized setup built for the characterization of the acoustic response of OLNDs and ZnO nanoparticles is described. The last section is focused on the development of a procedure for the MOLNDs preparation with the characterization methods exploited for understanding the physicochemical properties of the samples. Furthermore, the techniques employed for validating the appropriate functionalization of the samples and the induction of MDV through an alternating magnetic field are presented, concluding with the setups implemented to obtain a comparison of oxygen released through US and AC magnetic field stimuli.

- **Chapter 4**: results obtained for each section are detailed. First, a metrological characterization of the signals emitted during OLNDs and ZnO NPs interaction with the acoustic field is presented. In particular, the acoustic pressure ranges to work in the stable cavitation regime are defined for each sample, a correlation between acoustic signal and ecographic imaging is found and, as final investigation, the group dynamics behavior is studied. Furthermore, some statistics are extrapolated from the videos recorded with the improved optical setup.
  In the second part, the evaluation of the physicochemical properties of MOLNDs, due to the presence of Fe_3O_4 NPs on their surfaces, are evaluated. Then, the functionalization process is assessed as starting point for the evaluation of the oxygen release performances obtained inducing an AC magnetic field on the magnetic samples. Also the MDV process is checked, confirming that the oxygen release is actually induced by the magnetic field.

- **Chapter 5**: the last chapter summarizes the whole content detailed in this work, briefly explaining the motivation of the research, its scope and discussing the obtained results. Starting from these, moreover, for each section some possible future works are presented.

Chapter 2

Theoretical Background

The interaction between intense ultrasound waves and a liquid solution leads to the formation, growth and final collapse of bubbles, i.e. acoustic cavitation event [133]. Cavitation is the physical phenomenon at the base of the oxygen release in sono-sensitive oxygen nanocarriers.

This chapter has the aim to provide the theoretical framework necessary to understand the physical principles that are behind the experiments performed in this project. In the first part of the chapter, the laws derived from the interaction between US mechanical waves and sono-sensitive nanocarriers dispersed in a solution are described, focusing also on the different models that describe the bubbles behavior that lead to the cavitation phenomena.

The second part is instead centered on the explanation of the mechanism that induces US-induced phase-shift perfluorocarbon nanodroplets to pass from liquid to vapor phase, i.e. the ADV. This type of carriers exploits the fact that are synthesized in liquid phase and, by means of US, are able to vaporize and then to undergo cavitation for the oxygen release. In particular, first the thermodynamics behind phase transitions is proposed, starting from the intermolecular forces description until going through the Laplace pressure theory, that includes the size effects on vaporization mechanism. Secondly, the propagation of pressure wave and its interaction with the droplet itself is described, showing how the focusing effect due to the droplet-wave interaction increases the nucleation rate in the solution, giving an important contribution to the ADV initiation.

2.1 Acoustic Cavitation

Acoustic waves propagate through various media, such as air and liquids, at the speed of sound as a result of mechanical oscillations in pressure. The fundamental property that dictates wave propagation is its frequency, which in the case of sound waves, is determined by the number of pressure oscillations per second [134]. In the entire frequency spectrum of sound waves, ultrasound is defined as inaudible sound, characterized by frequencies above 20 kHz, although for practical purposes, this threshold is often shifted to frequencies above 10 kHz.
During each cycle, the pressure amplitude oscillates between positive and negative values relative to atmospheric pressure. When the amplitude is higher than the external pressure, the cycle results in a rarefaction phase, in which the instantaneous pressure is negative [135] and the force per unit surface area generated in a liquid leads to an expansion of the element.
Acoustic cavitation takes place when a time-varying pressure is superimposed on the steady ambient pressure of a solution [104]. Specifically, gas dispersed in the solution under this condition can no longer be dissolved in the liquid and induces the generation of bubbles. Regions in which gas is located are called weak spots and the number of these spots is proportional to the amount of generated bubbles. This kind of phenomenon is different with respect to boiling, due to the final collapse event of the bubble that characterizes cavitation. Regardless of the generation mechanism, bubbles grow with the same process related to the pressure variation cycle imposed by ultrasound. In acoustic cavitation, considering for simplicity a pre-existing bubble in solution in presence of a sinusoidal acoustic field (Figure 2.1), the alternating pressure variation imposed allows bubble to expand during the rarefaction phase and to compress during the positive peak of the acoustic cycle. This alternation of growth and compression lasts until bubble reaches a resonant size, that is only dependent on the acoustic field frequency, after which bubble finally collapses.

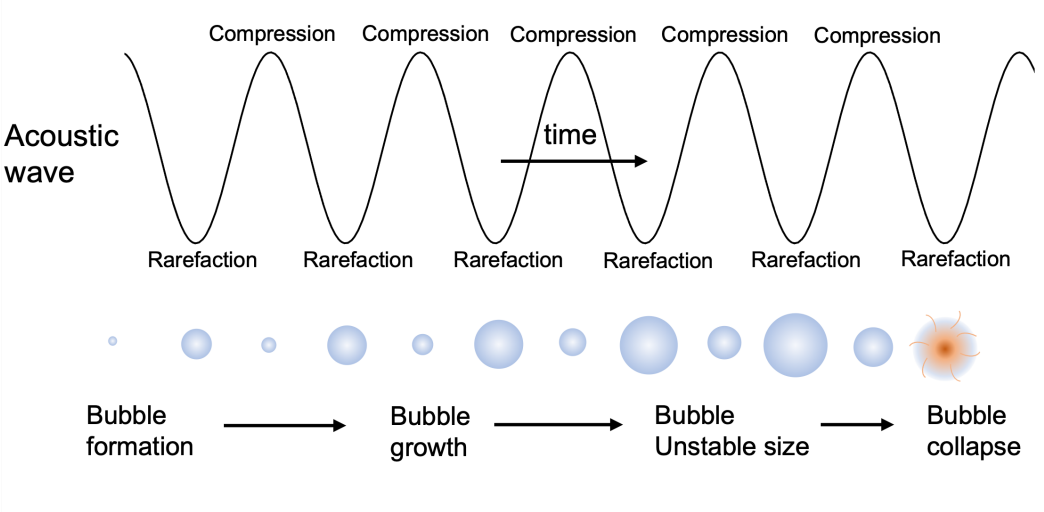

Fig. 2.1 Scheme of the bubble growth and final collapse under sinusoidal acoustic field.

The resonant size of bubbles can be easily derived, in a first analysis, through this formula:

$$\nu_0 R_r \approx 3 \text{ ms}^{-1} \tag{2.1}$$

where ν_0 is the resonant frequency and R_r is the resonant radius. Considering the ultrasound frequency range as 20 kHz $\leq \nu \leq$ 1 MHz, from Equation (2.1) it comes out that resonant size oscillates in the range of 3 µm $\leq r \leq$ 150 µm. Furthermore, depending on the finale bubble size, the cavitation effects are weaker or stronger so as different working frequency are exploited in different application fields of this phenomenon. Few acoustic cycles are usually enough to reach the resonance size, after which bubbles may undergo two different processes:

- *transient* or *inertial cavitation*, in which bubbles start being unstable and experience a final violent collapse;
- *stable cavitation*, in which bubbles stay stable in solution for many cycles oscillating around their resonant size.

The final bubble collapse is a quasi-adiabatic process during which considerable heat exchanges happen between inside and outside of the bubbles and, locally, both temperature and pressure undergo an intense increase reaching thousands of Kelvin and bars [136]. Moreover, shock waves are produced in the surrounding area of the bubbles after their implosion [137–139].

Another important consequence of bubble collapse is the dissociation of water vapor and oxygen due to this drastic increase of temperature and pressure, generating oxidants such as $(\cdot H)$ and $(OH\cdot)$ oxidizing solutes inside the solution [140].

2.1.1 Bubble Nucleation

In general, bubble nucleation occurs as a result of three main mechanisms [141]. The first mechanism takes place at the surface of solids, such as crevices of motes or particles, or the walls of a liquid container. In a crevice, for example, the gas pocket presents a concave surface in which the pressure inside the pocket is reduced by the surface tension of the pocket itself. The first mechanism takes place at the surface of solids, such as crevices in rocks or particles, or the walls of a container holding a liquid. The presence of an ultrasound field in the solution causes the gas pocket in the crevice to expand during the negative peak phase, leading to the diffusion of gas from the solution to the pocket and further decreasing the pressure inside the pocket. Conversely, during the compression phase, the pressure inside the pocket increases as the gas pocked is compressed. The rate of diffusion during expansion is higher than during compression, resulting in an overall growth of the gas pocket with each acoustic cycle. This is due to both the higher amount of gas diffusing into the pocket than the one diffusing out, being the available surface area larger during the compression phase compared to the expansion phase, as well as the thinner boundary layer during expansion as its volume is nearly constant over all the cycles.
The second mechanism for nucleation results from the presence of impurities in solution that act as cavitation nuclei [142]. This process is allowed by the fact that initially present bubble nuclei are stabilized against dissolution thanks to the presence on their surface of surfactants which strongly retard the gas diffusion across the bubble surface.
The last mechanism is related to the fragmentation of active cavitation bubbles [143]. This phenomenon comes from an initial bubble resulting unstable due to asymmetric acoustic environment reasons (presence of a neighbor bubble, solid object, liquid surface etc.) [144–146] that lead, under some specific conditions, to the generation of many tiny bubbles which behave as new cavitation nuclei [147, 148].

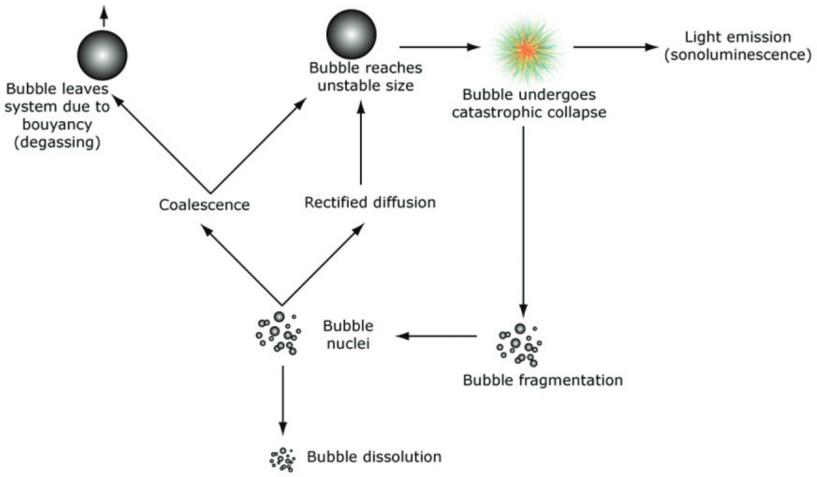

Fig. 2.2 Scheme of the cycle of gas bubbles in liquids under acoustic field [4]

2.1.2 Bubble and Acoustic Field

The Figure 2.2 illustrates the different processes that bubbles in a solution can undergo when interacting with an acoustic field. One such process is called *coalescence* in which two or more bubbles merge together to form a bubble of greater size. In a gas saturated solution, single bubbles can also expand over multiple acoustic cycles through a process known as *rectified diffusion*. If a bubble becomes large enough, it can rise to the surface of the solution due to buoyancy, a phenomenon referred to as *degassing*. Additionally, bubbles can also experience stable and then inertial cavitation, violently collapsing. Under certain conditions, this can lead to fragmentation into smaller bubbles emitting light under specific conditions. This phenomenon is known as *sonoluminescence* [149]. The behavior of bubbles can be predicted by taking into account factors such as its radius, the working acoustic frequency, the driving pressure, and the dissolved gas concentration.

2.1.3 Bubble Oscillator

Bubbles in a liquid solution can be modeled as an oscillatory system known as a *bubble oscillator* [150].The behavior of this system can be described though a set of physical laws by taking into account various parameters, including the external environment and the properties of the gas inside the bubble. The ultimate goal of this model is to derive a mathematical expression for the bubble's radius as a function of

time, known as the cinematic law of the bubble, represented by $R(t)$.
It is important to note that when modeling the bubble, it is generally assumed to be immersed in an infinite mass of homogeneous, incompressible fluid and initially in a spherical shape with a radius R_n at rest. These initial assumptions and all the parameters involved in the model description are shown in Figure 2.3.

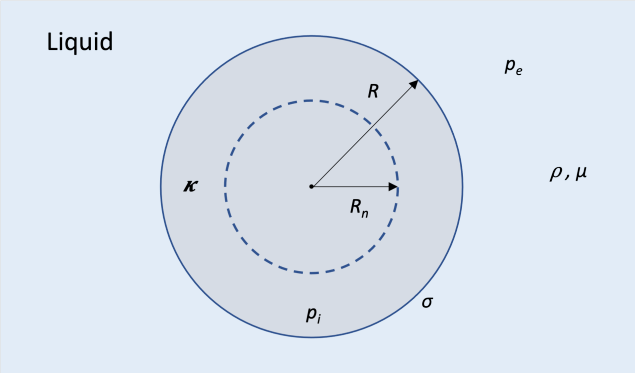

Fig. 2.3 Bubble parameters of bubble and liquid environment used to describe the oscillator system through the Reyleigh Model

The model used to start the description the behavior of bubbles in a liquid solution is known as the Rayleigh model [151]. This model takes into account various physical parameters, including the pressures inside and outside the bubble, represented by the variables p_{in} and p_e respectively. The polytropic exponent κ is also considered, which represents the ratio of specific heats of the gas and is important for describing adiabatic heat transfer across the bubble. Additionally, the density ρ, dynamic viscosity μ, and surface tension σ of the liquid are also taken into account.
The Rayleigh model describes the temporal evolution of the bubble radius through a second-order differential equation and is one of the most widely used and accepted model that describes the behavior of the bubble oscillator, and provides the starting point for describing the cinematic law of bubble $R(t)$:

$$\rho R\ddot{R} + \frac{3}{2}\rho\dot{R}^2 = p_{in} - p_e \tag{2.2}$$

in which the differentiation with respect to time is expressed by an overdot.
The left part of equation (2.2) shows the evolution of the system, where the coordinate reference system is transformed from the spherical three-dimension geometry to one radial dimension, while the right side indicates that the motion of the bubble

is mainly driven by the difference between pressures inside and outside the bubble. Pressures p_{in} and p_e become both radius R and time t dependent as soon as the gas fills the bubble, in addition to being dependent on the surface tension, liquid viscosity and applied acoustic field, leading the Reyleigh model to take the following form (Rayleigh-Plesset model [152–155]):

$$\rho R\ddot{R} + \frac{3}{2}\rho\dot{R}^2 = p_{gn}\left(\frac{R_n}{R}\right)^{3\kappa} + p_v - p_{stat} - \frac{2\sigma}{R} - \frac{4\mu}{R}\dot{R} - p(t), \tag{2.3}$$

where p_{gn} is the gas pressure inside the bubble at rest that can be written as dependent on the static pressure p_{stat} and the vapor pressure p_v:

$$p_{gn} = \frac{2\sigma}{R_n} + p_{stat} - p_v. \tag{2.4}$$

The term $p(t)$ represents an external pressure applied at the bubble surface. When dealing with a sinusoidal ultrasonic excitation of oscillation frequency ν_a and pressure amplitude p_a, this pressure can be expressed as:

$$p(t) = -p_a \sin(2\pi\nu_a t). \tag{2.5}$$

The negative sign is a mathematical convention assuming the oscillation starting with an expansion.
Joining equations (2.5) and (2.3) the fundamental equation of a single gas bubble under a sinusoidal acoustic field becomes:

$$\rho R\ddot{R} + \frac{3}{2}\rho\dot{R}^2 = p_{gn}\left(\frac{R_n}{R}\right)^{3\kappa} + p_v - p_{stat} - \frac{2\sigma}{R} - \frac{4\mu}{R}\dot{R} + p_a \sin 2\pi\nu_a t. \tag{2.6}$$

Through this final expression it is possible to describe the initial system, but other parameters deriving from the presence of sound radiation into the liquid due to the bubble oscillations cannot be taken into account. A more complete model is then the Gilmore model [156] that describes bubble surfaces as spherical loudspeakers that adsorb sound radiation. Furthermore, in case of strong oscillations, this model includes the Van der Waals law in order to consider the incompressibility of the gas inside the bubble. The model reads as:

$$\left(1 - \frac{\dot{R}}{C}\right)R\ddot{R} + \frac{3}{2}\left(1 - \frac{\dot{R}}{3C}\right)\dot{R}^2 = \left(1 + \frac{\dot{R}}{C}\right)H + \frac{\dot{R}}{C}\left(1 - \frac{\dot{R}}{C}\right)R\frac{dH}{dR}, \tag{2.7}$$

in which H represents the enthalpy defined as

$$H = \int_{p|_{r\to\infty}}^{p|_{r=R}} \frac{dp(\rho)}{\rho} \tag{2.8}$$

where $p(\rho)$ is the Tait equation describing the adiabatic heat transfer by means of the parameters A, B and n_T:

$$p(\rho) = A\left(\frac{\rho}{\rho_0}\right)^{n_T} - B, \tag{2.9}$$

$$p|_{r=R} = \left(p_{stat} + \frac{2\sigma}{R_n}\right)\left(\frac{R_n^3 - bR_n^3}{R^3 - bR_n^3}\right)^{\kappa} - \frac{2\sigma}{R} - \frac{4\mu}{R}\dot{R}, \tag{2.10}$$

$$p|_{r\to\infty} = p_{stat} + p(t), \tag{2.11}$$

$$C = \sqrt{c_0^2 + (n_T - 1)H}. \tag{2.12}$$

In particular, the parameters and variables introduced in the model are the sound velocity in the fluid at normal conditions c_0, the sound velocity at the bubble surface C and the Van der Waals constant b.
Featuring also a retarded time $t - R/c$ in the equations, the sound radiation from the oscillating bubble is incorporated, obtaining the Keller-Miksis model [157]. A model equivalent to the Keller-Miksis to first order in $1/c$ and dispensing with the retarded time is

$$\left(1 - \frac{\dot{R}}{c}\right)R\ddot{R} + \frac{3}{2}\left(1 - \frac{\dot{R}}{3c}\right)\dot{R}^2 = \left(1 + \frac{\dot{R}}{c}\right)\frac{p_1}{\rho} + \frac{R}{\rho c}\frac{dp_1}{dt}, \tag{2.13}$$

where

$$p_1 = \left(p_{stat} + \frac{2\sigma}{R_n}\right)\left(\frac{R_n}{R}\right)^{3\kappa} - p_{stat} - \frac{2\sigma}{R} - \frac{4\mu}{R}\dot{R} - p(t) \tag{2.14}$$

and $p(t)$ is the same as Equation (2.5). Again, the Van der Waals term can be introduced as defined in Equation (2.10).
Using for the parameters in (2.14) the values typical for a gas bubble in water, it is possible to evaluate the radius of the bubble at rest:

- $p_{stat} = 100$ kPa;
- $p_v = 2.33$ kPa;
- $\sigma = 0.0725$ Nm^{-1};

- $\kappa = 1.67$, assuming the gas inside the bubbles to be a noble gas;
- $\mu = 0.001$ MPa;
- $c = 1500$ ms^{-1};
- $\rho = 998$ kg m^{-3}.

From these, it can be proved that at rest the bubble radius R_n can cover a range from micrometers to several millimeters, depending on the driving frequency ν_a and the pressure amplitude p_a.
Models just described - Rayleigh-Plesset (2.6), Gilmore (2.7) and Keller-Miksis (2.13) - all three derived starting from Rayleigh theory, are able to provide an astonishing precise description of most of the experiments performed on oscillation phenomena of spherical bubbles. This has been proved, for instance, by Popinet and Zalski [158] exploiting the Rayleigh-Plesset model for the evaluation of the free, decaying oscillation of a bubble with radius at rest $R_n = 5$ μm in water. In particular, they compared their results with the Neiver-Stokes equation, used as reference, finding an error lower than 1% within six periods of the decaying oscillation.

2.1.4 The onset of stable and inertial cavitation

Safar derived the physical equations governing the bubble growth and the relative pressure thresholds at witch this event happens [159] and, soon after, Apfel exploited Safar's results in order to develop a series of prediction charts to illustrate the areas of the different cavitation activity [5]. Figure 2.4 shows an example of a prediction chart for a 10 kHz frequency system illustrating the areas of different cavitation activity:

- *Region A* - In these conditions, bubbles result under inertial control and their growth is only due to rectified diffusion, as will be discussed in section 2.1.5. As resonance regime is reached, characterized by a radius $R = R_r$, bubbles start a more violent behavior until collapse.
- *Region B* - Here bubble growth can be due either to rectified diffusion or to mechanical means [4], even if bubbles at the beginning are not transient. Until fragmentation occurs, bubbles stay in region C.

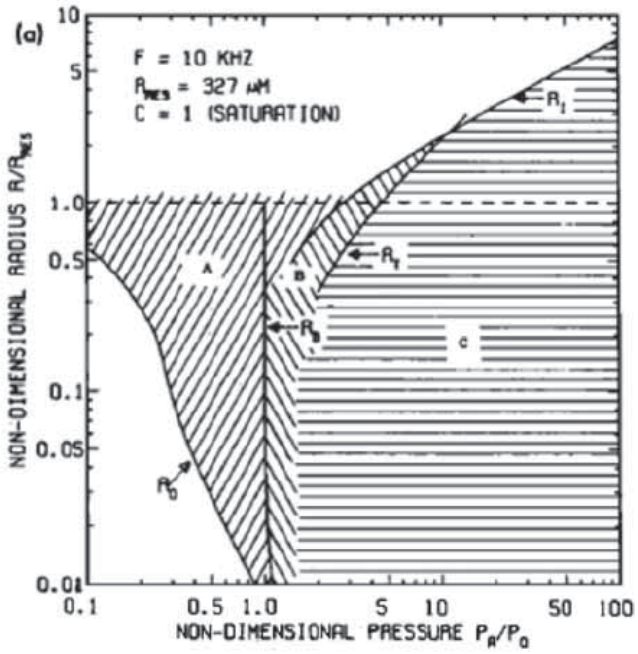

Fig. 2.4 Cavitation prediction chart for a 10 kHz system in a 100% gas saturated system taken from Apfel [5] showing the different cavitation regions bubbles can undergo.

- *Region C* - In this conditions bubbles stay in a transient region for cavitation: the boundary with region B represents the transient threshold, called *Blake threshold* [160].

Using Safar's equation the boundary rectified diffusion pressure P_D, representing the threshold between regions A and B, can be predicted:

$$\frac{p_D}{p_{stat}} = \frac{\left[3\mu\left(1+\frac{2\sigma}{p_{stat}R_D}\right)\right]\left[1-\frac{v_a^2}{v_{res}^2}\right]\sqrt{1+\frac{2\sigma}{p_{stat}R_D}-C_i/C_0}}{\sqrt{\left[6\left(1+\frac{2\sigma}{p_{stat}R_D}\right)\right]}}, \tag{2.15}$$

in which μ represents the fluid viscosity, v_a and v_{res} the driving and resonance frequencies, C_0 and C_i the concentrations of the gas dissolved in the solution at saturation and far from the considered bubble, respectively. Furthermore, the Blake threshold p_B can be evaluated through

$$p_B = p_{stat} + \frac{8\sigma}{9}\sqrt{\frac{3\sigma}{2\left[p_{stat}+\frac{2\sigma}{R_B}\right]R_B^3}}. \tag{2.16}$$

All this theory works well for predicting single bubbles behavior. For a multi-bubbles system the variety of pathways in which bubbles can enter make its study more complex to be predicted; thus, in order to understand bubbles dynamics it is prudent to start with the case of a single bubble in an acoustic field as discussed in section. 2.1.3

2.1.5 Growth of a bubble - Rectified diffusion

Rectified diffusion is a phenomenon that occurs when bubbles oscillate under an acoustic field. It is characterized by the unbalanced mass transfer across the bubble surface, leading to either bubble growth or dissolution.
When the pressure induced in the solution is greater than the rectified diffusion pressure, $p > p_D$, the bubble slowly grows. This is because the mass of gas that enters the bubble during the negative phase of the oscillation cycle is greater than the amount that exits during the positive one. Conversely, when the pressure is lower than p_D, the bubble dissolves as more gas exits the bubble than enters. This is due to the influence of the Laplace pressure generated by the surface tension acting on the surface of the bubble [161].
A theory proposed by Eller and Flynn explains this unbalanced mass exchange through two main effects: the area effect and the shell effect [162]. The area effect is related to the fact that the gas diffusion into the bubble occurs during the expansion phase when the bubble is bigger, while during the compression phase, gas is diffused out. Since the diffusion rate depends on the surface area available, a higher amount of gas goes into the bubble than out and thus, after some acoustic cycles, the bubble results in an overall growth.
The shell effect concerns the boundary layer (shell) through which the gas transfer physically occurs, as shown in Figure 2.5. In particular, the shell layer varies during the compression and expansion phases, leading to an increase and a decrease of its thickness, respectively. As a consequence, the concentration gradient is lower during compression, resulting in a smaller driving force for the mass transfer.
Eller and Flynn developed a mathematical model able to evaluate the change in the gas moles number in a bubble, through the equation:

$$\frac{dn}{dt} = 4\pi D R_n C_0 \left[\left\langle \frac{R}{R_n} \right\langle + R_n \sqrt{\frac{\langle (R/R_0)^4 \rangle}{\pi D t}} \right] H \tag{2.17}$$

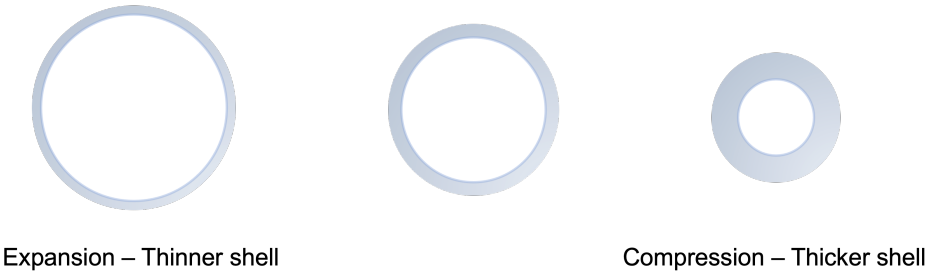

Fig. 2.5 Scheme of the thickness of the boundary layer (shell) of a bubble changing during its expansion and compression cycles, and showing how bubble expansion enhances the concentration gradient.

with

$$H = \frac{C_i}{C_0} - \frac{\left\langle \left(\frac{R}{R_n}\right)^4 \left(\frac{p_{in}}{p_{stat}}\right) \right\rangle}{\left\langle \left(\frac{R}{R_n}\right)^4 \right\rangle}. \tag{2.18}$$

In both the previous equations the angle brackets mean averaged values over time t, while D is the gas diffusivity through the shell and p_{in} the pressure inside the bubble. Starting from this, Crum added to Eller's model the thermodynamics of the process, obtaining the variation of the radius of a spherical bubble as function of time [161]:

$$\frac{dR_n}{dt} = \frac{Dd}{R_n}\left[\left\langle \frac{R}{R_n} \right\rangle \left(1 + \frac{4\sigma}{3p_{stat}R_n}\right)^{-1} H\right] \tag{2.19}$$

in which H is the enthalpy defined as in Equation (2.18). Introducing R_g as the universal gas constant and the absolute temperature T, d can be expressed as:

$$d = \frac{R_g T C_0}{p_{stat}}. \tag{2.20}$$

A more comprehensive model that builds upon the theory proposed by Eller and Flynn has been developed by Fryllas and Szeri. This model takes into account not only the area and shell effects, but also the movement of the boundaries of the bubble's shell [163, 164]:

$$\langle p[R(t)] \rangle = \frac{\int_0^{T_{osc}} R^4(t) p[R(t)] dt}{\int_0^{T_{osc}} R^4(t) dt} \tag{2.21}$$

in which $R(t)$ is the instantaneous bubble radius, $p[R(t)]$ the corresponding pressure inside the bubble and T_{osc} the period of the bubble oscillation. Using Equation (2.21),

an expression similar to eq. 2.19 can be obtained, with the form:

$$\frac{dR_n}{dt} = F(R, R_n, ...)\left[\frac{C_i}{C_g} - \frac{\left\langle \left(\frac{R}{R_n}\right)^{4-3\kappa} \right\rangle_{T_{osc}}}{\left\langle \left(\frac{R}{R_n}\right)^{4} \right\rangle_{T_{osc}}}\right] \tag{2.22}$$

where

$$C_g = \left(1 + \frac{2\sigma}{R_n p_{stat}}\right) C_0. \tag{2.23}$$

Considering the equilibrium conditions for which there is no net gas diffusion on average ($\frac{dR_n}{dt} = 0$), Equation (2.22) for the rectified diffusion becomes:

$$\frac{C_i}{C_0} - \left(1 + \frac{2\sigma}{R_n p_{stat}}\right) \frac{\left\langle \left(\frac{R}{R_n}\right)^{4-3\kappa} \right\rangle_{T_{osc}}}{\left\langle \left(\frac{R}{R_n}\right)^{4} \right\rangle_{T_{osc}}} = 0. \tag{2.24}$$

The above-described expression results in a complex formula able to express the typical bubble dimension at equilibrium under an acoustic field with amplitude p_a. The dependency on the applied pressure in the equation derives from $R(t)$, itself dependent on p_a.

From this equation, the value of the resonant frequency ν_{res} of a bubble during the rectified diffusion regime can be derived as follows:

$$\nu_{res} = \frac{1}{2\pi R_{n0}\sqrt{\rho}} \sqrt{3\kappa\left(p_{stat} + \frac{2\sigma}{R_{n=}} - p_v\right) - \frac{2\sigma}{R_{n0}} - \frac{4\mu^2}{\rho R_{n0}^2}}. \tag{2.25}$$

This result can be inverted in order to obtain the resonance size of the bubble. This final expression obtained is compatible with Rayleigh-Plesset (2.2), Gilmore (2.7) and Keller-Miksis (2.13) models.

A simplification of Equation (2.25) was then introduced by Minnaert [165] linearizing the previous expression resulting in a more straightforward formula for determining the resonance size of a bubble under rectified diffusion:

$$\nu_{res} = \frac{1}{2\pi R_{n0}} \sqrt{\frac{3\kappa p_{stat}}{\rho}}. \tag{2.26}$$

Considering an air bubble dissolved in water with $\kappa = 1.4$ and $\rho = 998$ kg m^{-3}, under a static pressure $p_{stat} = 100$ kPa, it comes out an expression very similar to Equation (2.1):

$$\nu_{res} R_{n0} = 3.26 ms^{-1}. \tag{2.27}$$

Considering again the US frequency range, typical resonance sizes of a bubble can vary from $R_{n0} \approx 3$ µm to $R_{n0} \approx 150$ µm.
To conclude this treatment, it has to be specified that bubbles are able to resonate not only at the fundamental driving frequency ν_0, but also at its multiple and submultiple values, leading to reach a series of differing resonance radii depending on the actual frequency they oscillate. In particular, if $\nu(n) = n \cdot \nu_{res}$ with $n = 1, 2, 3...$, the frequencies are integer multiple of the fundamental one and are called *harmonics frequencies*. If $\nu = \nu_{res} \cdot \frac{n}{2}$ (where $n = 1, 2, 3...$) other not integer multiple frequencies are involved, which are called *sub-harmonics* and *ultra-harmonics*.

2.1.6 The coalescence process

Up to now, the bubble growth treatment has been carried out considering only single bubble systems. In such a system, the main phenomenon leading to growth actually is rectified diffusion, as previously explained. However, in a more realistic scenario, there are typically a large number of bubbles interacting with each other. These multi-bubble systems can experience growth mechanisms beyond just rectified diffusion, making it important to consider the dynamics and interactions of multiple bubbles. Indeed, in parallel with rectified diffusion, growth is due also to *bubble coalescence* [166].
This process can be divided into three different phases, that are shown in Figure2.6 and described as:

1. Bubbles approaching, during which two bubbles with respectively radius R_1 and R_2 start moving in the fluid until getting sufficiently close. At this point, a quasi-equilibrium film with a thickness $\approx 1 - 10$ µm forms between them in a thermodynamically controlled process;

2. Thickness of the previous presented layer begins to reduce up to ≈ 100 nm due to gravity and suction forces. At this scale, the electric double layer (EDL) forces decrease while Van der Waals interactions increase, leading to a

metastable equilibrium. At this stage, it is possible for the film to roughly collapse interrupting the coalescence process and thus causing repulsion between starting bubbles;

3. In this final phase, if the metastable equilibrium is maintained, the film continues to further reduce its thickness below 10*nm*, eventually breaking and allowing the two bubbles to merge.

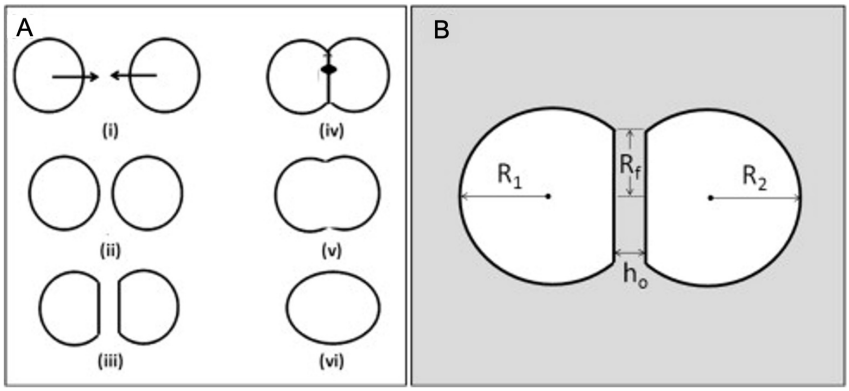

Fig. 2.6 A) Scheme of coalescing process of two colliding bubbles and B) variables used for two bubbles in contact [6].

Moreover, it has to be highlighted that the studies presented by Lee and Sunartio proved that coalescence phenomenon is similar in the case bubbles are excited by an acoustic field or not [148, 167].

2.1.7 Inertial Cavitation and its applications: sonochemestry and ROS generation

Inertial cavitation has been first described by Rayleigh [151], which provided a mathematical expression of this phenomenon through the derivation of a scaling law of the radius variation in time.
According to the results he obtained, during their expansion, bubbles are able to store a certain amount of potential energy. This energy increases over each acoustic cycle up to its maximum value when bubbles reach the critical sizes. At that point, bubbles collapse and convert this potential energy into kinetic one, causing a high-velocity fluid motion in the surrounding environment. This motion results to be characterized by a velocity higher than the sound speed, and, as a consequence, the

gas stored into the bubbles is violently ejected. During this final collapse, bubbles reduce their radius, drastically increasing the gas density inside, due to the fact that the gas molecules approach each other until the Van-der Waals repulsive forces dominate, and bubbles stop to compress. This phase can be treated as an almost adiabatic phenomenon that results in a sharp rise of the local temperature of the order of thousands of degrees. Studying the flux of heat exchanged between inside and outside the bubble [168], the temperature during each bubble phase can be evaluated through the equation:

$$\frac{T_R - T_0}{T_C - T_R} = \sqrt{\frac{K_g c_{pg} \rho_g}{L_l c_{pl} \rho_l}}. \tag{2.28}$$

T in equation (2.28) represents the absolute temperature respectively associated to the bubble surface (T_R), to the liquid away from the bubble (T_0) and to its center (T_C); K instead is the thermal conductivity and ρ and c the density and the specific heat associated respectively to the gas (X_g) and the liquid (X_l).
The value of the temperature that can be reached during the bubble collapse, thus related to the minimum bubble radius reached, can be evaluated through the estimation obtained by Noltingk and Neppiras [155]:

$$T(R_{min}) = T_0 \Big(\frac{R_i}{R_{min}} \Big)^{3(\kappa-1)}, \tag{2.29}$$

where R_{min} is the minimum radius reached during this process and R_i the starting radius for the adiabatic process. From Equation (2.28), it can be derived that the temperature is dependent on κ, meaning that monoatomic gas molecules (higher κ) generate higher temperature increase with respect to polyatomic ones (lower κ). Equation (2.29) is instead useful for the understanding sonochemistry, one of the main ultrasound application.
Sonochemistry is a brunch of chemistry that uses ultrasound in order to induce chemical reactions driven by acoustic cavitation [169]. As already explained, within inertial cavitation, very high temperatures are induced and the solvent vapor and gas molecules present inside the bubbles undergo endothermic chemical reactions that lead to the generation of highly reactive radical species.
Considering, for instance, bubbles in a water based environment, the main acoustically catalyzed reaction is the water dissociation:

$$H_2O \rightarrow H \cdot + \cdot OH, \tag{2.30}$$

that leads to the production of hydrogen atoms ($\cdot H$) and hydroxyl radicals ($OH\cdot$) [170]. These last result highly reactive and, in turn, can interact with other free radicals or ions present in solution. In particular, the hydroxyl radical OH^* assumes high importance since it is responsible for oxidizing chemical reactions.

2.2 Phase-shift Perfluorocarbon Nanodroplet Vaporization

In 1998, Apfel revolutionized the field of drug delivery systems with the development of nanometer-sized droplets with a perfluorocarbon core, capable of converting into microbubbles under ultrasound stimulus [171]. This discovery paved the way for the development of various phase-changing nanodroplets solutions with a fluorocarbon core, coated with lipid, protein, or polymer shells to improve their stability in aqueous solutions [172, 105, 173]. More in general, these submicron-diameter liquid emulsion particles, known as nanodroplets, can be converted into gas bubbles through thermal, mechanical, or electromagnetic energy, a process known as vaporization [8]. Upon vaporization, nanodroplets expand from a few hundred nanometers to a few microns and, interacting with an US field, are capable of undergoing cavitation phenomena. In this chapter, we will first discuss the intermolecular forces and the construction of the equilibrium phase diagram. Next, we will present the main theories developed to describe the vaporization of nanodroplets and their significance in the field of drug delivery systems.

2.2.1 Intermolecular Forces and Equilibrium Phase Behavior

Vaporization is the transition from the liquid to gas phase based on the balance between intermolecular pair potentials and thermal energy [174]. For vaporization to occur, the momentum transfer during molecular collisions must be strong enough to overcome Van der Waals attractive forces, leading molecules to transition from an organized state to a chaotic one [175].
Different sources can be exploited to provide the energy necessary for inducing vaporization, and among these sources, acoustic fields are particularly useful. ADV is the process that utilizes ultrasound to induce vaporization in a liquid [176]. The concept of ADV is rooted in thermodynamics, specifically the relationship between

phase state, phase change, and vapor pressure. The vapor pressure is defined as the pressure of a gas in equilibrium with the liquid or solid in a closed system at a given temperature. This pressure is proportional to the temperature of the condensed phase and represents the force exerted by molecules attempting to escape the liquid or solid and form a gas phase.
The boiling point of a liquid is defined as the temperature at which the vapor pressure is equal to 1 atm, marking the point of equilibrium between the gas and liquid phases. Above the boiling point, the liquid boils, while below it, the liquid condenses to gas. ADV leverages this relationship by manipulating the local pressure of the liquid through sound waves, causing the phase transition from liquid to gas or vice versa, without involving any temperature increase.
Going further into the classical phase shift description, it is important to note that the stability of molecules in gas and liquid phases governs this transition. In gas phase, the orientation of molecules results in a lack of constant shape and volume, while in the liquid phase, the volume remains constant but the shape does not. During vaporization, the transition from a more organized state (liquid) to a disordered state (gas) requires an increase in kinetic energy to overcome intermolecular attraction forces. These intermolecular attraction and repulsion energies can be described by the Lennard-Jones 6-12 potential [177, 7], whose trend can be seen in Figure 2.7, as:

$$\Phi_{LJ} = 4\varepsilon\left[\left(\frac{r_0}{r}\right)^{12} - \left(\frac{r_0}{r}\right)^{6}\right] \tag{2.31}$$

where ε is the depth of the molecular potential well, r describes the distance between molecules centers and r_0 the same distance at minimum potential condition. The Lennard-Jones potential theory is a molecular interaction model that describes the potential energy resulting from electrostatic interactions between molecules. This potential energy is composed of an attractive long-range component due to Van der Waals forces and a hard sphere repulsion [178]. The Van der Waals attraction forces involve interactions between two permanent dipoles (Keesom energy), between a permanent dipole and an induced dipole (Debye energy), and between two induced dipoles (London energy). As a result, molecules tend to occupy a state of minimum energy that balances the ability to move freely within a certain range [179]. Overcoming the attraction forces allows matter to transition from a liquid state to an infinitely dispersed gaseous state. Variations in temperature or pressure within the system can manipulate the kinetic energy associated with the Van der Waals

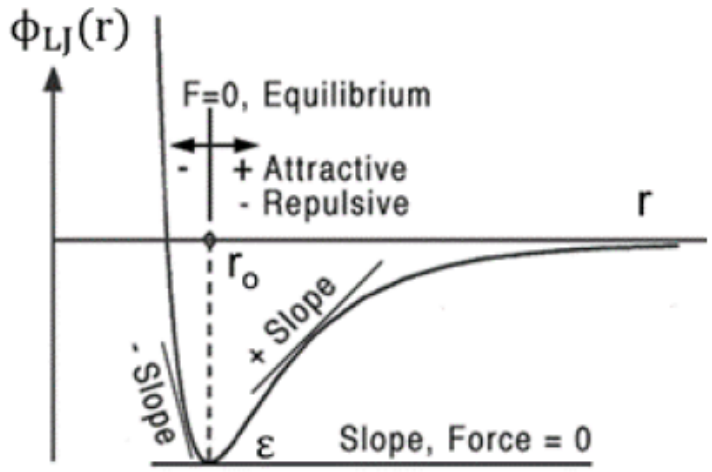

Fig. 2.7 Lennard-Jones 6-12 potential diagram [7].

potential, dictating the physical state of matter..
However, the Lennard-Jones does not delve into the specifics of what occurs when thermal energy is applied to a material. For this purpose, statistical and classical phase-change thermodynamics are now studied more deeply. Statistical thermodynamics establishes the relationship between pressure p, temperature T, and a specific material phase, which is defined as:

$$p = k_B T \left(\frac{\partial \ln Q}{\partial V} \right)_{T,N} \tag{2.32}$$

with k_B the Boltzmann constant, V and N the volume and mole number respectively, and $\ln Q$ the canonical partition function taking into account all the possible molecular orientations at the thermal equilibrium, as described by Carey [174].
Combining Equation (2.32) with the canonical partition function, the pressure expression, dependent on temperature and volume, normalized respect to the number of moles N and the molecular mass $\bar{M}$, can be derived as:

$$p = \frac{R_g T}{v - b_v} - \frac{a_v}{v^2} \tag{2.33}$$

with the universal gas constant R_g equal to:

$$R_g = \frac{N_A k_B}{\bar{M}}, \tag{2.34}$$

N_A the Avogadro number, v the specific volume and a_v and b_v the Van der Waals constants:

$$a_v = \frac{27(\bar{R}_g/\bar{M})^2 T_C^2}{64 p_C} \tag{2.35a}$$

$$b_v = \frac{(R_g/\bar{M}) T_C}{84 p_C}, \tag{2.35b}$$

with p_C and T_C are the critical pressure and temperature, i.e. the temperature at which no gas is present in the solution unless it reaches its critical pressure [180]. Joining Equation (2.34) and (2.35), the reduced equation of state is obtained:

$$p_r = \frac{8T_r}{3v_r - 1} - \frac{3}{v_r^2}, \tag{2.36}$$

in which X_r stands for reduced value, i.e. normalized respect its critical value ($T_r = T/T_C$). The statistical thermodynamic dependence between temperature, volume and pressure can be appreciated in Figure 2.8A. For temperatures below the critical value (blue and orange lines), a local minimum and a local maximum can be appreciated, meaning that considering as constant both reduced pressure and temperature, three values of reduced volume can exist simultaneously, indicating the coexistence of multiple physical states. Following the classical thermodynamics, a substance is allowed to undergo a phase transition only passing through an equilibrium state in which the chemical potential is the same for both vapor and liquid phases. Therefore, considering a reduced pressure, an isobaric line can be built between the two phases allowing equal probability (Figure 2.8B). This condition of equal probability is ensured by the fact that the areas of the regions above and below the isobaric line (A and B) are the same. Figure 2.8C shows the saturation curve obtained through the isobaric lines. A saturation curve describes the conditions for liquid and gas to change their phase, neglecting anyway the possibility of a multiphase stadium. This curve is then used for generating the equilibrium P-V phase diagram (Figure 2.8D) where the regions of pure vapor, liquid and vapor-liquid coexistence are represented.

2.2.2 Laplace pressure theory

Including in the treatment the size effects associated to nanoscale droplets, the Laplace pressure needs to be taken into account for the phase-transition phenomena description. Laplace pressure is defined for a spherical surface of radius R_n and

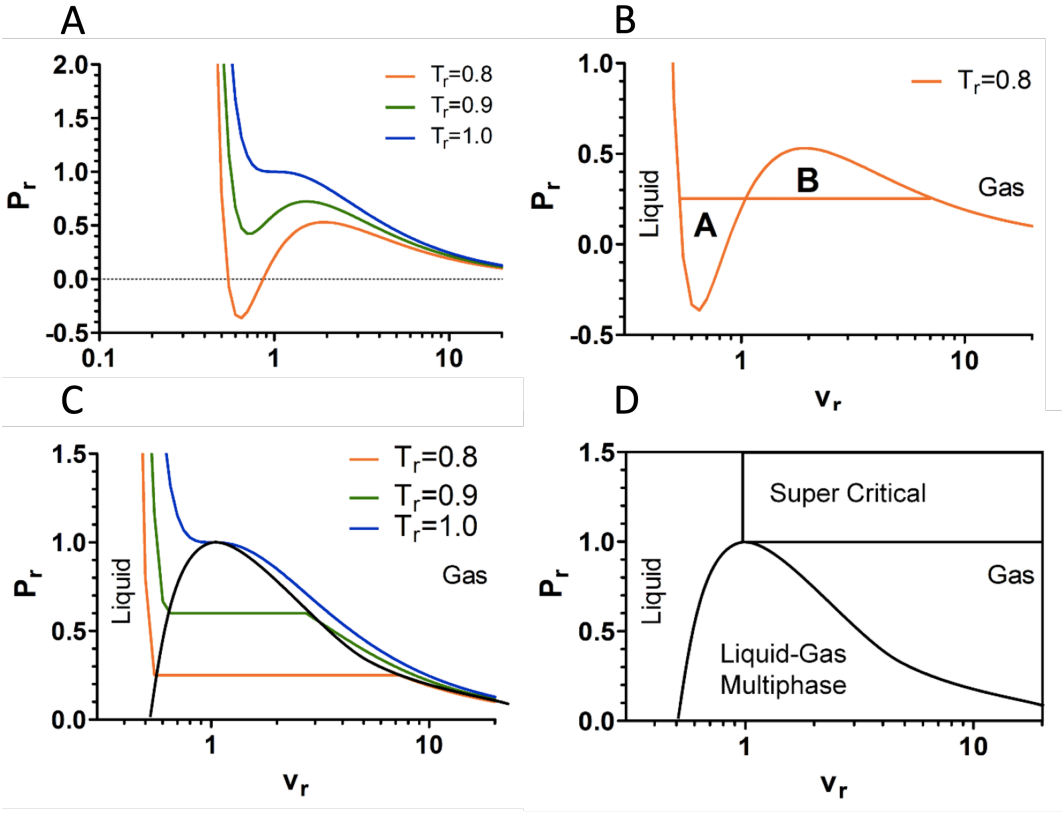

Fig. 2.8 Plot of the reduced Van der Waals equation of state (2.36) [8]. A) Plot showing the dependence of the pressure on temperature and volume. B) Plot enhancing the isobaric line for a vapor-liquid transition at a specific temperature in which the regions A and B have the same area (equal probability), meaning equal chemical potential. C) Saturation curve (black line) built starting from the isobaric lines drawn on the pressure-volume curves. D) Reduced pressure-specific volume liquid-gas phase diagram at fixed temperature.

surface tension σ as the difference between pressure inside and outside the droplet:

$$\Delta p = p_{in} - p_e = \frac{2\sigma}{R_n}. \tag{2.37}$$

This is an additional pressure that nanodroplets undergo due to the surface tension between the two immiscible phases that compresses the content (liquid or gas) of the droplet [176]. Under equilibrium conditions, the liquid inside nanodroplets will never experience a phase transition to gas due to the effect of Laplace pressure, which is directly proportional to the inverse of droplets dimension ($\propto 1/R_n$). This is because the liquid is contained within a small dimensional system, resulting in a very intense Laplace pressure confinement. This particular condition is called

superheating. Vaporization of liquid droplets to bubbles involves surface expansion and thus can be affected by two physical entities, Laplace pressure and interfacial tension that is the cohesive force holding the liquid molecules together at the surface. In order to better understand the role of Laplace pressure in the droplet vaporization, one now considers the case of C_3F_8 and C_4F_{10} droplets and their relative pressure-temperature diagrams, as shown in Figure 2.9. It has been shown that the interfacial

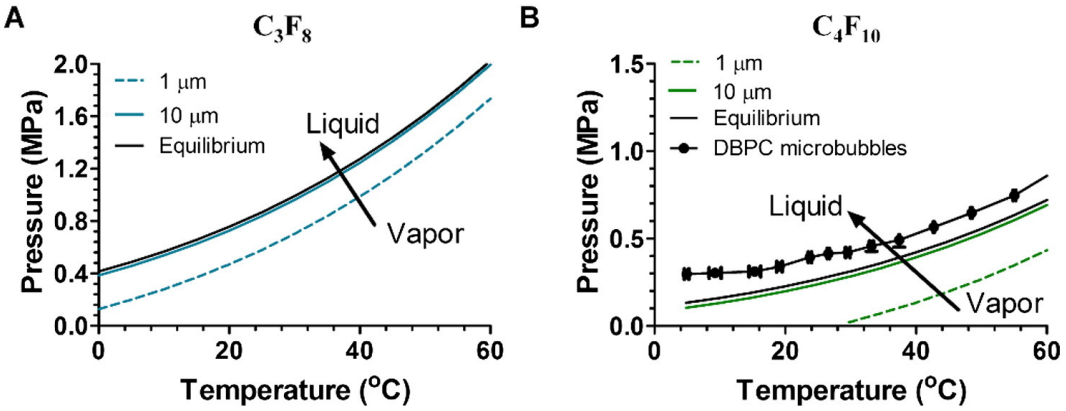

Fig. 2.9 Role of the Laplace pressure in the pressure–temperature phase diagrams for C_3F_8 A) and C_4F_{10} B) [8].

tension during expansion phase passes from 0 to 73 mN/m [181] and it is useful to investigate the Laplace pressure influence in the phase diagram. Laplace pressure induces a shift in the P-T diagrams such as a lower pressure or higher temperature is required for droplet vaporization, providing an explanation to the remarkable metastability of superheated droplets. Starting from this consideration, the Antoine equation can be used to correlate vapor pressure P_{out} and boiling temperature T_b [182]:

$$T_b = \frac{B}{A - \log_{10}\left(P_{out} + \frac{2\sigma}{R}\right)} - C \tag{2.38}$$

where A,B and C are dimensionless empirical constant depending on the material. This equation can be used to estimate the ultrasound peak negative pressure (PNP) needed for submicron droplet vaporization evaluating the difference between the droplet pressure P_{in} and the equilibrium vapor pressure P_{sat} at specific temperatures. Figure 2.10 shows how the Laplace pressure theory explains the dependence of the pressure required fot vaporization on the droplet dimensions. Specifically, from this results that smaller is the droplet diameter higher will be the PNP necessary for inducing acoustic vaporization.

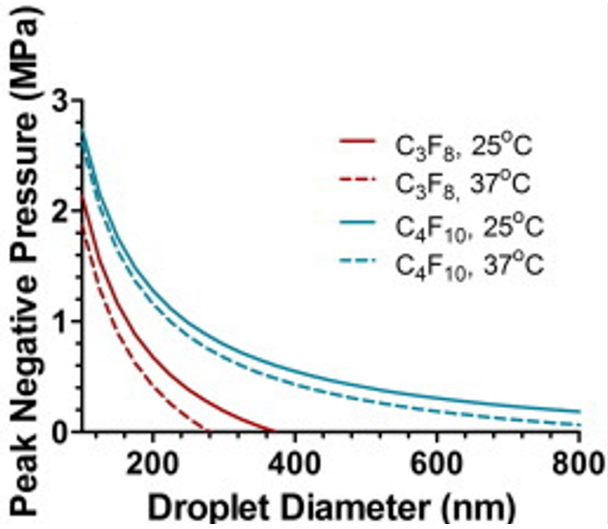

Fig. 2.10 Theoretical ultrasound PNP trend respect to droplet size predicted through Antoine equation [8].

Chapter 3

Methodology

In this chapter, a comprehensive overview of the materials and methods employed in the experiments is presented. Specifically, the evaluation method for uncertainties, following the guidelines provided by the Joint Committee for Guides in Metrology (JCGM), is presented first in order to provide systematic and consistent measurements and results.
Then, since this work is divided in two parts - one related to the characterization of OLNDs cavitation mechanism and the second to the functionalization with magnetic nanoparticles - a detailed description of the techniques and the processes used to obtain the results is provided for each section.

3.1 Uncertainty of Measurements

The aim of a measurement is to provide numerical information about a physical or chemical process, which helps in understanding the obtained data more effectively [183]. However, it is essential to note that the outcome of a measurement is never exact and is always dependent on several factors such as the measuring system, the procedure used, the operator's skills, and other potential sources of error that must be taken into account [184].
Measurements are associated with two types of error: random and systematic errors. Random errors are obtained when the same quantity is measured several times under the same conditions and a different value is obtained each time. In order to obtain a more reliable measurement, multiple values are measured and their average is

calculated along with the dispersion, which indicates how well the measurement was made.
The measuring system must provide values that are not dispersed with respect to the true value of the quantity, but with respect to an offset value. The difference between the offset value and the true value is called the systematic error, which is a constant component of error or one that depends on other quantities in a specific and known way.
For ensuring high-quality measurements, both types of errors must be accounted for through a probabilistic method based on the concept of measurement uncertainty. It is important to note that it is not possible to determine the exact true value of a measurand, but only to estimate it based on the level of uncertainty, which reflects the incomplete knowledge of the measurand. From a metrological perspective, the notion of "belief" is crucial, as the results of a measurement must be quantified in terms of probability, which represents the degree of belief.

3.1.1 Guide to the Expression of Uncertainty in Measurement

The JCGM promotes a Guide to the Expression of Uncertainty in Measurement (GUM) to establish general rules for the evaluation of uncertainty in measurement in different fields [185]. The principles of the Guide are thus aimed to cover a broad spectrum of measurements, from the basic research to the production industry, passing through the standards calibration and regulations.
This document first gives a definition of uncertainty related to the measurement of a well-defined physical quantity, the so-called measurand, that can be defined by an essentially unique value. Here follows a set of definitions given in the Guide [186]:

- the *measurement* is the sequence of operations performed to determine the value of a quantity;
- the *value* represents the magnitude of a quantity expressed as a unit of measurement multiplied by a number;
- the *measurand* is a particular quantity to be measured;
- the *method of measurement* relies to the generic logical set of operation exploited during the performance of measurements;

- the *measurement procedure* is the specific sequence of operation used in the performance of a particular measurement according to a given method.
- the *result of a measurement* is an estimation of the value attributed to a measurand obtained by a measurement;
- the *uncertainty* is a parameter associated with the result that indicates the degree of reliability in the result;
- the *accuracy* is the closeness of the agreement between the result of a measurement and the respective true value;
- the *precision* instead is the closeness of agreement between indications or measured quality values obtained by replicate measurements on similar objects under specified conditions (repeatability or reproducibility);
- *repeatability* of reasults is the closeness of the agreement between the results of successive measurements of the same measurand performed under the same repeatability conditions (same procedure, observer, instrument, location etc.);
- *reproducibility* relies to the closeness of agreement between the results of the same measurand carried out under changed conditions that have to be stated.

Performing a set repeated measurements, variations on the observations arise due to influence quantities, that are not the measurand but that affect the result of the measurement. Furthermore, also the mathematical model of the measurement used to transform the set of repeated observations into the result includes various influence quantities that are inexactly known. All this lack of knowledge gives a contribution to the uncertainty of the result. In practice, uncertainty derives from many possible sources, including the incomplete definition of the measurand, its imperfect realization, the non-representative sampling, an inadequate knowledge of the effects of environment conditions, personal bias in reading analogue instruments, instrument resolution, inexact references, constants and external parameters, approximations and variations.
GUM classifies uncertainty into two types: Type A and Type B. Both types of uncertainty are based on probability distributions and can be quantified using variances or standard deviations. Type A uncertainty is obtained through statistical analysis of a set of measurements, while Type B uncertainty is derived from data obtained

through calibration certificates, scientific judgment, or references. Although both types of uncertainty provide similar information, they differ in their emphasis on the procedures used to obtain the data.

3.1.2 Direct Measurements

The method used to evaluate uncertainty depends on the nature of the measurement being performed, whether it is direct or indirect. For a set of direct measurements of a quantity X $(x_1, x_2, ..., x_n)$, the first step is to identify and discharge any gross errors. Gross errors are measurand values that deviate significantly from the other values, and their recognition depends on the evaluation of the investigator. It can be caused by both investigator itself and also momentary conditions or disruptions.
In the case of type A uncertainties, the set of independent observations q_k performed is considered as a n-element random sample of the infinite set of values, from which the arithmetic mean value, its standard deviation and the degrees of freedom v_k for $u(q)$ can be extracted, as defined in the following expressions:

$$\bar{q} = \frac{1}{n} \sum_{k=1}^{n} x_k. \tag{3.1a}$$

$$u(q_k) = \sqrt{s(q_k)^2} = \sqrt{\frac{1}{n(n-1)} \sum_{j=1}^{n} (q_j - \bar{q})^2} \tag{3.1b}$$

$$v_k = n - 1 \tag{3.1c}$$

where s^2 and $u^2(\bar{q})$ have equivalent meaning and stand for squared experimental standard deviation and squared experimental variance of the mean value. The degrees of freedom associated with a certain uncertainty is a parameter counting how good is the estimation of the standard uncertainty.
Type B standard uncertainty is crucial, particularly when repeated observations are not feasible. In such cases, uncertainty is assessed through scientific judgment that takes into account all available information on the potential variability of x_i, such as previous measurement results, general understanding of the behavior of materials and instruments, manufacturer specifications, data provided in calibrations, and uncertainties assigned to reference data. For Type B uncertainty, the degrees of

freedom can be evaluated as:

$$v_i \simeq \frac{1}{2}\left[\frac{\delta u(x_i)}{u(x_i)}\right]^{-2} \tag{3.2}$$

being an indication of how how much standard uncertainty is reliable.
If the value x_i is for instance taken from manufacturing specifications, calibration data or other sources, the uncertainty results to be the standard uncertainty $u(x_i)$ divided by a multiplier and its correspondent variance is the square of that quotient. In other cases it can be found that the quoted uncertainty defines an interval with a specific level of confidence in percentage.
When the result of a measurement is obtained by a certain number of different quantities, also the final overall uncertainty - combined uncertainty - is given by considering each contribution, following the formula:

$$u_C = \sqrt{u_A^2 + u_{B1}^2 + u_{B2}^2 + ... + u_{Bm}^2} \tag{3.3}$$

Starting from this, the concept of extended uncertainty $U(\bar{x})$ is introduced in order to make possible comparisons of measurement results performed with different conditions and in different laboratories. In this case, the standard uncertainty of x_i is evaluated dividing the quoted value by a specific coverage factor k:

$$U(\bar{x}) = k \cdot u_C(\bar{x}). \tag{3.4}$$

The value of this factor depends on the type of probability distribution associated to the specific measurement through which results are modeled and on the desired coverage probability, i.e. the the fraction of the distribution of values that can be reasonably attributed to the measurand. For instance dealing with a Gaussian distribution, $k = 2$ associates a level of confidence of 95%, while $k = 3$ associates the 97%.
In case of a coverage of 100% the concept of tolerance is obtained. This is defined as the maximum expected amplitude range around the result of a measurement including all the possible values attributed to the measurand. In Figure 3.1 and Table 3.1 are showed the shape and the coverage factors related to the normal distribution respectively.

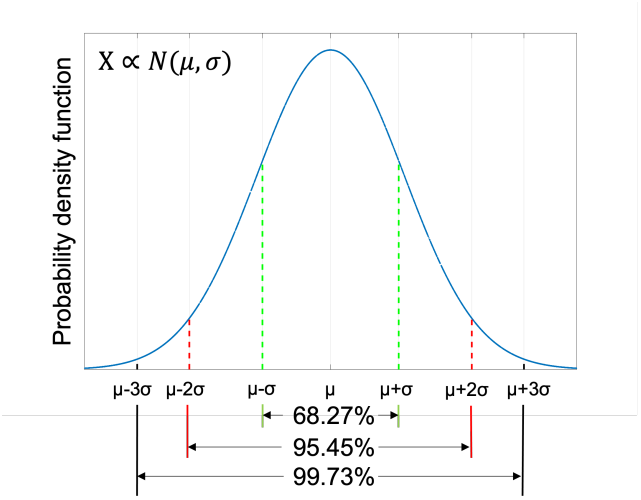

Fig. 3.1 Gaussian (Normal) probability density function showing the range of values covered for three different levels of confidence.

Table 3.1 Coverage factors and relative percentages of coverage relative to the normal distribution.

Level of confidence (%)	**Coverage factor** k
67.28	1
90	1.645
95	1.960
95.45	2
99	2.576
99.73	3

3.1.3 Indirect Measurements

In case of indirect measurements, the measurand cannot be compared to a reference quantity, but its value is obtained by processing the results of one or more direct measurements carried out on quantities related to it.
An indirect measurement, therefore, assumes the existence of an analytical model

$$y = f(x_1, x_2, ..., x_i, ..., x_m) \tag{3.5}$$

that relates the m measurements x_i of the quantities $q_1, ...q_m$ to the measurement y of the quantity q_0. The presence of the model implies an additional uncertainty, referred to as "model uncertainty": $f(...)$ does not exhaustively describe the relationships in the empirical world. Therefore, the model may not perfectly capture the true underlying relationship between the measured quantities, which can lead to errors in the final result. It is important to account for this source of uncertainty in the evaluation of the overall uncertainty of the indirect measurement. The evaluation of uncertainty for indirect measurements typically involves propagation of the uncertainty associated with the underlying quantities used in the calculation. According to the GUM, the uncertainty in an indirect measurement is typically estimated using the law of propagation of uncertainty (LPU), which provides a way to calculate the combined standard uncertainty of a quantity resulting from the combined effects of the uncertainties in the measured variables used in the calculation.
LPU is based on a first-order Taylor series approximation of the measurement model f, for which the output combined uncertainty related to y can be expressed as:

$$u_C^2(y) = \sum_{i=1}^{N} \left(\frac{\partial f}{\partial x_i}\right)^2 u^2(x_i) + 2\sum_{i=1}^{N-1}\sum_{j=i+1}^{N} \frac{\partial f}{\partial x_i}\frac{\partial f}{\partial x_j} u(x_i, x_j), \tag{3.6}$$

where $u(x_i)$ is the standard uncertainty associated with x_i, $\frac{\partial f}{\partial x_i}$ the sensitivity coefficient describing how the output estimate y varies with changes in the values of the input estimate x_i and $u(x_i, x_j)$ the covariance between X_i and X_j.
In case the input quantities are uncorrelated, Eq. (3.6) becomes:

$$u^2(y) = \sum_{i=1}^{N} \left(\frac{\partial f}{\partial x_i}\right)^2 u^2(x_i) = \sum_{i=1}^{N} u_i^2(y) \tag{3.7}$$

The propagation of uncertainty formula can be applied to any indirect measurement, and is an essential tool for evaluating the uncertainty associated with such measurements. By accounting for the uncertainty in the underlying measurements, the uncertainty in the final result can be estimated, providing a measure of the reliability of the measurement. In conclusion, the evaluation of uncertainty for indirect measurements requires careful consideration of the underlying measurements used in the calculation. The law of propagation of uncertainty provides a mathematical framework for estimating the uncertainty in the final result, and is essential for ensuring the accuracy and reliability of the measurement.

Following the discussion of measurement uncertainty and the law of propagation, limited examples of uncertainty propagation in indirect measurements will be provided, which are relevant to the subsequent results presented.
For example, consider the measurement of a quantity C deriving from the sum or the difference between two quantities directly measured, A and B, so as $C = A + B$ or $C = A - B$, each characterized by its uncertainty already known u_A and u_B. For both cases, Eq.(3.6) becomes:

$$u_C^2 = u_a^2 + u_b^2. \tag{3.8}$$

Dealing with the measurement of the velocity of an object v, for instance, involves the indirect measurement of distance x and time t. Suppose that the distance measurement has an uncertainty of u_x and the time measurement has an uncertainty of u_t. The velocity v is calculated as the ratio of distance over time, $v = x/t$. The uncertainty in the velocity, u_v, can be estimated using the law of propagation of uncertainty, which states that:

$$u_v = \sqrt{\left(\frac{\partial v}{\partial x} u_x\right)^2 + \left(\frac{\partial v}{\partial t} u_t\right)^2}$$

where $\left(\frac{\partial v}{\partial x}\right)$ and $\left(\frac{\partial v}{\partial t}\right)$ are the partial derivatives of v with respect to x and t, respectively.

For the velocity example, we have $\left(\frac{\partial v}{\partial x}\right) = \frac{1}{t}$ and $\left(\frac{\partial v}{\partial t}\right) = -\frac{x}{t^2}$. Therefore, the uncertainty in the velocity is:

$$u_v = \sqrt{\left(\frac{u_x}{t}\right)^2 + \left(\frac{x}{t^2} u_t\right)^2}$$

3.2 Multiple Approaches for Ultrasonic Cavitation Monitoring

The aim of the first part of this study was focused on the characterization of the signals emitted by US-sensitive nanocarriers during the interaction with an acoustic field. To achieve this, three different sensors were used to collect acoustic, ecographic and optical responses generated by two differently coated DFP-based OLNDs and

sono-sensitive porous nanoparticles. The methods used to conduct this investigation are described, beginning with the synthesis procedure of the nanodroplets and the experimental setup, followed by the improvements made to overcome certain limitations.

3.2.1 OLNDs Preparation and Characterization

In this first part, two types of liquid nanodroplets were prepared and characterized. DFP was used as core PFC material, while polyvinyl-alcohol (PVA) or chitosan were employed as polymeric coatings.
To produce the liquid formulation of OLNDs, first a mixture composed of 1.5 mL of PFC, 1.8 mL of solution of Epikuron 200 (1%) and palmitic acid (0.3%) in ethanol, and 0.5 mL of Polyvinylpyrrolidone (PVP) in water solution (0.5%) were homogenized in 30 mL of deionized water at 24000 rpm through Ultra-Turrax SG215 homogenizer for 2 min. The resulting solution was then saturated with O_2 for more 2 min with a constant flow rate reaching a final concentration of 35 $mg\ L^{-1}$, followed by the final homogenization of the mixture at 13000 rpm for 2 more minutes, during which 1.8 mL of coating was added drop-wise [91]. The polymeric solution for the coatings were prepared starting from commercial low molecular weight chitosan (Sigma-Aldrich) and polyvinyl alchol 99% hydrolyzed (Sigma-Aldrich), with a concentration of 2.7% in acetate buffer solution and deionized water, respectively. The final structure of a liquid nanodroplet is schematized in Figure 3.2.

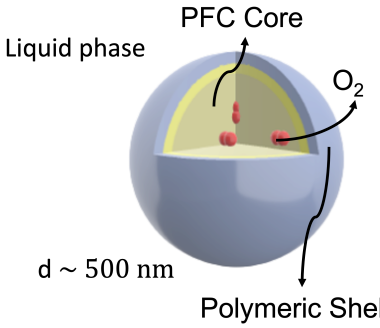

Fig. 3.2 Scheme of the final OLND.

The OLNDs suspensions were characterized in their size distribution using Dynamic Light Scattering (DLS) technique (Delsa Nano C Particle Analyzer, Beckman

Coulter) and in terms of shape using optical microscopy. Figure 3.3A hows the dimension distribution of chitosan-coated OLNDs measured by DLS, while Figure 3.3B displays the PVA-shelled droplets observed under an optical microscope.

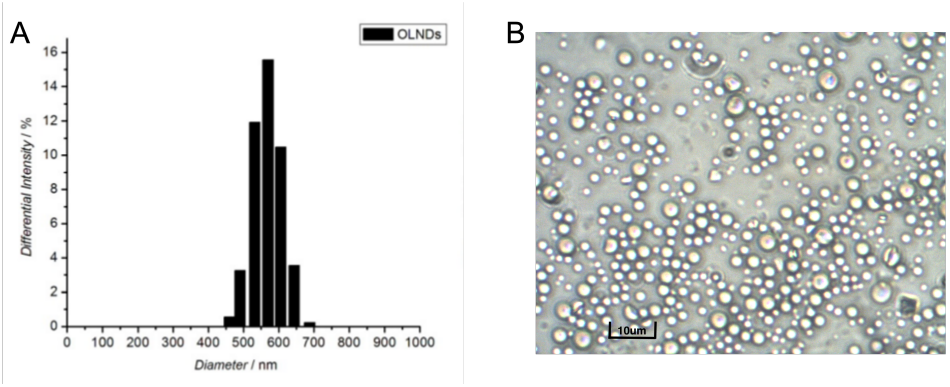

Fig. 3.3 A) Size distribution obtained by DLS investigation of chitosan-coated OLNDs and B) Optical microscope image of PVA-coated OLNDs with a magnification of 40 $\times$.

According to the DLS results, the average size of the PVA droplets was around $300 - 400$ nm, whereas the chitosan OLNDs exhibited larger dimensions, with an average diameter ranging from $500 - 600$ nm.
It has to be mentioned that commercial sono-sensitive Zinc Oxide nanoparticles (ZnO-NPs) were also used in this study to provide more data for acoustic response comparisons. These particles show a porous structure and, when dispersed in solution, interact with the US field to act as cavitation nuclei, leading to the formation of bubbles starting from the gas present in the solution. A TEM picture of ZnO NPs can be seen in Figure 3.4A together with their size distribution obtained by DLS analysis (Figure 3.4B). In order to perform the measurements on this sample, an aqueous solution 0.02 % of ZnO NPs was prepared homogenizing with a 20 kHz US probe at 20% of the maximum power for 2 cycles of 30 s.

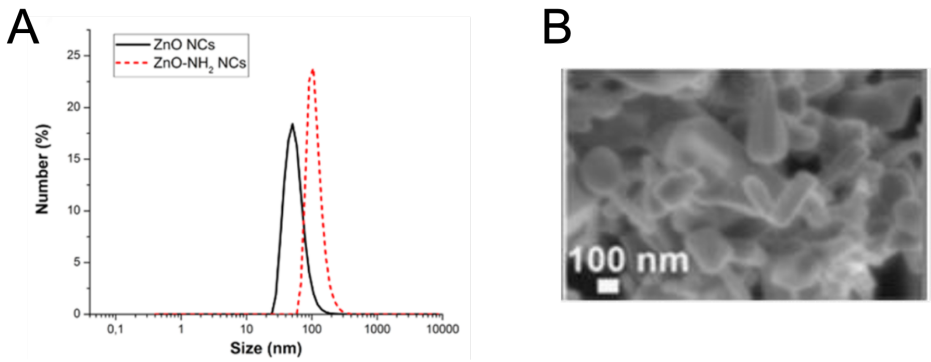

Fig. 3.4 A) DLS size distribution (black line) and B) TEM image of ZnO NPs [9].

3.2.2 Phantom Preparation

To perform the acoustic sample response analysis, the carrier solution was led to flow into a channel within a custom-made cylindrical phantom made of materials capable to simulate human soft tissue in its acoustic properties. Two different recipes were tested with the same phantom geometry and dimensions, as illustrated in Figure 3.5, but with diverse physical properties. To construct the channel, a small plastic tube with a diameter of approximately 3.5 mm was inserted in two holes dug on the opposite sides of the external surface of a plastic mould. For the first phantom, a transparent silicon-based polymer (Bluesil RTV 141A/B) was utilized. The components of the polymer were mixed together, and the resulting solution was poured into the mold. The mold, containing the solution, was then placed in an oven set at a temperature of 38 °C for a duration of 24 hours. This process facilitated the vulcanization of the polymer, leading to its solidification and formation of the first phantom.

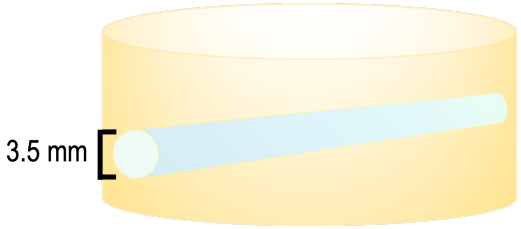

Fig. 3.5 Customized cylindrical phantom with the channel inside.

The second phantom employed a soft gel made from Gellan Gum (GG) polysaccharide. In summary, a 1.5% weight solution of GG was heated to 70 °C until the solution became clear. The solution was then poured into the plastic mold and left to cool. Subsequently, the cooled gel was immersed in a 0.4 Molar solution of zinc acetate. This step was performed to facilitate the crosslinking process initiated by divalent ions, enhancing the mechanical and attenuation properties of the gel. Additional details regarding the preparation methods and the acoustic properties of these phantoms can be found in reference [187].

3.2.3 Experimental Setup

A customized setup was developed to excite the carriers monitor their acoustic response. The setup, depicted in Figure 3.6, comprised a Sonic Concepts H-101 transducer for providing the acoustic excitation with a fundamental frequency of 1 MHz, fixed at the base of a ultra poor water-filled tank. The transducer was driven

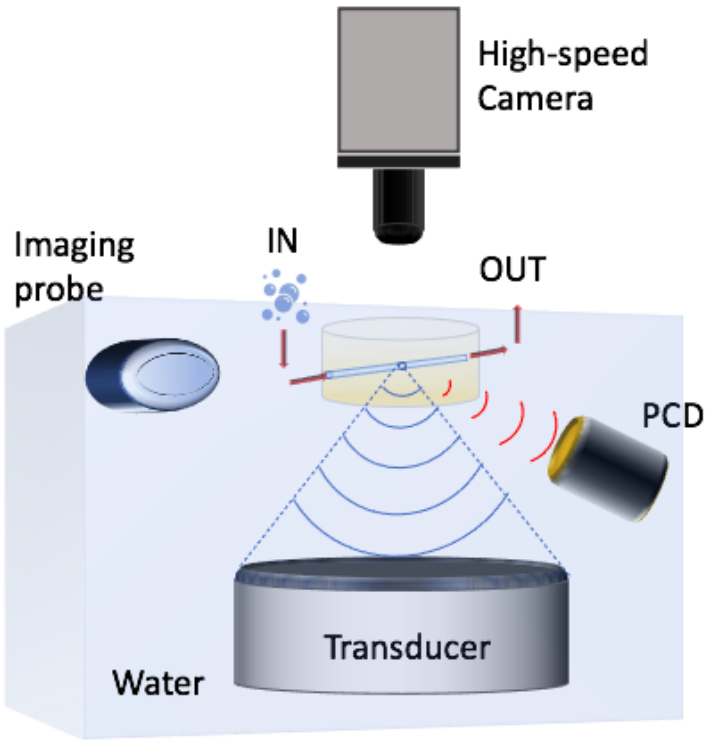

Fig. 3.6 Scheme of the experimental setup employed for the carriers characterization.

by A&R amplifier (model 800A3A) connected to a function generator (Agilent 33250A). Initially, the Peak Rarefractional Pressures (PRPs) were measured and stored on a Labview-provided PC, using a hydrophone coupled to an oscilloscope (InfiniiVision 2000 X DSO-X 2022A, Agilent Technologies).The range of working acoustic pressure for the reported experiments resulted $0.2 - 0.8$ MPa. A manual flow controller (Cole Parmer Masterflex Peristaltic Pump) was employed to inject the carrier suspension into the channel and, during the excitation, three different sensors were used to monitor the acoustic cavitation:

- a Passive Cavitation Detector (PCD) for acquiring the acoustic signal;
- an ultrasonic imaging probe record the ecographic response;
- a high-speed camera to capture the optical signal.

Cavitation Activity Detection

A focused PCD (Ultrasonic Transducer PA1101, Precision Acoustics) utilized to acquire the broadband acoustic signal generated by the forced bubble oscillations. Specifically, the PCD was connected to a spectrum analyzer (Keysight N9320b, Agilent) for signal acquisition in the range of 500 kHz -5 MHz. The obtained spectra were processed by performing a Fast Fourier Transform (FFT), and through LabView each recorded spectrum resulted from the average of five sequential measurements. FFT spectra were characterized by the presence of peaks at specific frequencies, generated by the forced bubbles oscillations and thus revealing the activity of stable cavitation within the solution. Final data were then stored and plotted by Matlab in order to highlight the presence of ultra-harmonics and harmonics with respect to the fundamental driving frequency. Basing on the assumption that during inertial cavitation events the produced shock waves generate a contribution in the continuous components in the spectra between harmonics and ultra-harmonics ("white noise"), the spectra were precessed through Matlab in order to perform the cavitation noise spectrum analysis, obtaining a quantitative indicator of the bubble collapse. This analysis was performed evaluating the cavitation noise power (CNP) indicator [188] as follows. Data were manipulated by means of Matlab to pass from linear to

logarithmic scale through the relationship:

$$I_{dB} = 20\log_{10}\left(\frac{I_{mV}}{I_0}\right) \tag{3.9}$$

in which I_0 represents the minimum value recorded by the analyzer for each spectrum. All the harmonics and ultra-harmonics components of the spectra were then filtered in order to emphasize only the contribution of the white noise and, at the end, the resulting data were integrated over frequency according to

$$CNP = \int I_{dB}(f)df \approx \sum I_{dB}(f)\delta f \tag{3.10}$$

where $I_{dB}(f)$ is the spectrum amplitude in logarithmic scale and f the frequency. Although the obtained values were not directly associated with physical power, they were indicative of the white noise power resulting from the activity of bubble collapse events. Consequently, these values served as a measure of the level of inertial cavitation activity.

Ultrasound Imaging

The ultrasonic imaging investigation was performed using an ultrasonic research scanner (Ultrasonix SonixTouch) connected to a linear probe (SA4-/24, Ultrasonix) operating at 10 MHz. The linear probe was placed in front of the phantom, parallel to the channel. Initially, B-mode imaging was used to align the channel inside the phantom to the US transducer focus to ensure that the carriers received the excitation correctly. Real-time responses of the solutions were the collected during ultrasound excitation, and the obtained videos were post-processed using Matlab in order to evaluate the average intensity of the bright spots recorded within a specific region of interest (ROI) within the channel during the excitation. This method enabled the extrapolation of a qualitative measure of the bubbles growth and oscillation, which could be correlated with the previously explained PCD analysis. During these first two approaches, deionized water response was also investigate to establish a reference and confirm the absence of cavitation activity.

Optical Imaging

The last sensor utilized in this setup was a high-speed camera (CamRecords 5000, Optronis), directed above the channel to provide an optical characterization of the cavitation phenomena. To optimize the recording, localizing the light directly onto the channel, a light source was placed on the top of the phantom and tilted appropriately to focus the light on the analysis area. However, due to setup limitations, the maximum recording rate achieved was of 3000 fps, although the camera's capabilities were up to 10000 fps. No single carrier dynamics could be appreciated with this limited condition, but it resulted sufficient for observing the group dynamic interaction of the bubbles with the acoustic field and to determine the different behavior demonstrated each type of sono-carriers.

3.2.4 Improvement of the Optical Setup

This paragraph describes a new setup that was implemented to overcome the limitations in recording speed of the previous optical section. An inverted optical microscope was modified as shown in Figure 3.7 so that the illumination was provided from the bottom and the top side of the setup was freed for implementing the US excitation. A high-intensity LED light source (MultiLED G8 power supply and MultiLED QT white, GS Vitec) was directed towards a beam splitter placed directly below the objective lens of the microscope to address light beam towards the sample. The reflected part of the beam coming from the sample was sent, by means of the same beam splitter, towards the high-speed camera placed, to this aim, at the output of the microscope. The focused transducer was reversed respect to the previous setup, in order to give the US excitation from the top, pointing its focus directly onto the channel of the phantom. In order to allow the acoustic field propagation between the transducer and the flowing suspension, a hollow plastic cone filled with ultra-pure water was attached to the transducer and placed with the tip facing the channel phantom. Thanks to the more intense the light source implemented, this setup was able to reach recording speed up to 10000 fps with a better frame resolution and visibility. Furthermore, the original microscope allowed to change magnification during measurements thanks to the possibility to install objective lenses, thus adding another degree of freedom in the recording properties. Three different objective lenses were exploited, with a magnification respectively of 20 $\times$, 40 $\times$ and 60 $\times$.

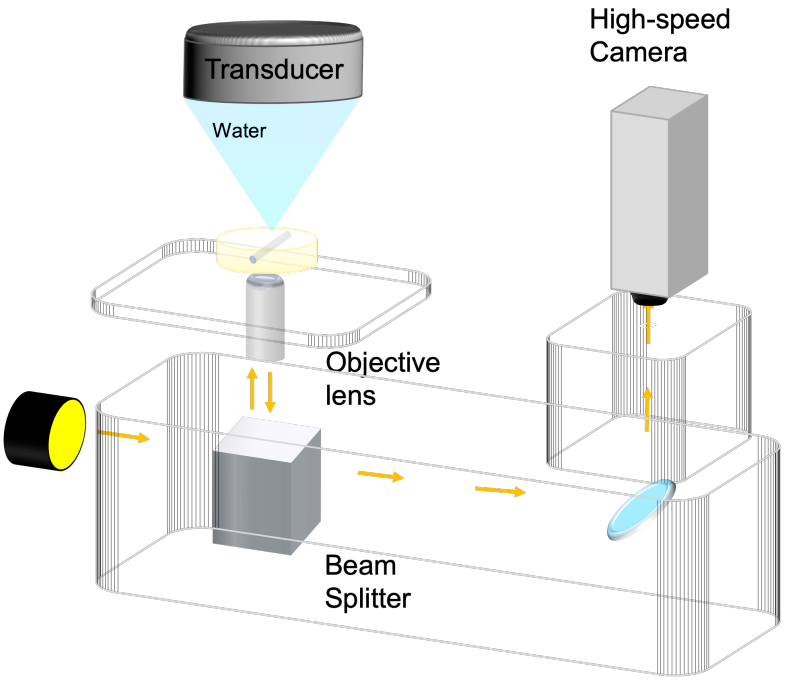

Fig. 3.7 Scheme of the setup implemented in order to improve the high-speed camera recording parameters.

Through the frames recorded with this improved setting, some single bubbles statistics could be performed for each sample by analyzing twenty videos for each sample at a single pressure through ImageJ software. The dependence of bubbles lifetime and streaming velocity on the applied acoustic pressure were in this way evaluated. The PRPs were measured also for this new setup using the same instrumentation described in Section 3.2.3.

3.3 OLNDs Functionalization with Magnetic NPs

The second part of the study concerned the magnetic functionalization of OLNDs using Fe_3O_4 NPs in order to perform MDV. This section describes the materials and the methodologies employed for aiming this scope. First, the optimal method for MOLNDs preparation was established, followed by the physico-chemical characterization of the obtained samples, and then, the assessment of this functionalization was performed. The samples were at this point characterized in their acoustic response, in order to understand if the presence of the NPs on their structure led to significant

changes in their behavior. Finally, MDV was tested and, as last measurement, a comparison of the oxygen released by means of acoustic and magnetic stimuli was performed.

3.3.1 MOLNDs preparation

The functionalization of OLNDs was achieved by using Fe_3O_4 nanoparticles, previously synthesized by means the co-precipitation method [10]. To briefly explain, a mixture of iron(II) chloride tetrahydrate and iron(III) chloride hexahydrate with a molar ratio 1:2 (Fe^{2+}/Fe^{3+}), was dispersed in deionized water and heated up to 75 °C. Ammonium hydroxide (30 %) was then added dropwise to promote precipitation until pH reached the value of 8. The reaction was carried out for 1 h at 85 °C and the resulting precipitate was finally washed with deionized water and magnetically decanted. In Appendix A the main properties of the Fe_3O_4 NPs employed in this work are reported, focusing in particular on their physicochemical (Figure A.1) and magnetic characteristics (Figure A.2).
In order to prepare a formulation of MOLNDs, 5 *mg* of Fe_3O_4 NPs were homogenized in 1 mL of a saturated aqueous solution prepared with PVP and Epikuron 200 (at an equal concentration as OLNDs preparation) with a 20 kHz US probe at 20 % of the maximum power for 2 cycles of 10 s. The resulting solution was added to 4 mL of OLNDs suspension (prepared as explained in section 3.2.1) to reach a final concentration of Fe_3O_4 NPs equal to 1 mg/mL. The mixture was then homogenized for two more steps of 10 s in an ice-water bath to ensure binding to the OLNDs surface. This procedure was repeated for all the OLNDs samples. The final MOLNDs structure is illustrated in Figure 3.8.
In this section, new OLNDs formulations were prepared using DFP as before and PFP as PFC cores, while chitosan, PVA, and dextran as polymeric coatings. Chitosan and PVA solution were prepared as already explained in Section 3.2.1, and for dextran, the polymeric solution was prepared starting from commercial dextran (Sigma-Aldrich) with a concentration of 2.7% in deionized water. PFP has a boiling point of 29 °C, which means that PFP-based OLNDs and MOLNDs are expected to vaporize and cavitate at a lower excitation energy with compared to DFP-based ones.

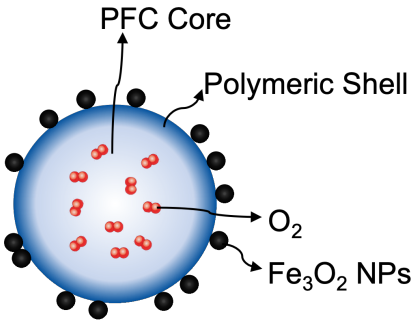

Fig. 3.8 Schematic representation of the magnetic oxygen-loaded nanodroplets (MOLNDs).

3.3.2 Physicochemical Characterization

The initial analysis conducted for this study focused on the hydrodynamic size distribution and ζ potential of both OLNDs and MOLNDs. These properties were determined at room temperature through the use of DLS using the Malvern - Zetasizer Lab.
Then, the morphological characterization of the nanodroplets was performed by Scanning Electron Microscopy (SEM) using the FEI Inspect – F. instrument and by Transmission Electron Microscopy (TEM). The SEM analysis provided an initial assessment of the functionalization of Fe_3O_4 NPs, though the liquid state of the formulations presented some challenges. To address this, each sample was dried on a silicon support prior to SEM analysis to ensure better sample control and to prevent droplet removal during testing, which could compromise the accuracy of the results. TEM images were acquired through a Philips CM 10 transmission electron microscope (Eindhoven, The Netherlands), with an electronic beam energy of 80 kV. A drop of the suspension was allowed to adsorb for 5 min on a Pelco® carbon and formvar-coated grid and then washed several times with water. 0.5 % w/v uranyl acetate in water was used to negatively stain the grid and excess fluid was removed with filter paper.

3.3.3 Acoustic Characterization

Both OLNDs and MOLNDs were characterized in terms of their acoustic behavior to determine the influence of Fe_3O_4 nanoparticles on their response. The setup shown in Figure 3.7 was used, with the US excitation source placed at the top of the

phantom and pointed directly at the channel in which the carriers were flowing. The utilized PCD sensor was characterized by a focus distant 7 *c*m from its surface, and given that the phantom radius was approximately 2 cm, it was inserted in another ring-shaped phantom of the same material with a thickness of about 5 cm. This was done to ensure a total distance of approximately 7 cm between the channel center and PCD. The sensor was positioned adjacent and in contact to this external phantom to accurately collect the acoustic signal. In contrast to the setup used in subsection 3.2.3, where the measurements were performed in water, ultrasound gel was spread on the contact surface between the sensor and the phantom in this case to ensure the transmission of the acoustic field. Prior to measuring OLNDs and MOLNDs samples, PRP values were measured and stored, resulting in a working range of $0.08 - 1.74$ MPa. The solution was then injected into the channel using a flow controller (uniPERISTALTICPUMP 1, LLG LABWARE), and the broadband acoustic signal was acquired in the range of $0.5 - 5$ MHz. Each spectrum was obtained by averaging three acquisitions, and stable and inertial cavitation events were analyzed for all the samples, as discussed in Section 3.2.3.

3.3.4 Functionalization Assessment

To confirm the functionalization with Fe_3O_4 NPs, an analysis on MOLNDs streaming trajectory was conducted under the influence of a magnetic field gradient generated by a nearby permanent magnet. In particular, two different setups were employed to this aim, as displayed in Figure 3.9.

Two different methods were employed to analyze the behavior MOLNDs The first method (see Figure 3.9A) involved the use of an ultrasonic research scanner (Ultrasonix SonixTouch) connected to a linear probe (SA4-/21, Ultrasonix) in the presence or absence of a NdFeB magnet with dimensions 12×6 mm.

A transducer (Sonic Concept SU 103) operating at a frequency of 3.3 MHz was focused on the center of a parallelepipedal sample holder containing the suspension. The sample was exposed to ultrasound, and the behavior of MOLNDs was recorded after turning off the excitation. The captured frames were post-processed using the tracking plug-in of ImageJ software [189], and Matlab was used to extrapolate the droplets streaming velocity. Each average value was obtained based on 30 measurements.

Figure 3.9B illustrates the second setup, which involved a microfluidic pump (Flow

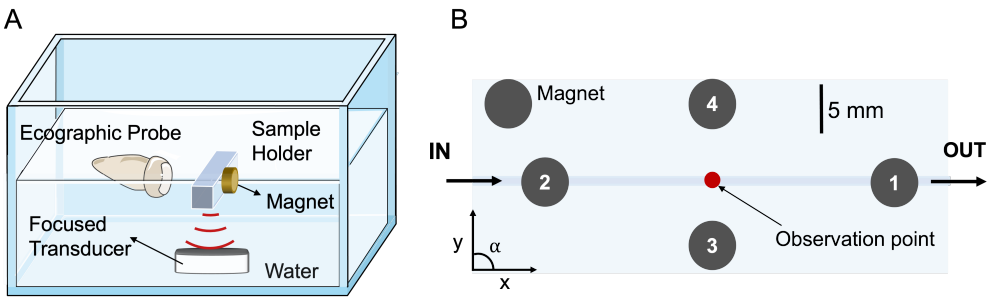

Fig. 3.9 Schematic representation of A) the setup used to record the droplet behavior by means of ecographic imaging probe and B) of the microfluidic chip employed to evaluate the steering angle and the velocity variation due to the magnet influence .

EZ, Fluigent) to generate a constant flow of the sample into a single micro-channel chip (Be-Flow, BEOnChip) and an optical microscope (IX73, Olympus) connected to an external camera to record the transit of MOLNDs. Both the steering angle and the streaming velocity of the droplets were evaluated in five different conditions for each sample, including the absence of the magnet and placing it (a NdFeB magnet with dimensions 5×2 mm) in four different positions in relation to the sample flow. The tracking plug-in of ImageJ software was employed to analyze the measurements. Table 3.2 displays the characterization of the residual magnetization B evaluated at different distances, resulted the same for both magnets employed in the two different setups.

Table 3.2 Residual magnetization (B) of the NdFeB magnet as function of the distance.

Distance (mm)	0	2	6
Remanence (kG)	2.56	0.56	0.126

3.3.5 Magnetic Droplet Vaporization

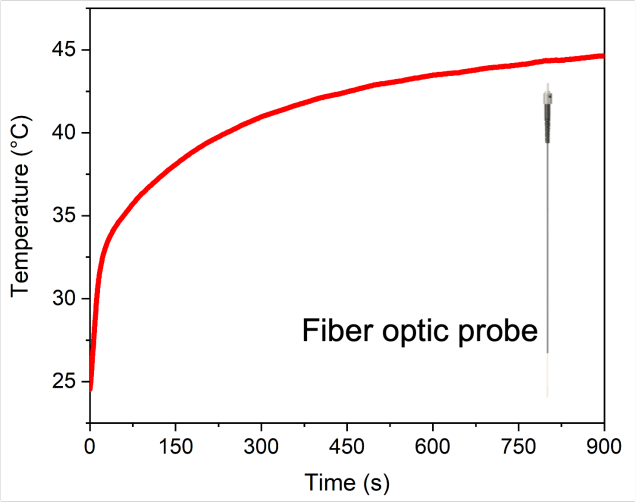

Fig. 3.10 Typical temperature trend over time measured by the fiber optic probe during the excitation of MOLNDs through an uniform AC magnetic field.

The experiment to induce magnetic droplet vaporization in MOLNDs involved a custom-built setup (see Figure 3.11B) that generated a uniform alternating current (AC) magnetic field with a frequency of 100 kHz and an amplitude selectable up to 72 kA m^{-1}. A volume of 1 mL of the suspension was placed in a tube on a thermally isolated support to prevent heat losses. The sample was exposed to the magnetic field, and the temperature was monitored using a fiber optic thermometer (Osensa Innovation). The experiment was performed at specific temperatures based on the boiling points of PFCs - 25 °C, 27 °C, 29 °C, 37 °C for PFP-core MOLNDs and 37 °C, 45 °C, 48 °C, 51 °C in case of DFP based ones. After exposure to the magnetic field, the sample was immediately observed under an optical microscope (ARISTOMET, Leitz) to check for the presence of vaporized bubbles, which confirmed the occurrence of MDV. Figure 3.10 displays a typical increase in temperature over time recorded by the fiber optic probe during the uniform AC magnetic field excitation of the MOLNDs suspension.

3.3.6 Oxygen Release

As final measurement, the evaluation of the oxygen release induced by both acoustic and magnetic stimuli was compared. In the first case, OLNDs oxygen release was

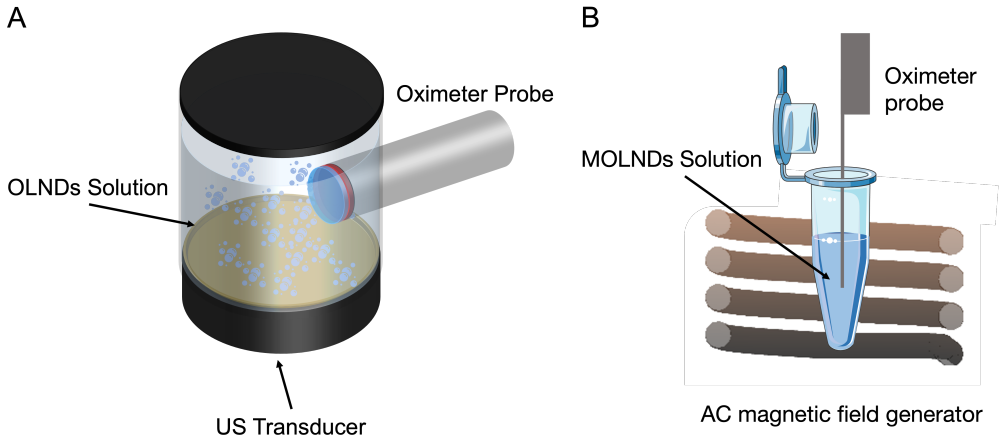

Fig. 3.11 A) Illustration of the setup used to conduct oxygen release experiments on OLNDs samples during US exposure. B) Visual depiction of the experimental system to evaluate oxygen discharge induced by the alternating magnetic field stimulus.

measured by a digital oximeter (Hach.) HACH HQ 40D connected with a LDO 101 digital, luminescent/optical dissolved oxygen (LDO) probe. A small bath was hermetically closed putting an US transducer, characterized by a working frequency $f_0 = 1$ MHz, at the base and the probe laterally inserted into the bath as shown in Figure 3.11A. 5 mL of OLNDs suspension was dipped into the bath collecting the oxygen level to be used as reference. Before measuring the oxygen levels, the hydrophone described in Section 3.2.3 was utilized to measure the PRP, which was found to be 0.13 MPa. The sample was then exposed to US excitation for 270 s and the oxygen concentration value was measured and stored every 30 s.
Similarly, the oxygen release induced by MDV in MOLNDs was evaluated using the same oximeter as in the OLNDs experiments, integrated into the customized setup described in Section 3.3.5 and shown in Figure 3.11B. The oxygen concentration of each sample was measured before and after the MDV process, with the sample holder kept hermetically sealed. The magnetic field was turned off once the temperatures previously mentioned were reached (from 25 °C to 37 °C for PFP-core and from 37 °C to 51 °C for DFP-core). The oxygen concentration value was collected for 270 s in this case as well.

Chapter 4

Results and Discussion

This chapter provides a detailed description of the results obtained in this project. In the first part of this chapter, a comprehensive description of the outcomes obtained to characterize acoustic, ecographic and optical signals emitted by sonosensitive carriers - OLNDs and ZnO NPs - during cavitation phenomena through two customized setups is presented.
In the second section, an optimized method for the preparation of magnetic OLNDs is presented. After a characterization of the physico-chemical properties of MOLNDs, their magnetic functionalization is demonstrated, and, finally, a comparison is drawn between the oxygen release capability resulting from the exploitation of an alternating magnetic field and standard US-based stimuli methods.

4.1 Multiple Approaches for Ultrasonic Cavitation Monitoring

The first part of the thesis aims to detail the results obtained by a comprehensive characterization of the response of chitosan- and PVA- coated OLNDs and ZnO NPs to ultrasound excitation. The experimental setups described in Sections 3.2.3 and 3.2.4 were utilized to analyze the acoustic behavior of the solution with the carriers as it flowed into the channel within the customized phantom and to capture the acoustic, ecographic and optical signal emitted.

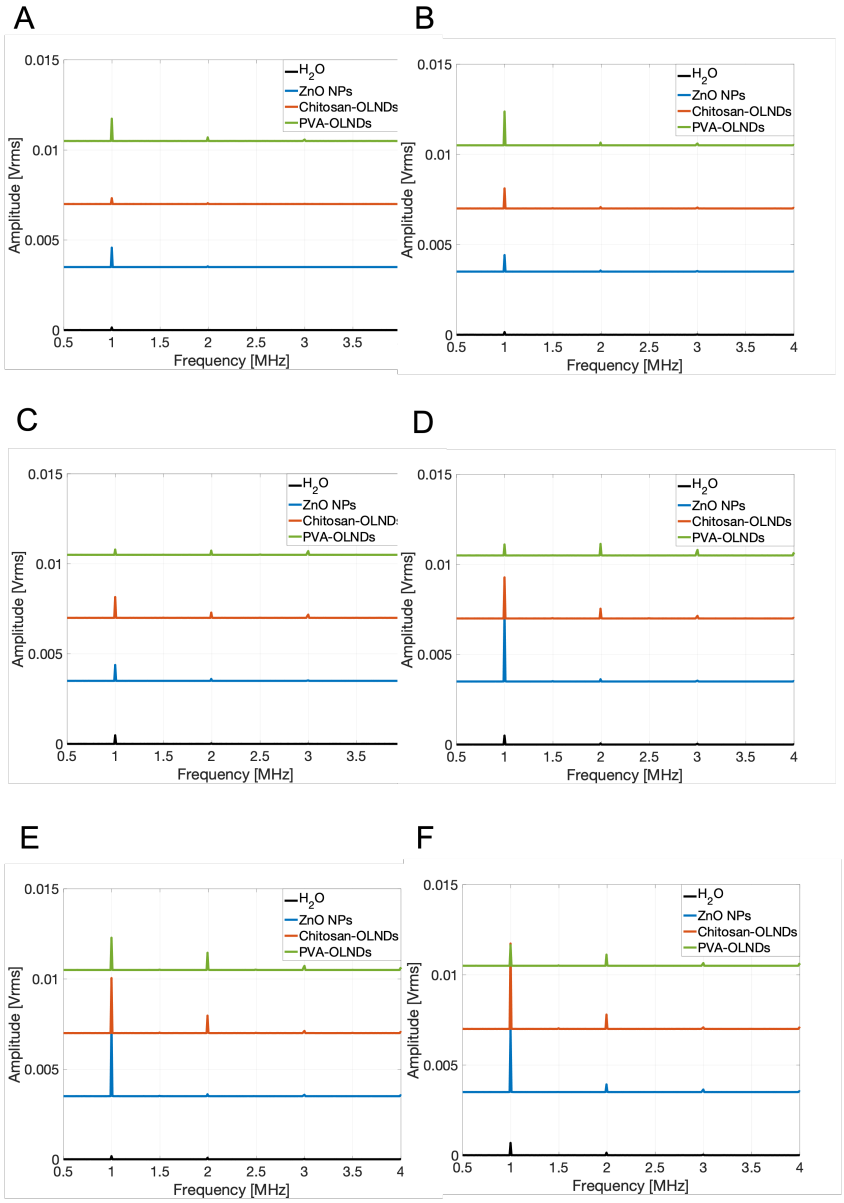

Fig. 4.1 FFT spectra of chitosan-, PVA- coated OLNDs and ZnO NPs compared with respect to pure water (black line) at different acoustic pressures: A) 0.29 MPa, B) 0.36 MPa, C)0.40 MPa, D) 0.53 MPa, E) 0.74 MPa, F) 0.79 MPa.

4.1.1 First Setup

Through the setup described in Figure 3.6 of Section 3.2.3, three signals have been monitored during the interaction between US excitation and carriers flowing into the channel of the customized phantom. The PCD is used for having information about the cavitation activity, both stable and inertial, occurring into the channel, the ecographic probe to perform acoustic imaging and the high-speed camera for recording real-time images of carriers inside the channel.

Cavitation Activity Detection

The PCD sensor was used to collect FFT spectra for each sample at different acoustic pressures, as shown in the plots of Figure 4.1. Each graph in the figure displays four acoustic spectra, one for each sample, generated at a given acoustic pressure, with three of them (ZnO NPs and OLNDs ones) being slightly shifted in the y-direction for better visibility and comparison respect to pure water (black spectrum).
The spectra results indicate the presence of a primary peak at the working frequency of the US transducer ($f_0 = 1.1$ MHz) in all samples. Pure water only exhibits the fundamental peak characterized by a limited amplitude compared to the other samples, which show additional peaks at specific frequencies with higher amplitude, confirming that the presence of sonosensitive carriers in the solution enhances the response to US. In particular, the spectra related to the carriers are distinguished by multiple discrete frequency components located around $n \cdot f_0/m$, where m and n represent integer values. These frequency components, known as harmonics and ultra-harmonics, arise due to the non-linear characteristic of stable cavitation, which induces forced oscillations through the interaction between vaporized bubbles and the ultrasonic field.
Furthermore, different behaviors are observed depending on the carrier when increasing the acoustic pressure. When using PVA-based OLNDs and ZnO NPs, a detectable main peak is observed even at low acoustic pressure ($P_a = 0.29$ MPa), indicating that a small amount of bubbles oscillating at the driven frequency $f_0 = 1.1$ MHz are already present. Conversely, at that acoustic pressure Chitosan-coated OLNDs show an amplitude of the fundamental peak similar to that of water, suggesting the absence of cavitation events and thus a shifted threshold for entering the stable cavitation regime towards higher pressures ($P_a = 0.36$ MPa). This behavior may be

attributed to the more rigid structure provided by chitosan to the nanodroplets shell compared to PVA and also to the bubbles coming from ZnO NPs that are not coated by a polymeric shell. As the acoustic pressure rises, the amplitude of the main peak significantly increases for all samples and ultra-harmonics related to the presence of non-linear oscillations appear for the OLNDs samples, indicating a significant intensification of the oscillating phenomena regardless of the carrier used, while NPs show a sharp intensification of the amplitude of the fundamental peak only.
After analyzing the filtered broadband spectra, CNP parameter was evaluated for all samples at the same acoustic pressures proposed in the FFT spectra analysis. Figure 4.2 presents the numerical results of the CNP parameter of the four solutions as a function of increasing acoustic pressure. The CNP of pure water (represented by black bars) remains unchanged, independent of the induced pressure, indicating the absence of inertial cavitation events in the solution. In contrast, sonocarriers exhibit a significant increase in the parameter as the acoustic pressure rises to higher values. Specifically, PVA-coated OLNDs begin experiencing the inertial cavitation regime at $P_a = 0.53$ MPa, ZnO NPs at $P_a = 0.74$ MPa, and chitosan-shelled droplets at $P_a = 0.79$ MPa, confirming the same order of activation observed for stable cavitation. The more rigid shell structure of chitosan-OLNDs allows them to remain in the stable regime for a wider range of acoustic pressures.
The analysis of the FFT spectra enables the determination of the upper pressure limits required to prevent the activation of inertial cavitation phenomena for the different carrier exploited, thereby avoiding any undesirable side effects induced by violent bubble collapse.

Ultrasound Imaging

Some frames of the videos captured using the ultrasonic imaging probe are depicted in Figure 4.3. For each sample, two different acoustic pressures are presented - 0.39 MPa and 0.79 MPa -, and four consecutive frames are selected for each pressure, covering the time span of $t = 0$ s to $t = 3$ s. The channel, which has a width of approximately $d_{channel} = 2.5$ mm, contains the solution with the sample and, bubbles forming and oscillating under the the acoustic field excitation are easily visible. This allows for a qualitative assessment of the cavitation activity occurring within the channel.
In the case of water, there is no significant difference in the formation of bubbles

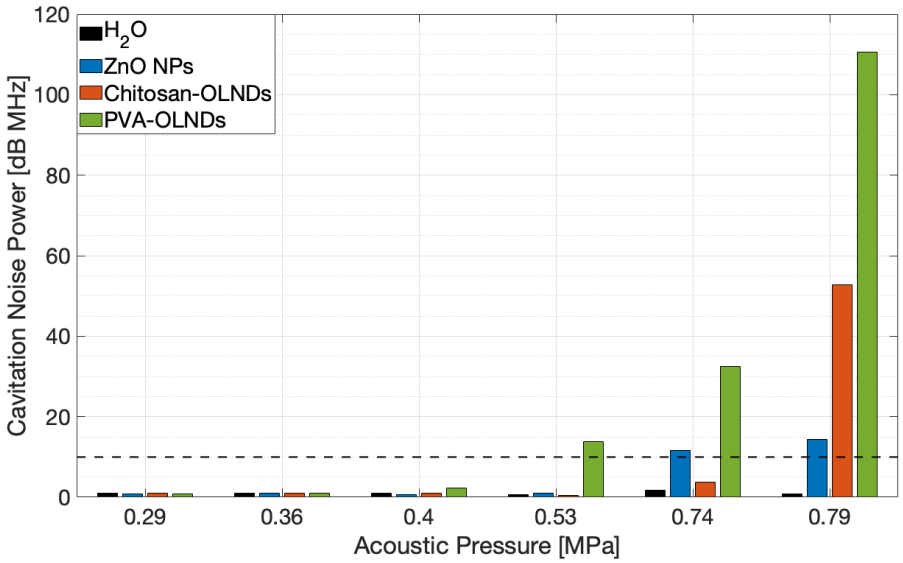

Fig. 4.2 Comparison of the cavitation noise power (CNP) among pure water, ZnO NPs, chito-coated OLNDs, and PVA-coated OLNDs at varying acoustic pressures. The black dashed line in the graph represents a qualitative threshold for determining the occurrence of the inertial cavitation regime.

in the channel between the low and high acoustic pressure, indicating the absence of cavitation activity even at higher pressures and confirming the results obtained through PCD analysis. However, for the three carrier cases, only a few bubbles are visible inside the channel at $P_a = 0.39$ MPa as excitation time progresses, while a large number of vaporized droplets can be appreciated after just 1 second of US irradiation at $P_a = 0.79$ MPa.

In order to get quantitative information from the frames captured by ecographic imaging, the average intensity during US irradiation within a ROI selected inside the channel is evaluated. The ROI is represented by a yellow box in the frames of Figure 4.3 and is defined to consider the US field focus point. The measurement is taken for 4.5 s after the starting of the US excitation, and the mean values for each sample at the each acoustic pressure are reported in Figure 4.4.

The results of the measurement show that pure water samples do not exhibit a significant increase in light spot intensity as the acoustic pressure increases because no bubbles are formed inside the channel. Furthermore, each result related to a sample with carriers is in agreement with the ones observed quantitatively from PCD method for stable cavitation measurement. In particular, PVA-OLNDs demonstrate a strong amount of bubbles oscillating at $P_a = 0.29$ MPa, being the intensity level significantly

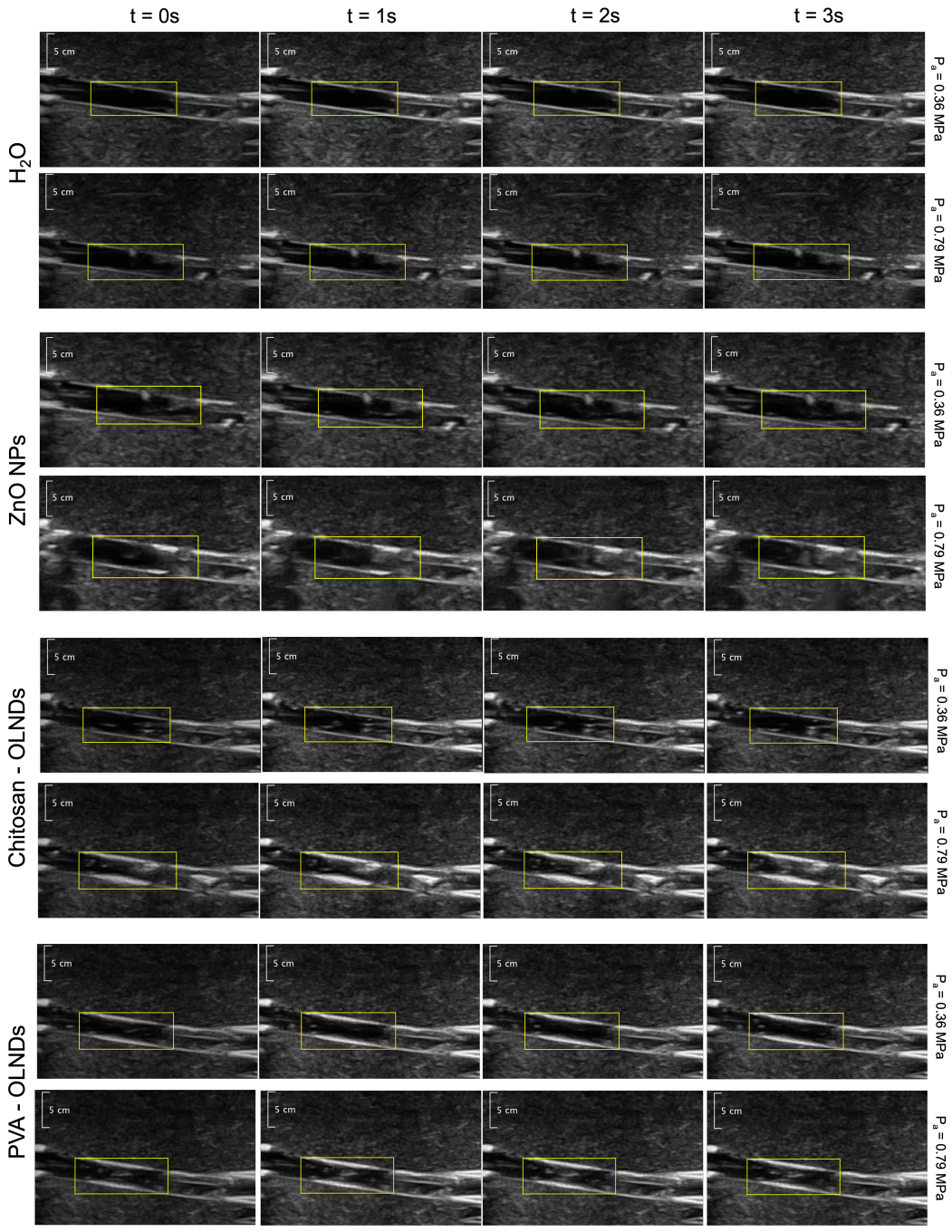

Fig. 4.3 Four consecutive frames of the videos recorded by the US ecographic probe at two different acoustic pressures for pure water, ZnO NPs, chitosan- and PVA-coated OLNDs.

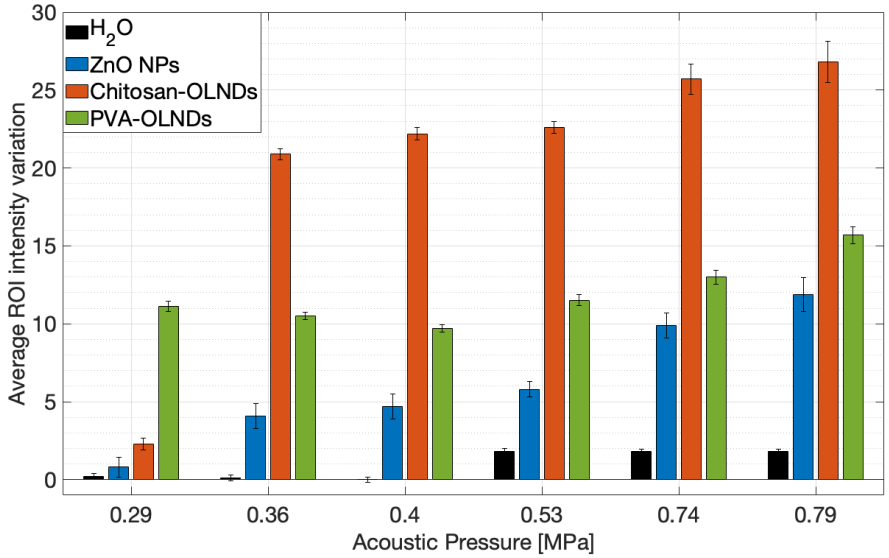

Fig. 4.4 Comparison of the intensity averaged on 4.5 s of the light spots measured into the ROI (yellow box in Figure4.3) for each solution at different acoustic pressures.

high, then is kept nearly constant up to $P_a = 0.53$ MPa, and finally, it starts to rise slightly. Chitosan-coated carriers, on the other hand, enter the bubble formation and stable cavitation regime at a more intense pressure condition ($P_a = 0.36$ MPa), showing s light intensity value close to zero at $P_a = 0.29$ MPa. ZnO NPs have a more linear increase of the average intensity with the rise of the pressure, reaching a significant level only as the pressure reaches a value equal to $P_a = 0.53$ MPa, but with a overall lower intensity respect to the OLNDs.

The observed difference in intensity levels between chitosan-coated droplets and PVA-OLNDs and ZnO NPs suggests that chitosan more rigid shell structure results in a lower population undergoing the inertial cavitation mechanism, leading to the formation of more trapped bubbles in the acoustic antinodes and a more intense signal on the imaging probe. In contrast, PVA-based samples and ZnO NPs disappear suddenly once the bubble transition is completed. This behavior is further confirmed by the presence of more intense light spots observed in the recorded frames of PVA-OLNDs and ZnO NPs, which are usually associated to the presence of air in the solution, indicating that the inertial cavitation activity starts at lower pressures for these two samples.

Figure 4.5 illustrates the trend of instant light intensity in the ROI for the four samples over time at two limit acoustic pressures. As anticipated, at $P_a = 0.39$ MPa,

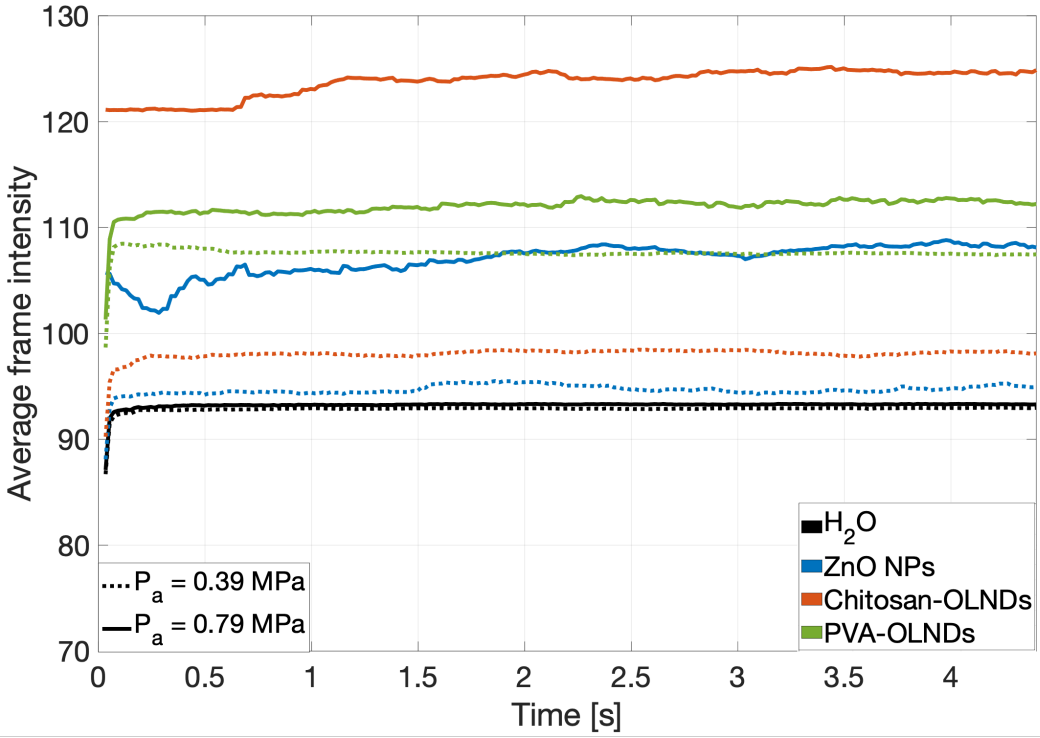

Fig. 4.5 Comparison of the instantaneous intensity of the light spots measured into the ROI (yellow box in Figure 4.3) for each solution at $P_a = 0.39$ MPa (dashed lines) and $P_a = 0.79$ MPa (continuous lines).

each sample has a lower intensity level than at $P_a = 0.79$ MPa, except for pure water, which shows exactly the same values for both cases since no bubbles are forming. Additionally, for lower pressure cases, the intensity trends are flatter, with no significant variations over time, whereas for the higher pressure ones, trends exhibit a slightly increasing evolution over time with visible instantaneous fluctuations of the value. This behavior indicates that cavitation overall activity intensifies over time, but instantaneously new bubbles form and start oscillating while others collapse and disappear. This observation is confirmed also by the uncertainty bars reported in Figure 4.4, which indicate that as pressure increases, uncertainties also become slightly higher.

Optical Imaging

Figures 4.6, 4.7, and 4.8 show high-speed frames of ZnO NPs, chitosan-coated OLNDs, and PVA-coated OLNDs, respectively, flowing inside the channel under an acoustic pressure of $P_a = 0.74$ MPa. The recording time for the videos started after 5 seconds of US exposure to better appreciate the droplet dynamics. The videos reveal the oscillation of bubbles, and upon closer examination, it is observed that the response velocity of the bubbles depends on their size, with larger bubbles exhibiting slower responses to the acoustic field. Additionally, observing the group dynamics of the carriers, different behavior is demonstrated analyzing each sample. In particular, in the case of the ZnO NPs, a smaller population of bubbles characterized by larger dimensions can be noted. In fact, these larger bubbles derive from the merging of smaller ones previously present in the solution. The lack of a shell to enforce stability may make bubbles generated from ZnO NPs more prone to merge as they approach each other in a multibubble-system, undergoing the coalescence process before collapsing, as described in Section 2.1.6.

Conversely, OLNDs tend to agglomerate towards fixed positions along the acoustic field lines, at which they start increasing their dimensions. Before achieving the final collapse, single bubbles undergo rectified diffusion while oscillating growing up to their resonance sizes. At this point, adjacent bubbles merge due to coalescence mechanism, resulting in larger final bubbles. Specifically, chitosan-coated bubbles agglomerate in long lines, while PVA-coated ones form bigger clusters around which oscillate.

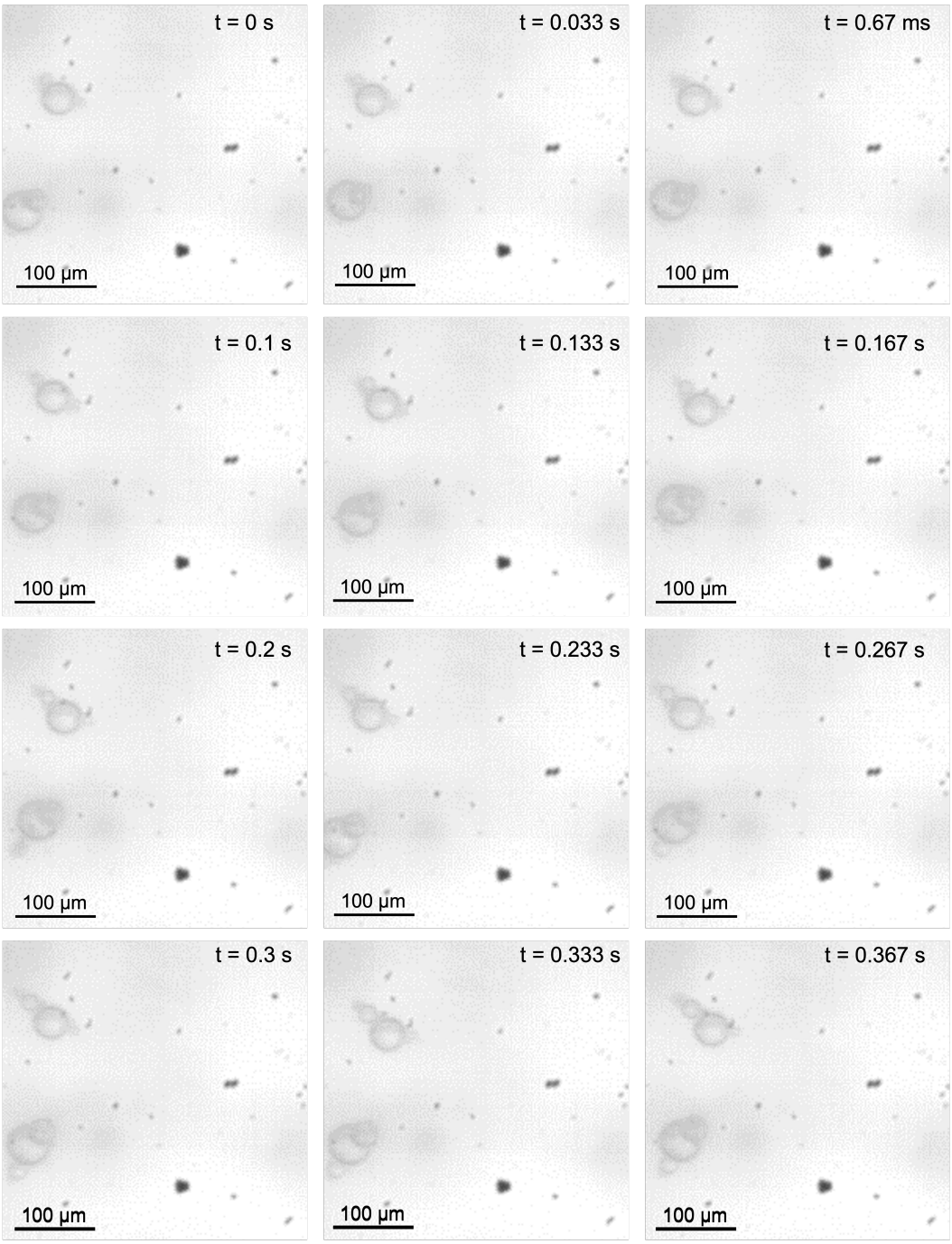

Fig. 4.6 Frames recorded with the high-speed camera with a frame rate of 3000 fps at different time of ZnO NPs at acoustic pressure $P_a = 0.74$ MPa.

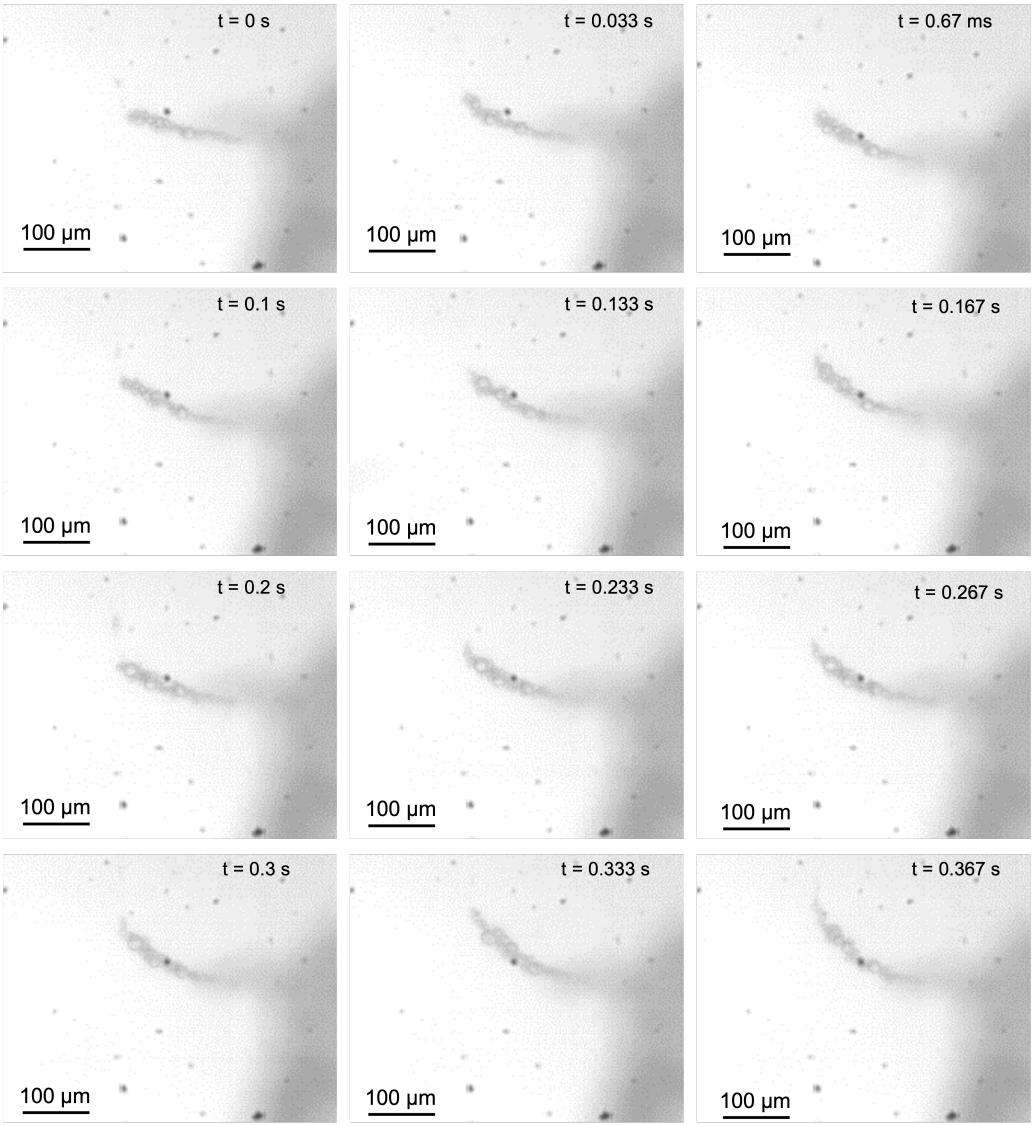

Fig. 4.7 Frames recorded with the high-speed camera with a frame rate of 3000 fps at different time of chitosan-coated OLNDs at acoustic pressure $P_a = 0.74$ MPa.

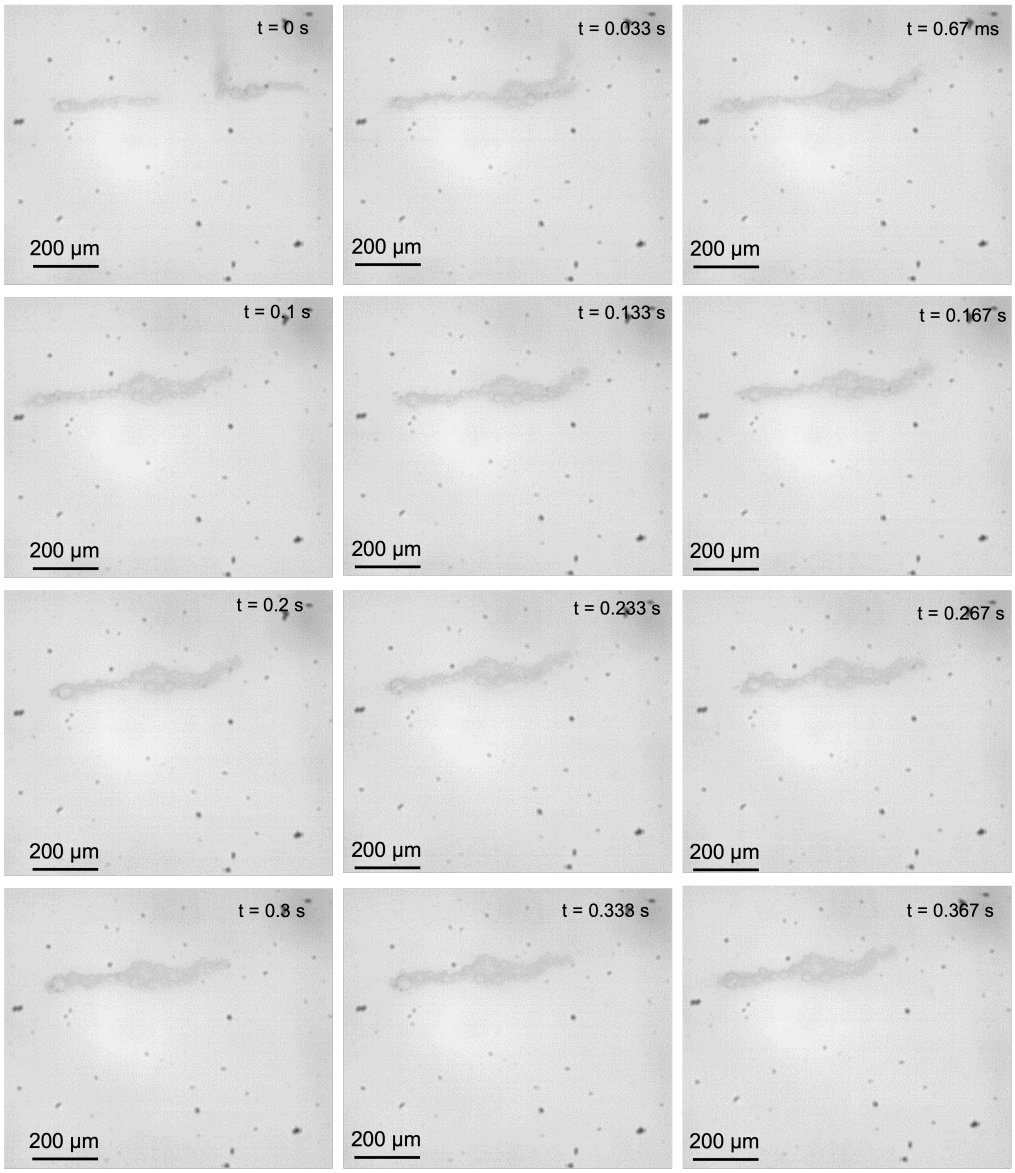

Fig. 4.8 Frames recorded with the high-speed camera with a frame rate of 3000 fps at different time of pva-coated OLNDs at acoustic pressure $P_a = 0.74$ MPa.

4.1.2 Improvement of the Optical Setup

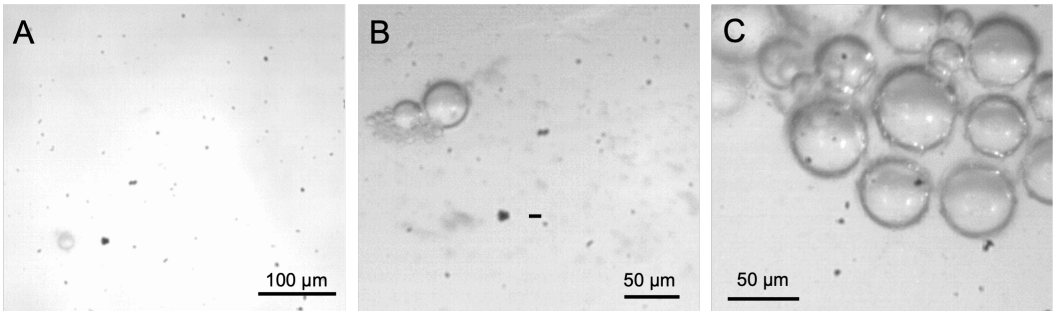

Fig. 4.9 High-speed camera frames of A) ZnO NPs with a 20× objective lens, B) PVA-coated OLNDs with a 40× objective lens and C) chitosan-coated OLNDs with a 60× objective lens.

The optical imaging results described above only provide qualitative information about the behavior of the groups of bubbles already formed in the solution. This limitation is primarily due to the maximum frame rate of the setup conditions (3000 fps), but also to the fixed objective of the camera that limits the image magnification. To improve this analysis thus, a second setup has been proposed (Figure 3.7), able to achieve recording speeds up to 10000 fps and to exploit three different objectives. Figure 4.9 shows a picture obtained from each objective, thus with a different magnification. Upon initial observation of the recorded videos, it become apparent that the measurement can provide diverse information depending on the plane on which the lens focus inside the channel, as bubbles can be observed in different conditions. Specifically, when the lens are focused on the center of the channel, the motion of bubbles interacting with the acoustic field becomes more apparent. Four sequential frames for each carrier are shown in Figure 4.10, depicting the trajectory of bubbles under an acoustic pressure of $P_a = 0.67$ MPa recorded at a speed of 5000 fps and with a magnification of 40 $\times$. From the frame sequences it can be noticed how bubbles tend to stream towards clusters placed on the acoustic field lines at which they start oscillating. From this analysis statistical information about the bubbles streaming velocity can be extrapolated at different acoustic pressures ranging from 0.37 MPa to 0.78 MPa. Results are plotted in Figure 4.11.
As expected, the streaming velocity is found to be strictly dependent on the acoustic pressure used, increasing as the pressure rises, regardless of the type of carrier being analyzed. As already qualitatively observed in the optical imaging discussion of Section 4.1, their responsiveness is also affected by the dimensions and mass of the bubbles. ZnO NPs generate lighter bubbles compared to OLNDs, which have

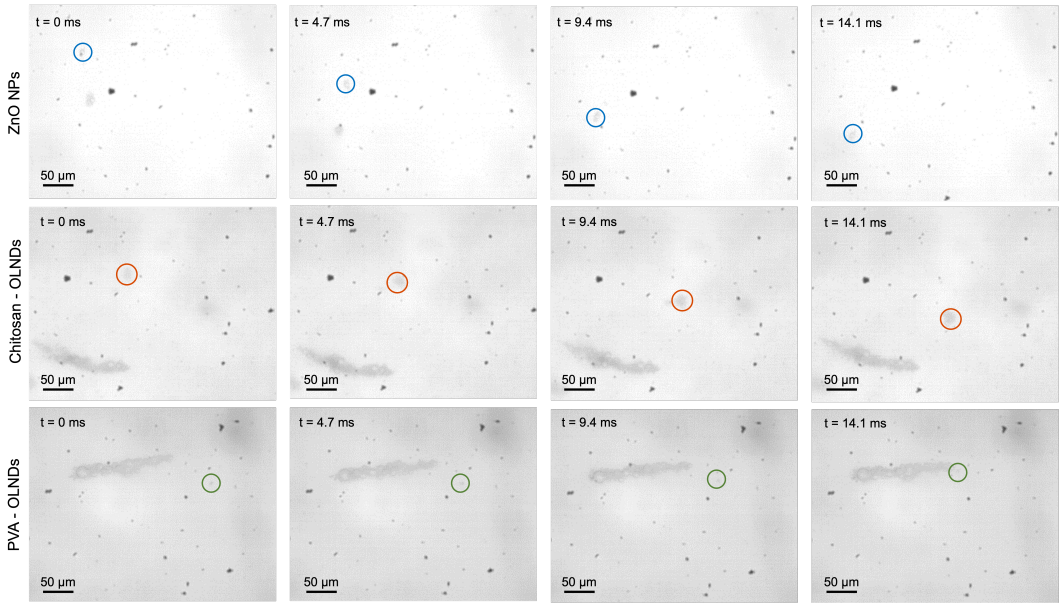

Fig. 4.10 Frames captured by the high-speed camera with a 40 × objective lens at a recording speed of 5000 fps of the samples. Circles in the frames highlight the trajectory traveled by a single bubbles under US field.

a more complex structure consisting of different components. Therefore, OLNDs show an overall slightly lower streaming velocity compared to ZnO NPs, regardless of the working pressure. Furthermore, when comparing samples with different shells, chitosan-coated OLNDs have higher velocities, especially for low acoustic pressures. This is probably because, under the same conditions, they tend to maintain smaller dimensions due to their more rigid shell, which is less prone to expand compared to PVA-shelled bubbles. The uncertainties associated with the results plotted in Figure 4.11 demonstrate a high variance of the measured velocities, confirming the dependence of bubble response to ultrasound on their size. As shown in the size distribution in Figure 3.3, OLNDs dimensions can vary by more than 100 nm from their mean value. This significant heterogeneity, resulting from the homogenization method used for droplet synthesis, generates a similar level of variance in the bubbles generated from droplets.

Moving the focus of the objective lens deeper towards the surface of the channel, fixed carriers can be observed, providing the opportunity to appreciate their formation, growth and final collapse. In Figure 4.12, four frames for each sample extrapolated from videos recorded at a frame rate of 10000 fps during US excitation are shown. For each case, it can be noticed the complete life cycle of a single bubble, starting

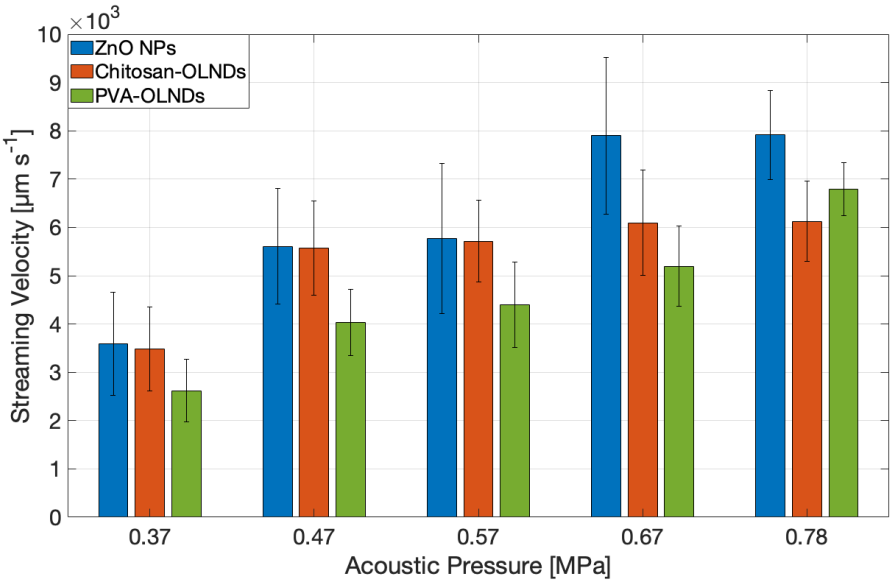

Fig. 4.11 Average streaming velocities evaluated for each carrier from the videos recorded by the high-speed camera at different acoustic pressures.

from $t = 0$ s when no bubbles are present in the circles, passing from the two intermediate times (second and third frames) at which one single bubble is present inside the same circles, up to its collapse (fourth frame), at which bubbles are no longer visible. Similar to the streaming velocity analysis, a statistical evaluation of the carriers average lifetime at different acoustic pressures is performed in this case as well. The results of this analysis are shown in Figure 4.13, in which the average lifetime of the carriers is plotted. From the obtained results, it can be inferred that the bubble's lifetime is also highly dependent on the acoustic pressure, but unlike the streaming velocity, it exhibits an inverse proportional relationship. As the acoustic pressure increases, the bubble's lifetime decreases. Specifically, the lifetime is approximately halved when the pressure is increased from 0.37 MPa to 0.78 MPa. These findings provide valuable insights into the dynamics of acoustic cavitation and can inform the design and optimization of cavitation-based processes.

Building on these findings, further insights can be gained through the improved experimental setup. Figure 4.14 and Figure 4.15 showcase frames capturing the coalescence process of OLNDs at enhanced magnification (up to 60 $\times$) and frame rate (up to 10000 fps). In particular, Figure 4.14 illustrates a sequence of consecutive frames, recorded at 5000 fps and with 40 $\times$ objective lens, showing PVA-coated OLNDs approaching and merging, resulting in two distinct coalescence events. The

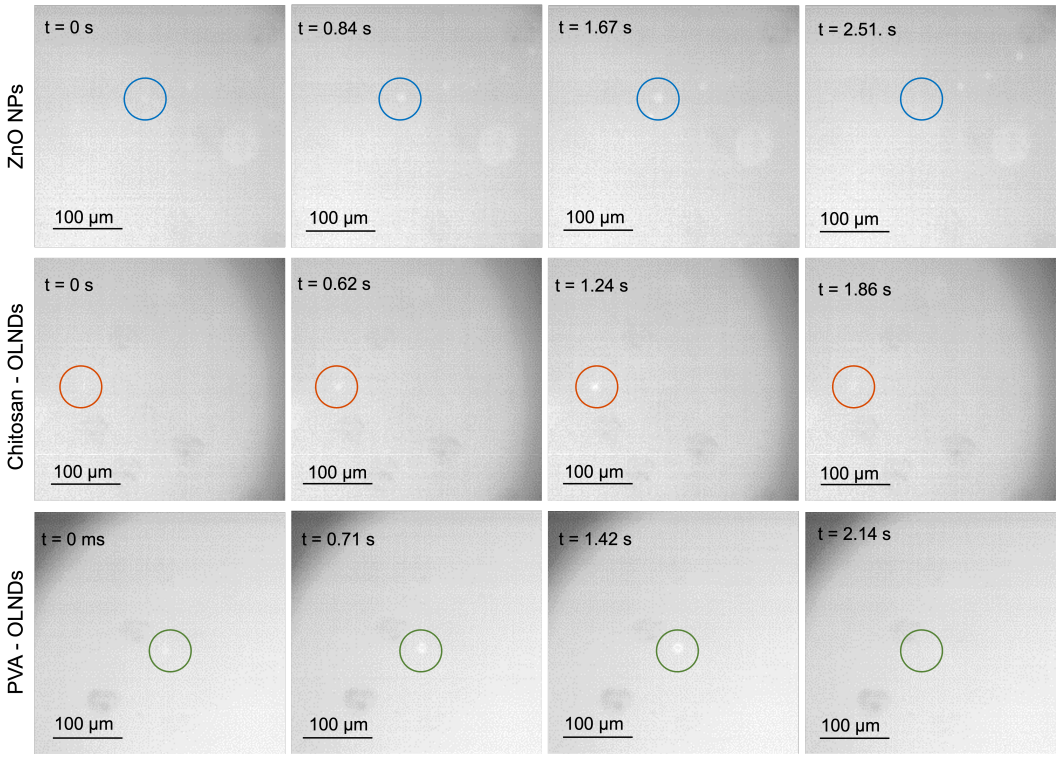

Fig. 4.12 Frames captured by the high-speed camera with a 20 × objective lens at a recording speed of 10000 fps of the samples under an acoustic pressure of 0.47 MPa. For each sample, the life cycle of a single bubble (highlighted by the colored circles) is shown starting from its formation in the first frame and ending with its disappearance in the fourth frame.

first coalescence event is observed at $t = 0.2$ ms, during which the largest bubble in the black circle seems to disappear, only to reappear with larger dimensions at $t = 0.6$ ms. The second coalescence event takes place shortly after, at $t = 1.2$ ms, where the newly formed bubble vanishes together with one of its nearest ones, and a larger bubble appears at $t = 1.6$ ms.

Figure 4.15 presents similar frames for chitosan-coated OLNDs with two distinct blocks of six consecutive frames each. In this case, recording speed was increased to 10000 fps and 60 × magnification was exploited. The first block shows two main bubbles that tend to get closer as time goes on, while the second block, that record exactly th same situation after 164.7 ms, captures their merging, that can be visible between times 165.4 s and 165.5 s.

However, it can be noticed that both the recording speeds exploited are not enough for capturing the clear steps of the process. In both cases, in fact, coalescence occurs

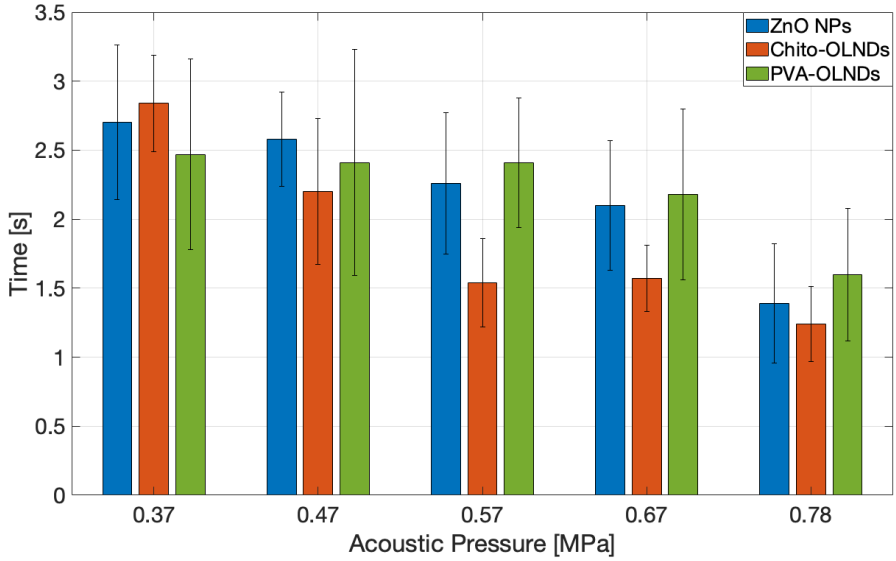

Fig. 4.13 Average lifetimes evaluated for each carrier from the videos recorded by the high-speed camera at different acoustic pressures.

between two consecutive frames, meaning that actually this kind of analysis requires further higher recording speeds to clearly investigate the phenomenon.

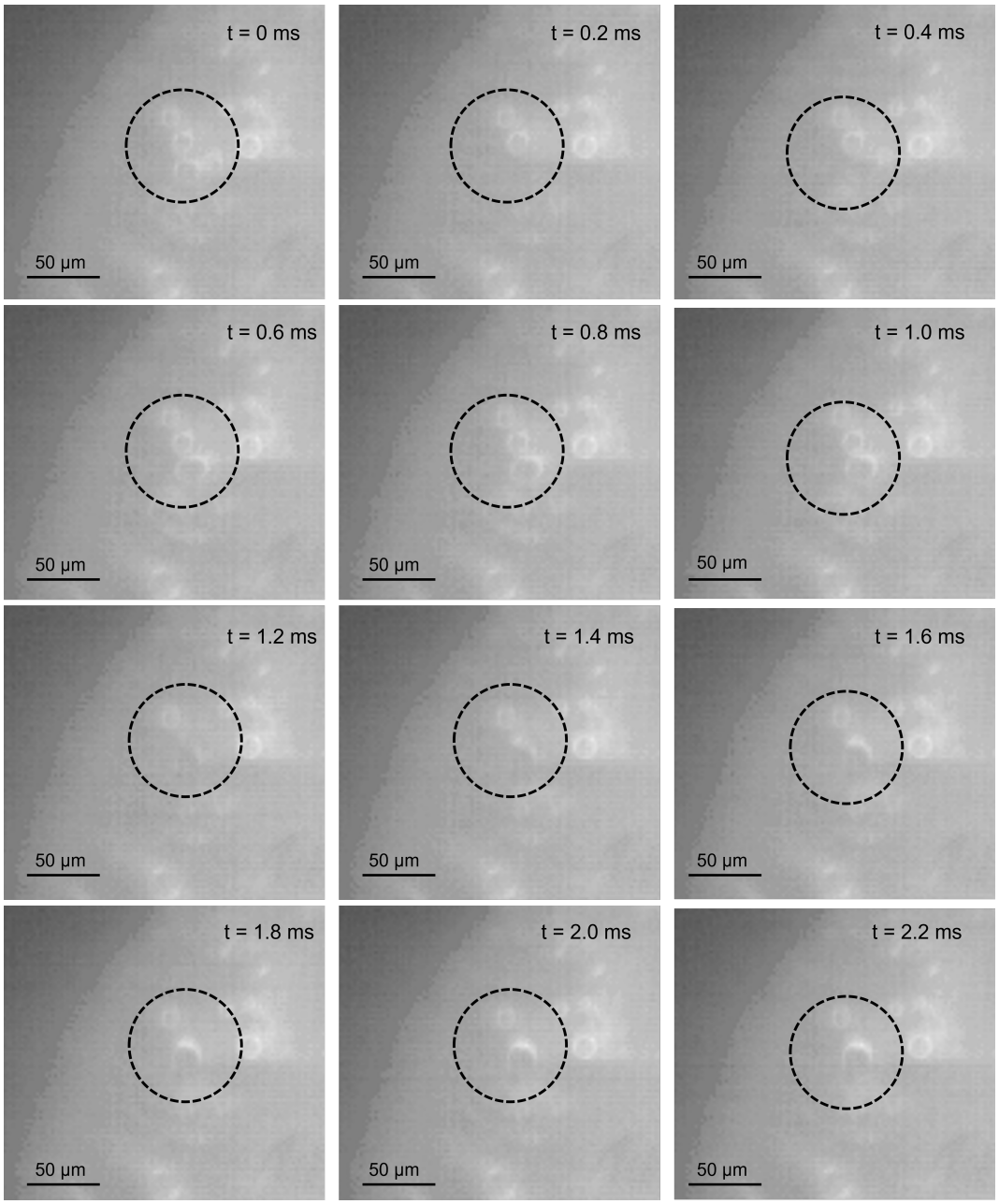

Fig. 4.14 Frames captured by the high-speed camera with a 40 × objective lens at a recording speed of 10000 fps of PVA-coated OLNDs under an acoustic pressure of 0.57 MPa. Attention is drawn to a group of adjacent bubbles that undergo the coalescence process, which is highlighted using black dashed circles.

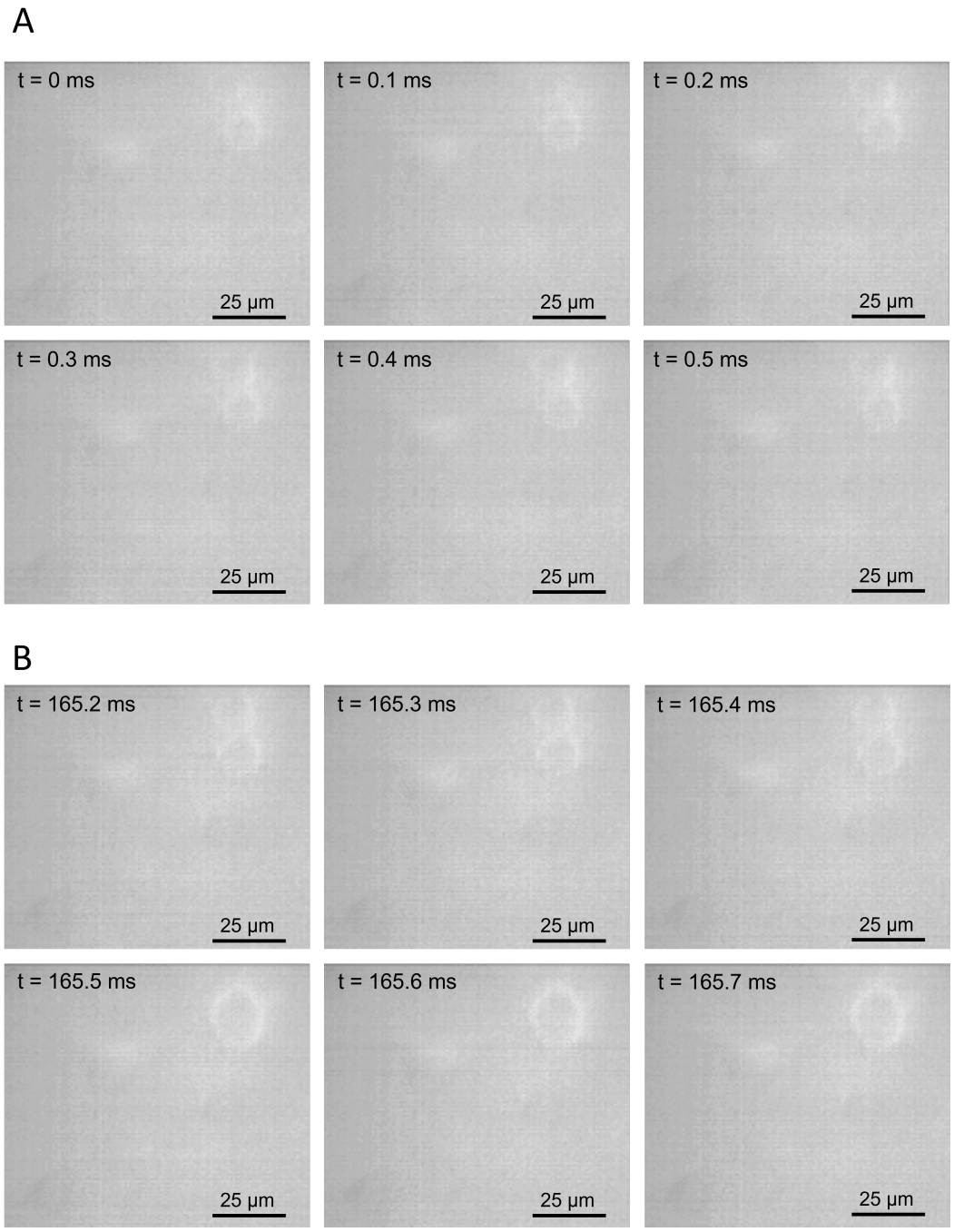

Fig. 4.15 Frames captured by the high-speed camera with a 60 × objective lens at a recording speed of 5000 fps of chitosan-shelled OLNDs under an acoustic pressure of 0.47 MPa. A) Consecutive frames showing the approaching of two close bubbles; B) consecutive frames of the same bubbles after ≈ 164.7 ms undergoing the coalescence process.

4.2 OLNDs Functionalization with Magnetic NPs

The focus of this second section is the investigation of magnetically functionalized nanodroplets (MOLNDs) using Fe_3O_4 nanoparticles. Firstly, the dimensions, shape, and ζ potential of the MOLNDs are examined to understand the changes in physicochemical properties induced by the presence of nanoparticles. Subsequently, the samples' response to the acoustic field is analyzed to obtain information about both stable and inertial cavitation activities, and the influence that NPs can have on these activities. Following these initial characterization steps, the magnetic functionalization is verified through various approaches. Finally, the oxygen release induced by MDV is evaluated and compared with that induced by the acoustic field, providing evidence that the observed increase in oxygen concentration is due to MDV phenomena. Before this evaluation, vaporization induced by an alternating magnetic field is also assessed to confirm the source of the oxygen increment measured in the solution.

4.2.1 Physico-chemical Characterization

Six different samples of OLNDs were synthesized through the homogenization method, utilizing two perfluorocarbons - DFP and PFP - as the core, and three different polymers - chitosan, dextran, and PVA - as the shell. Subsequently, Fe_3O_4 NPs with an average diameter of approximately 10 nm were used to magnetically functionalize the surface of each sample, obtaining thus six MOLNDs samples. Appendix A contains supplementary information regarding the Fe_3O_4 NPs and their properties.

The initial step in the analysis of magnetic nanodroplets (MOLNDs) was their physico-chemical characterization using SEM and TEM microscopy. Representative SEM images of OLNDs and MOLNDs are shown in Figure 4.16A and 4.16B, respectively, where the cases of DFP-core nanodroplets coated with chitosan are depicted. The OLNDs image shows quasi-circular halos with a diameter of a few hundred nanometers, indicating the presence of liquid droplets on the silicon support that have evaporated before the microscopy procedure. In contrast, the MOLNDs image shows a cluster of Fe_3O_4 NPs in close proximity to these droplet halos, indicating functionalization of the surface. The size of the MOLNDs sample is around 350 nm.

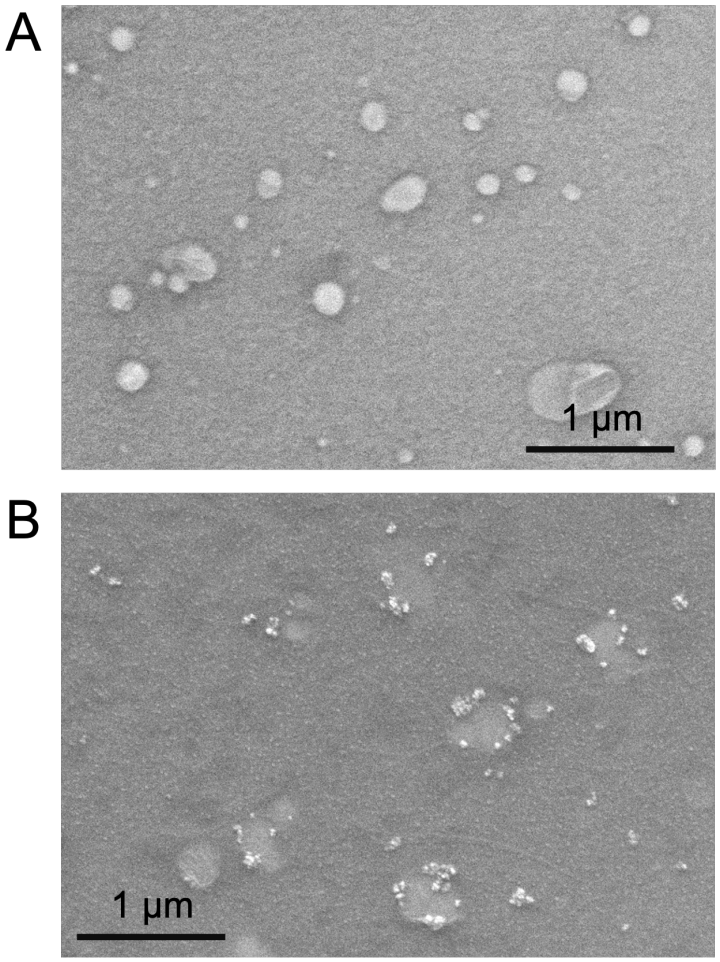

Fig. 4.16 SEM images of A) chitosan-coated OLNDs and B) MOLNDs.

Figure 4.17 shows two TEM pictures of DFP-based MOLNDs coated with chitosan. The presence of Fe_3O_4 NPs on the nanodroplet surface can be distinctly appreciated, validating the results gathered through the SEM imaging and corroborating the effectiveness of the droplets magnetic functionalization. The hydrodynamic size distributions of the samples were analyzed using DLS, and the results are presented in Figure 4.18. Mean values of the size distributions are reported in Table 4.1. The findings confirm that the PFC structure does not have a significant impact on the size of OLNDs [91]. In fact, there is no substantial difference between the DFP and PFP cases. On the other hand, the choice of coating agent plays a crucial role in determining the droplet size, as evidenced by the larger diameter of chitosan-coated droplets compared to both dextran- and PVA-coated ones. Furthermore, functionalizing the droplet surface with Fe_3O_4 NPs results in an increase in their mean size,

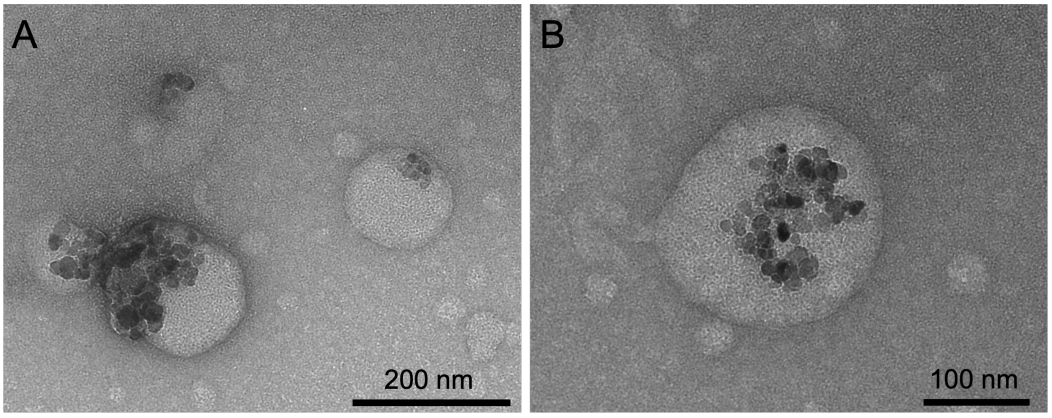

Fig. 4.17 TEM images of A) a group of DFP-based, chitosan-coated MOLNDs and B) a single zoomed MOLND.

regardless of the core and coating used. The plotted distribution reveals the presence of elements quite outside the expected droplet size range, with some values around and below 100 nm and others above 1000 nm. The former can be attributed to the presence of residuals of the synthesis reagents in the solution, and also of free Fe_3O_4 NPs in the case of MOLNDs. The higher values, on the other hand, are due to droplet agglomeration and vaporized bubbles, especially in the PFP case, which has a lower vaporization threshold. Therefore, only values ranging from 100 nm to 900 nm were taken into account for the evaluation of the mean diameters presented in Table 4.1.

Table 4.1 displays the ζ potential values for each sample. The results demonstrate that the type of coating agent has an impact on this value, with dextran- and PVA-coated droplets exhibiting a negative ζ potential, and chitosan-coated droplets providing a positive one. Moreover, surface functionalization with NPs has an impact on the ζ potential value of the samples, with a decrease in its absolute value observed for MOLNDs compared to their respective OLNDs. This decrease indicates that the suspension becomes less stable.

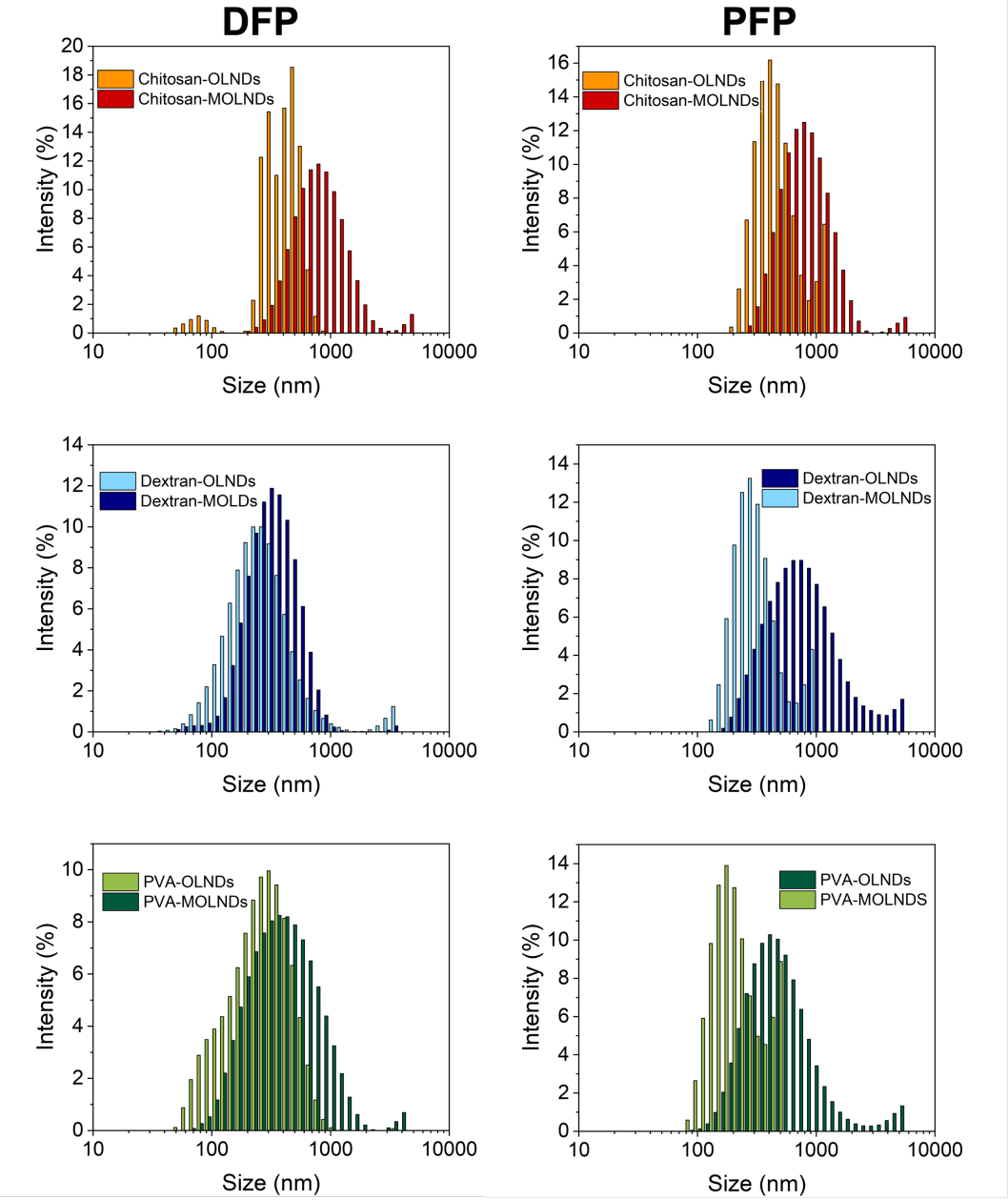

Fig. 4.18 Hydrodynamic diameter distribution obtained by DLS technique. In each graph OLNDs and correspondent MOLNDs are plotted together in order to appreciated the influence of Fe_3O_4 NPs on the distribution.

Table 4.1 Mean hydrodynamic diameter and ζ potential for OLNDs and MOLNDs samples measured by means of DLS.

Sample				**Diameter (nm)** $\pm \sigma$	**ζ Potential (mV)** $\pm \sigma$
F_3O_4 NPs				135 $\pm$ 35	-24.8 ± 0.5
	Core	**Coating**	**Magnetic**		
OLNDs	DFP	Chitosan	✗	419 $\pm$ 13	39.5 $\pm$ 2.5
			✓	627 $\pm$ 22	24.7 $\pm$ 1.4
		Dextran	✗	285 $\pm$ 16	-21.7 ± 3.9
			✓	345 $\pm$ 15	-18.4 ± 0.3
		PVA	✗	310 $\pm$ 16	-34.4 ± 1.3
			✓	408 $\pm$ 23	-12.3 ± 5.5
	PFP	Chitosan	✗	407 $\pm$ 11	21.7 $\pm$ 3.9
			✓	638 $\pm$ 21	18.4 $\pm$ 0.3
		Dextran	✗	292 $\pm$ 12	-50.9 ± 1.8
			✓	563 $\pm$ 25	-25.6 ± 0.6
		PVA	✗	236 $\pm$ 12	-61.0 ± 2.7
			✓	455 $\pm$ 22	-49.3 ± 2.3

4.2.2 Acoustic Response of MOLNDs

Figures 4.19 and 4.20 display the acoustic spectra emitted by the DFP- and PFP-samples, respectively, for both OLNDs and MOLNDs. As previously explained in Section 4.1.1, the spectra exhibit peaks that indicate stable cavitation activity resulting from forced bubble oscillations in the solution. For each sample, four spectra at increasing acoustic pressures ($0.08 - 0.57 - 1.04 - 1.74$ MPa) are presented. The trend of the peaks in each case appears to be quite similar, showing an increasing bubbles oscillating activity with the rise in pressure inside the solution, with no significant variations in droplet behavior attributed to the perfluorocarbon and the coating used. However, comparing OLNDs and relative MOLNDs spectra, the presence of Fe_3O_4 NPs induces an increase in peak amplitude at the same acoustic pressure, indicating a stronger emitted acoustic signal. This discrepancy is attributed to the NPs presence in the solution, which boosts acoustic field scattering events, resulting in a local increase in pressure and, as a result, in the amount of cavitation activity.

To quantify inertial cavitation activity, spectra were processed using cavitation noise

spectrum analysis, and the CNP parameter was evaluated.
Figures 4.21 and 4.22 depict the CNP indicator for all samples, in which the black dashed line gives a qualitative idea of threshold for which the inertial cavitation starts to be significant. The results show that as the acoustic pressure increases, the CNP rises after reaching a specific threshold, which varies depending on the sample. The pressure range before the threshold enables identification of optimal working conditions for preventing the inertial cavitation regime.
Moreover, the type of coating used affects the cavitation behavior, as the chitosan coating produces a more rigid structure than dextran and PVA, resulting in inertial cavitation triggering at higher acoustic pressures for both OLNDs and MOLNDs. Additionally, magnetic functionalization causes the threshold for the inertial cavitation regime to shift towards lower pressures due to the enhancement of acoustic wave scattering events, as already discussed for stable cavitation.
As in the FFT spectra analysis, similar results are obtained regardless of DFP- and PFP- core samples, but with more intense signals attributed to PFP lower boiling temperature, resulting in a higher percentage of cavitated droplets.
All these considerations are summarized in Table 4.2, in which the acoustic pressures at which inertial cavitation starts are shown for each sample.

Table 4.2 Acoustic pressures for entering the inertial cavitation regime.

Sample			**Acoustic**
Core	Coating	Fe_3O_4	**Pressure (MPa)**
DFP	Chitosan	✗	1.74
		✓	1.10
	Dextran	✗	1.42
		✓	0.78
	PVA	✗	1.54
		✓	1.04
PFP	Chitosan	✗	1.01
		✓	1.04
	Dextran	✗	0.78
		✓	0.67
	PVA	✗	0.92
		✓	0.67

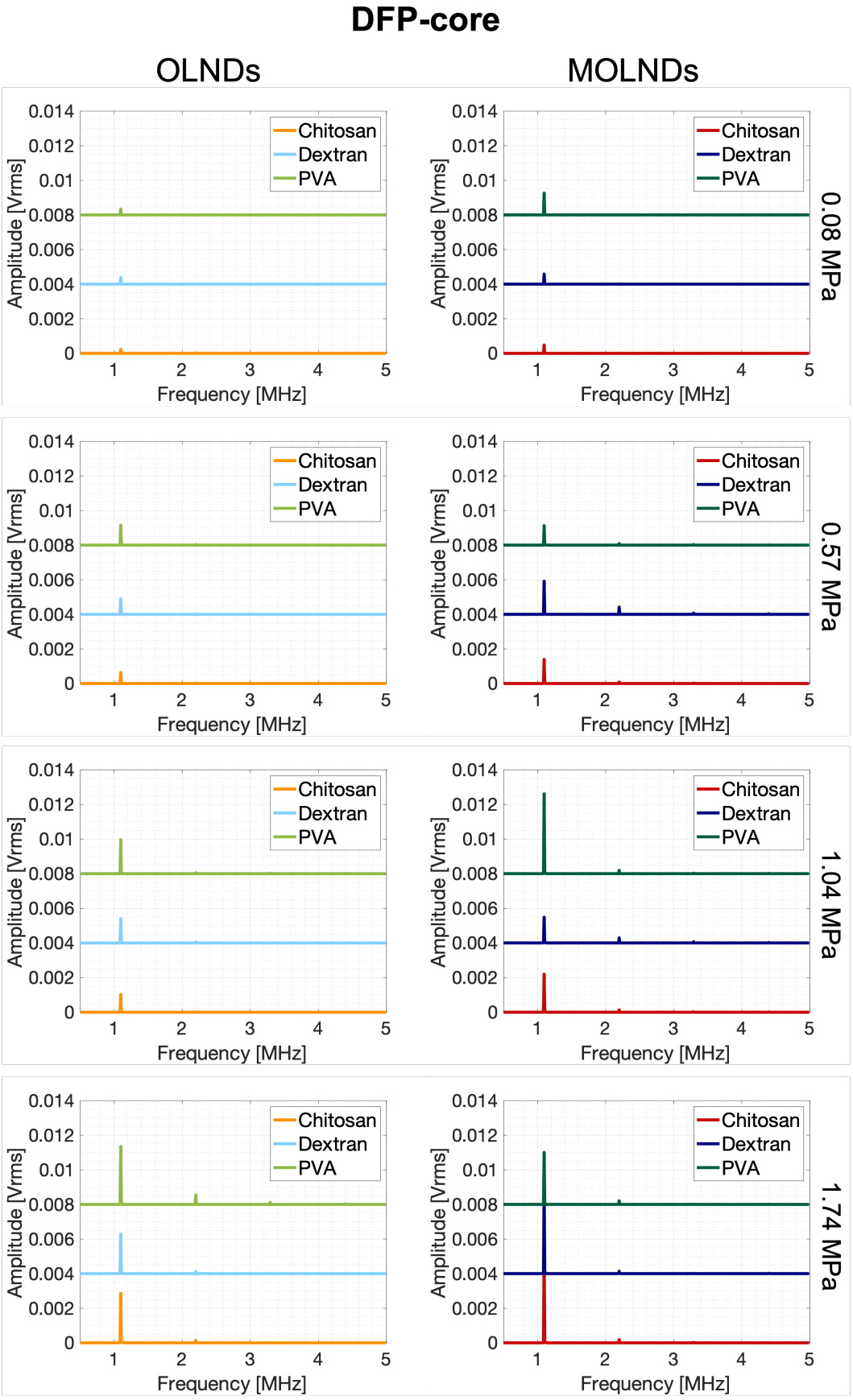

Fig. 4.19 FFT spectra of DFP-based OLNDs and MOLNDs at different acoustic pressures.

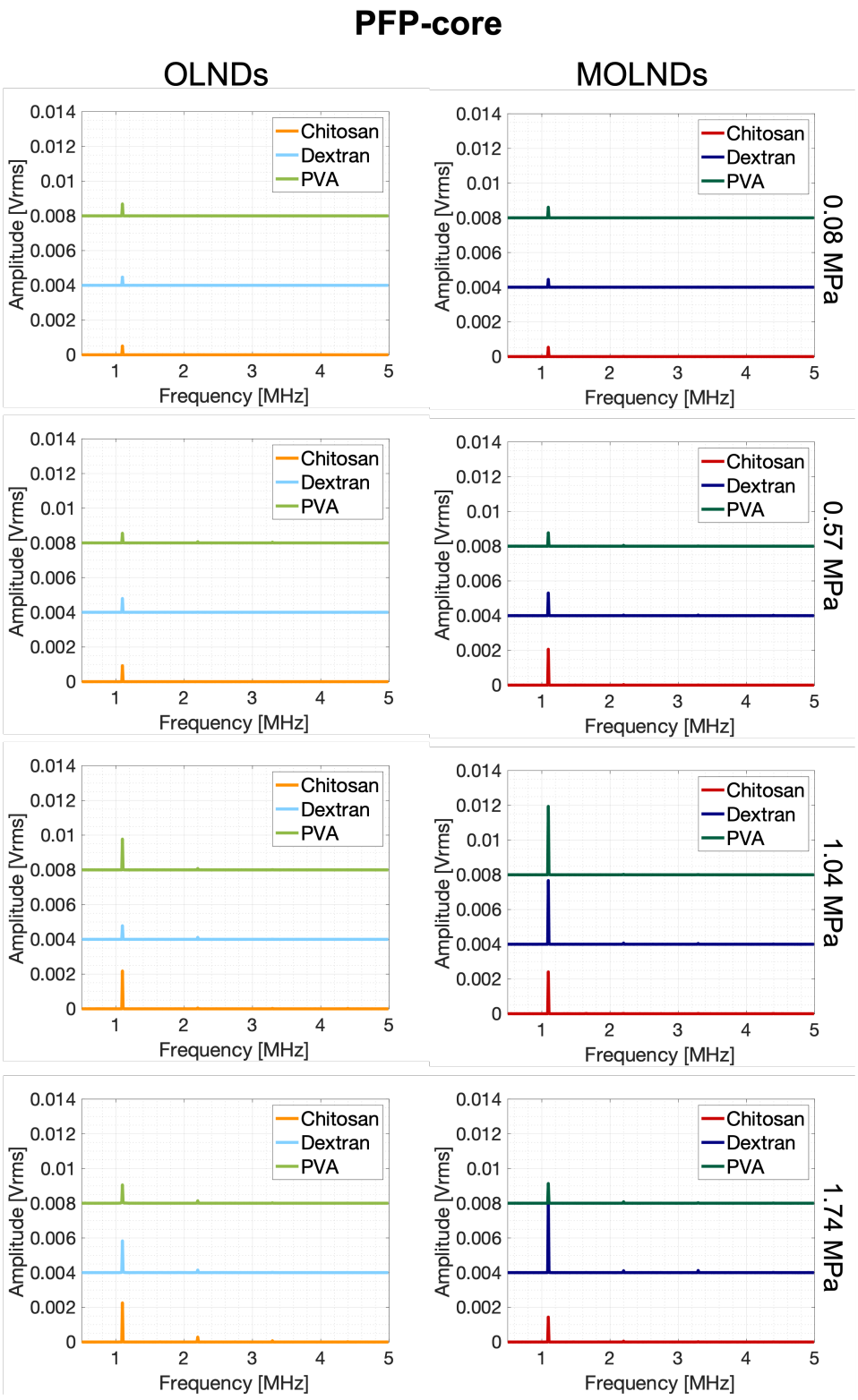

Fig. 4.20 FFT spectra of PFP-based OLNDs and MOLNDs at different acoustic pressures.

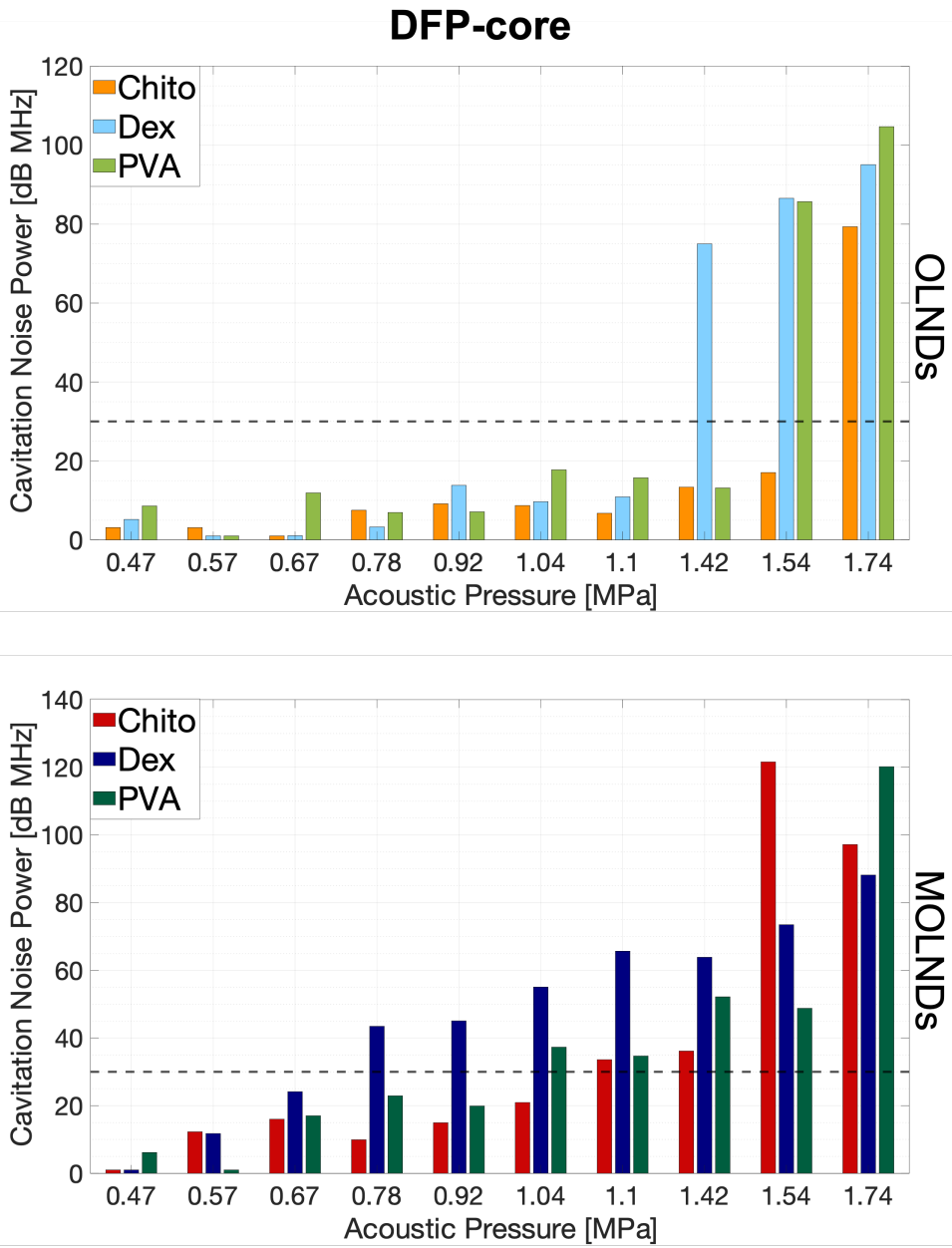

Fig. 4.21 Cavitation noise power analysis for DFP-core OLNDs and MOLNDs at different acoustic pressures.

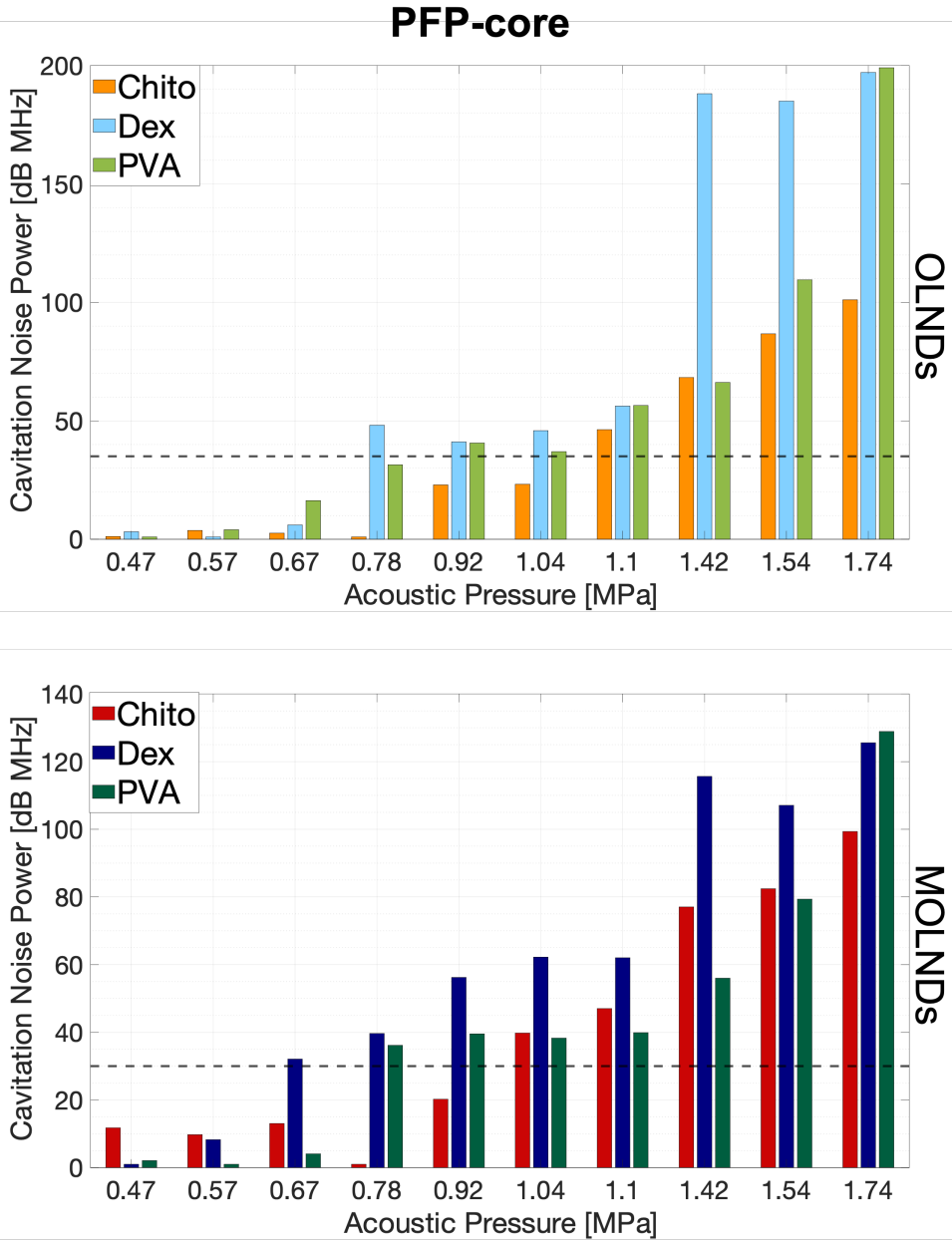

Fig. 4.22 Cavitation noise power analysis for PFP-core OLNDs and MOLNDs at different acoustic pressures.

4.2.3 Functionalization Assessment

After characterizing the samples, a crucial step is assessing the functionalization process as a mandatory requirement for the occurrence of MDV and, consequently, the release of oxygen.
Streaming velocity is an important parameter to provide information about the magnetic response of MOLNDs under a static magnetic field, induced by a permanent magnet placed in their proximity.The presence of the magnet generates an attractive force towards Fe_3O_4 NPs bound on the nanodroplet surface, affecting the trajectory of MOLNDs, thereby inducing streaming velocity variations and magnetic steering. As discussed in Section 3.3.4, two different setups have been implemented for this purpose. The first setup involves the use of an ecographic probe, while the second uses a microfluidics channel.
Through the ecographic approach, the trajectories of US-vaporized MOLNDs were collected in the absence or presence of a permanent magnet to evaluate their streaming velocity.

Figures 4.23 and 4.24 show a series of ecographic frames for DFP- and PFP-MOLNDs samples, both in the absence (top sequence) and presence (bottom sequence) of a magnet (highlighted by the yellow box). These figures allow for a qualitative assessment by comparing the droplet trajectories under two distinct conditions. In the presence of a static magnetic field, the droplets experience enhanced streaming with a preferred direction towards the magnet, as indicated by circles. Without the application of the field, MOLNDs exhibit random motion in all directions without demonstrating a preferential one.
Figure 4.25 reports the average velocities of MOLNDs under the two conditions mentioned above. The application of a magnetic field leads to a significant increase in streaming velocity, at least two times, thus confirming previous preliminary evidence and the successful functionalization. Moreover, the results also reveal a difference based on the coating type. In particular, in both PFC cases, the chitosan-coated MOLNDs show a higher streaming velocity compared to the others, which could be associated with a better functionalization rate. This behavior may be correlated to the electrostatic attraction between chitosan-coated OLNDs and Fe_3O_4 NPs, as confirmed by the ζ potential values reported in Table 4.1.

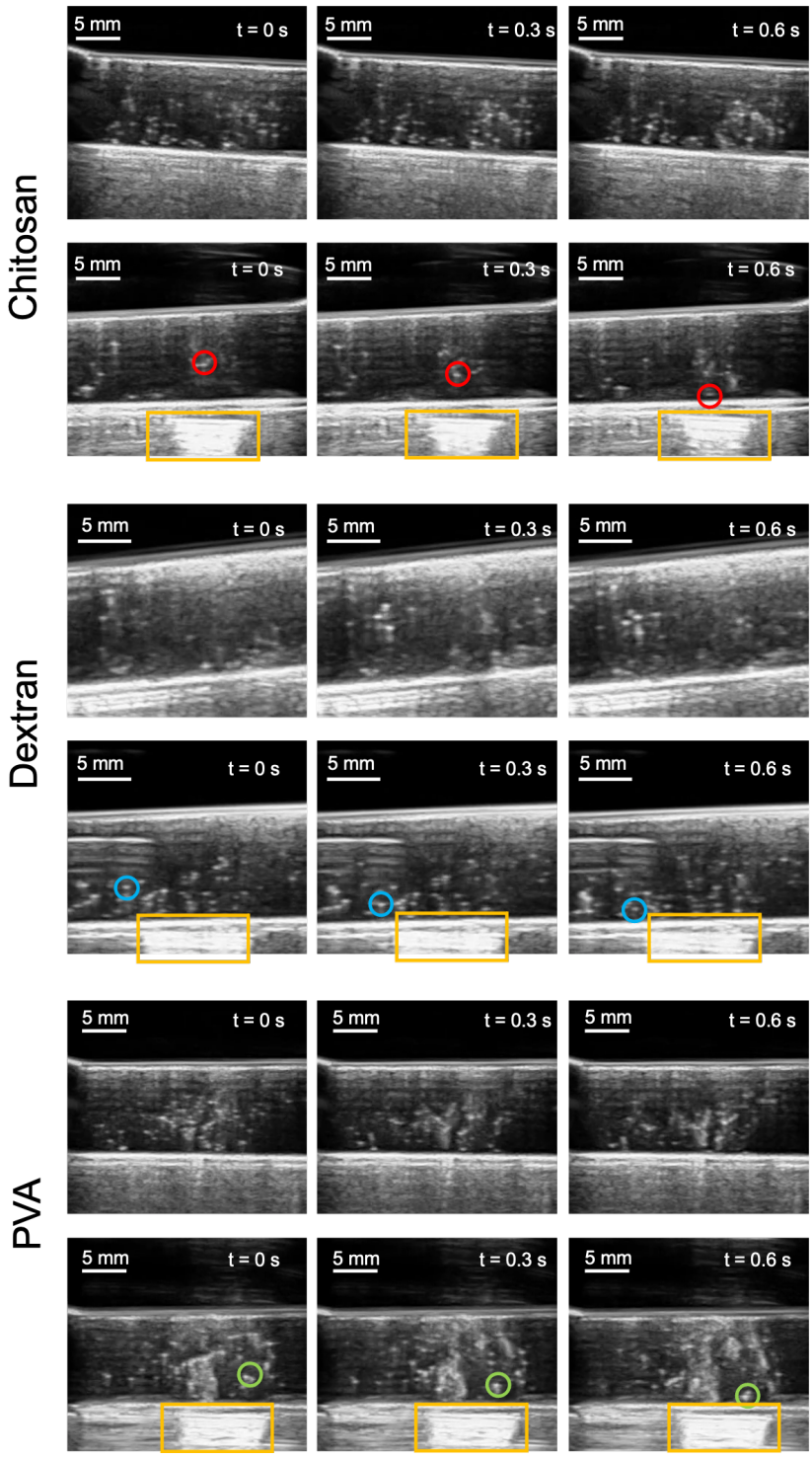

Fig. 4.23 Frames depicting the movement of DFP-MOLNDs at three successive times after the application of US. The top sequence shows the droplets without the presence of a permanent magnet, while the bottom sequence regards the droplets with the magnet, indicated by a yellow box. Circles are used to track one droplet movement over time.

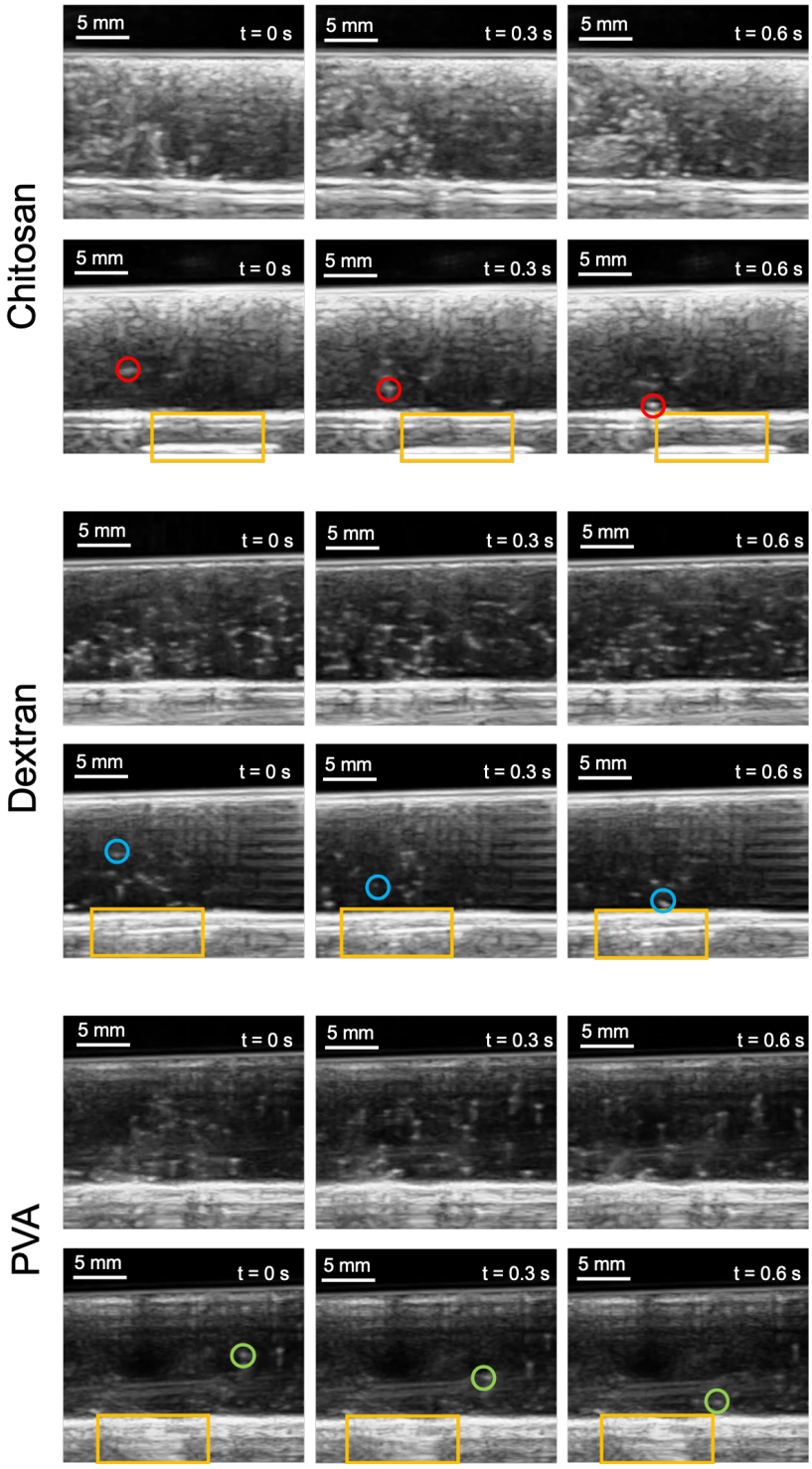

Fig. 4.24 Frames depicting the movement of DFP-MOLNDs at three successive times after the application of US. The top sequence shows the droplets without the presence of a permanent magnet, while the bottom sequence regards the droplets with the magnet, indicated by a yellow box. Circles are used to track one droplet movement over time.

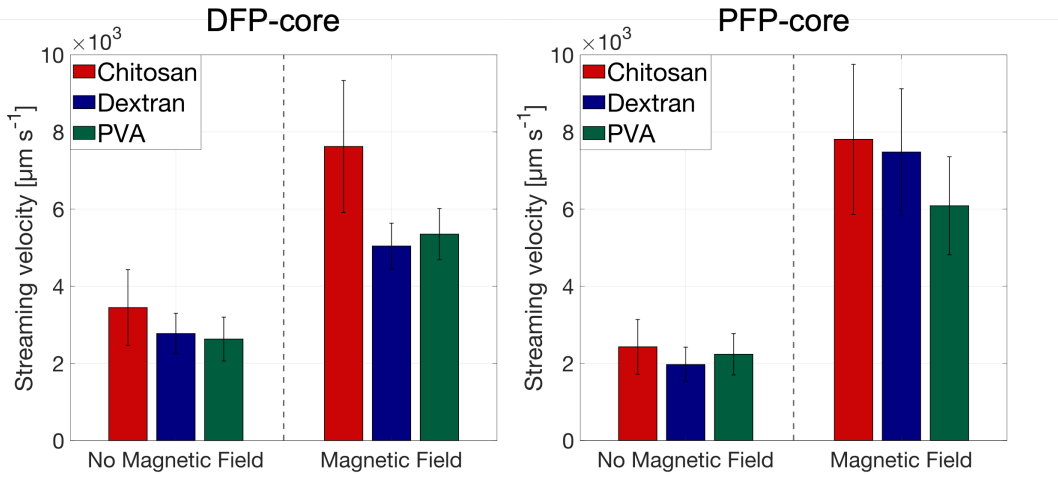

Fig. 4.25 Average streaming velocities of DFP- and PFP-MOLNDs in presence and in absence of the magnet.

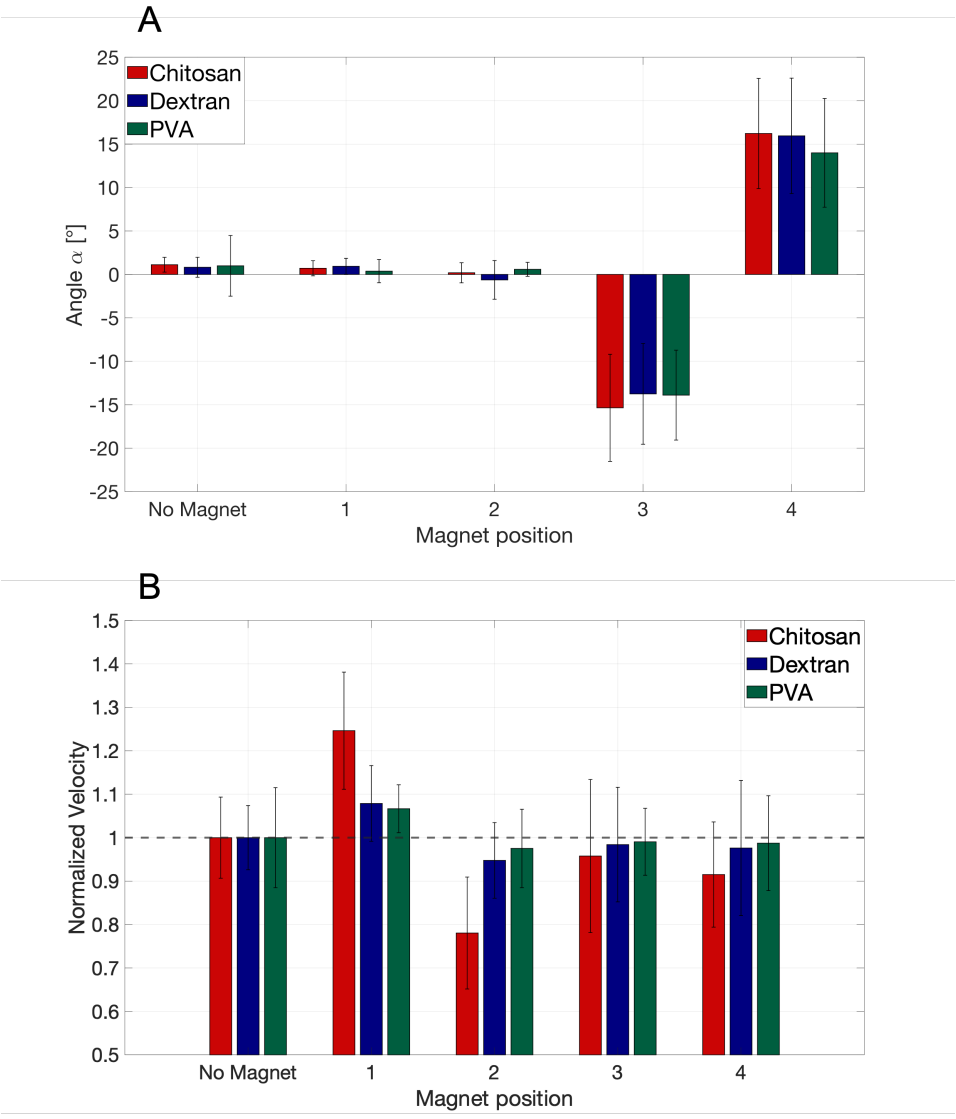

Fig. 4.26 A) Mean steering angle values and B) mean streaming velocity values obtained for DFP-MOLNDs samples through the microfluidic channel setup.

The second approach involved controlling the flow rate Q to record MOLND streaming inside a microfluidics channel (approximated as the average between the measured inlet and outlet flow rates $Q_{av} = \frac{Q_{in}+Q_{out}}{2} = \frac{11-8.5}{2}\ \mu L^{-1} = 9.8\ \mu L^{-1}$) and compare their velocity and steering angle in five different cases (as illustrated in Figure 3.9B). Figure 4.26A displays the steering angles obtained. The results indicate that placing the magnet laterally to the MOLNDs flow (positions 3-4) causes a deviation angle of approximately 15°C from the original trajectory, while the variation in this angle is not significant without the magnetic field or when the magnet is positioned along the flow trajectory (positions 1-2).
However, the analysis of the streaming velocity did not yield strong results, probably because the pump's flow velocity force was too strong to be affected by the magnet's presence. The only case where a visible variation was observed is for chitosan-coated MOLNDs, confirming the higher functionalization rate provided by the chitosan shell compared to the other cases. All these results confirm that the droplets are now magnetically responsive.

4.2.4 Magnetic Droplet Vaporization and Oxygen Release

In order to establish a basis for comparing the efficacy of acoustic and magnetic fields in inducing th release of oxygen, we induced the unload of OLNDs through an acoustic stimulus before evaluating the performance of MOLNDs in releasing oxygen. The results obtained for OLNDs are presented in Figure 4.27.

Upon analyzing first the two different cores, it is noteworthy that DFP-based nanodroplets (with a boiling temperature of 51 °C) exhibit a linear trend in the increase of oxygen concentration in the solution, with a significant increase up to 6 mg/L. In contrast, PFP-based nanodroplets (with a lower boiling temperature of approximately 29 °C) do not display a consistent rise in oxygen concentration over time. In particular, dextran- and PVA-coated samples show an initial spike in oxygen release upon US exposure, followed by a decrease in concentration. Only chitosan-coated OLNDs exhibit a similar increasing trend as DFP-based nanodroplets, likely due to the added rigidity provided by the chitosan structure to the nanocarrier.
Furthermore, observing the percentage uncertainties obtained in each measurement and reported in Table 4.3, the less stability provided by PFP based OLNDs is still confirmed by the fact that for PFP droplets, its values ranges from 2 % to 7 %, while in DFP case it does not overcome 2.5 %. The graphs presented in Figure 4.28

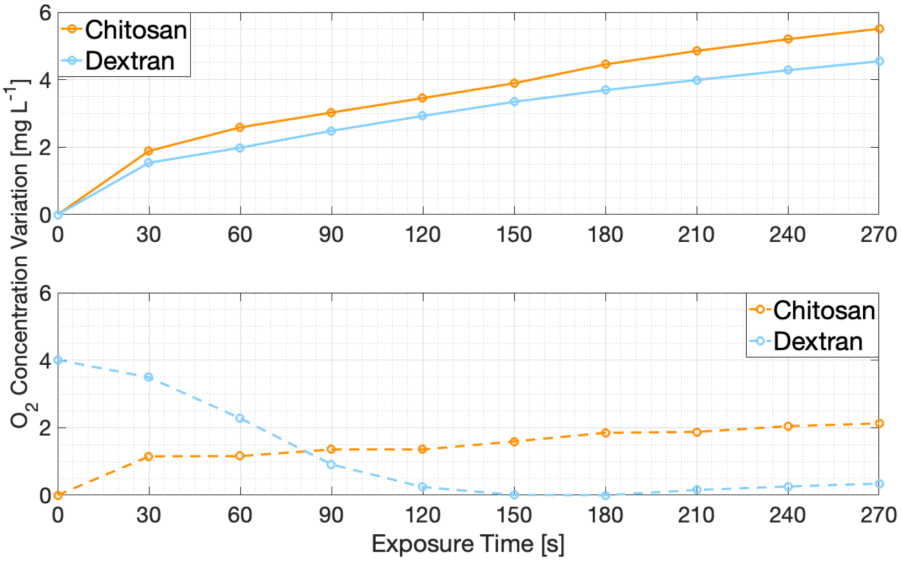

Fig. 4.27 Variation of the oxygen concentration measured during US irradiation in a solution of DFP- and PFP-OLNDs over time.

illustrate the concentrations of the oxygen released from MOLNDs when specific temperatures are reached into the solution thanks to the local heat generated by the interaction between Fe_3O_4 NPs and the AC magnetic field. A notable difference can be observed in the release of oxygen between the two core materials. Specifically, for DFP-based nanodroplets, oxygen is not released until the temperature reaches 45 °C, while for PFP-based droplets, a significant increase in oxygen concentration is observed at temperatures as low as 27 °C. This difference in behavior can be attributed to the boiling points of the two PFCs, although the temperatures at which the oxygen concentration starts to increase are slightly lower than their respective boiling points, 51 °C and 29 °C respectively. It is worth noting that the fiber optic probe used to measure the temperature records the average temperature in the solution, whereas the local temperature on the surfaces of the functionalized droplets is higher, approaching the actual boiling point of the PFC and thus enabling the vaporization process. From the perspective of biomedical applications, an important factor to consider is the human body temperature of 37 °C, as highlighted in the figure. In the case of PFP, in fact, the level of released oxygen is already high at lower temperatures, thus losing control over the oxygen release, as it would occur spontaneously as soon as the MOLNDs solution enters the bloodstream. On the contrary, DFP-MOLNDs at 37 degrees show almost no release of oxygen, making

Sample		Percentage Uncertainty (%)									
Core	Coating	$\mathbf{u_{0s}}$	$\mathbf{u_{30s}}$	$\mathbf{u_{60s}}$	$\mathbf{u_{90s}}$	$\mathbf{u_{120s}}$	$\mathbf{u_{150s}}$	$\mathbf{u_{180s}}$	$\mathbf{u_{210s}}$	$\mathbf{u_{240s}}$	$\mathbf{u_{270s}}$
DFP	**Chitosan**	1.8	1.4	1.2	1.2	1.3	1.3	1.4	1.4	1.4	1.4
	Dextran	1.4	1.2	1.2	1.1	1.1	1.0	1.0	1.0	1.0	1.1
	PVA	2.4	2.3	2.3	2.2	2.1	2.0	1.9	1.9	1.8	1.8
PFP	**Chitosan**	3.4	3.1	3.1	3.5	3.5	3.5	3.3	3.4	3.4	3.4
	Dextran	1.8	3.2	4.3	5.4	6.3	6.7	6.7	6.6	6.4	6.2
	PVA	4.2	4.3	4.9	5.4	5.7	5.8	5.7	5.6	5.5	5.4

Table 4.3 % uncertainties of the measurements of the oxygen concentration in OLNDs solution evaluated at 30 s intervals for a total of 270 s.

these platforms more suitable for their purpose.

Another interesting observation regarding the two PFCs is related to the release profile over time. As detailed in Section 3.3.6, following exposure to the magnetic field to reach the desired temperature, the oxygen concentration was measured for 270 seconds. Figure 4.29 depicts the release profile over time for DFP- and PFP-MOLNDs at their boiling temperatures, along with a second-order fit to visualize the behavior. It can be observed that in PFP-based samples (black lines), the amount of oxygen present in the solution tends to diminish over time, as it was already fully released at the beginning of the measurement. Conversely, DFP-MOLNDs (red lines) exhibit an increasing oxygen concentration over time until reaching a stable plateau, confirming the same behavior observed in the OLNDs case.

In terms of shell coating, both chitosan- and PVA-based MOLNDs show a significant amount of released oxygen compared to dextran-coated ones. However, the chitosan-coated droplets exhibit a significant amount already liberated at 48 °C and 27 °C for DFP and PFP, respectively. This observation confirms the higher level of functionalization provided by the chitosan coating, which was previously discussed in the dedicated paragraph.

The percentage uncertainties for MOLNDs were evaluated and reported in Table 4.4. Similar to the OLNDs case, it can be noticed that carriers based on PFP demonstrate higher uncertainty compared to DFP carriers, providing further confirmation of their lower reliability.

In order to investigate the role of MDV in oxygen release, MOLNDs samples were subjected to AC magnetic fields to reach targeted temperatures, and subse-

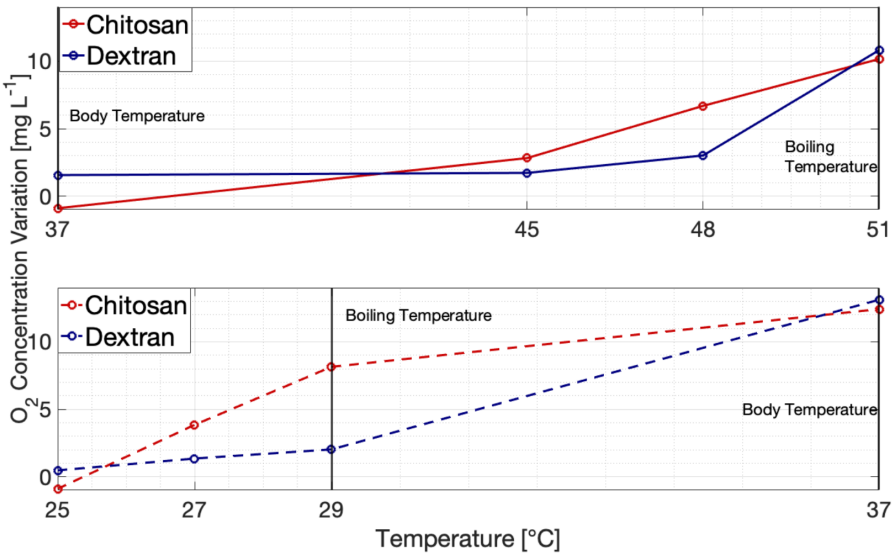

Fig. 4.28 Variation of the oxygen concentration measured after AC magnetic field excitation in a solution of DFP- and PFP-MOLNDs at different temperatures.

quently observed under an optical microscope. Figure 4.30 displays some images of the treated samples, clearly indicating that the MOLNDs have undergone the process of vaporization. One picture for each sample is depicted, focusing on one single bubble resulting after reaching the boiling temperature of the PFC employed. Additionally, aggregates of Fe_3O_4 nanoparticles are visible on the surface of the MOLNDs, as indicated by the white dashed circles depicted in each picture, confirming the functionalization that induces heating under magnetic field.

Analysis of the samples reveals that the vaporization process for PFP-MOLNDs initiates at approximately 27 °C, with a few bubbles appearing in the suspension. The number of bubbles gradually increases with temperature, reaching a maximum at 29 °C, before declining due to bubble implosion events. At 37°*C*, only a small number of bubbles remain. A similar trend is observed for DFP-MOLNDs, although the vaporization process occurs at a higher temperature range. Specifically, droplets start to vaporize at 45 °C, reach a maximum quantity at 48 °*C*, and then begin to decrease at 51 °C. This difference in behavior between DFP- and PFP-MOLNDs is related to the boiling temperatures of the two perfluorocarbons and the results obtained from oxygen release analysis. Notably, from this latter analysis, no substantial difference could be detected in terms of the employed coating.

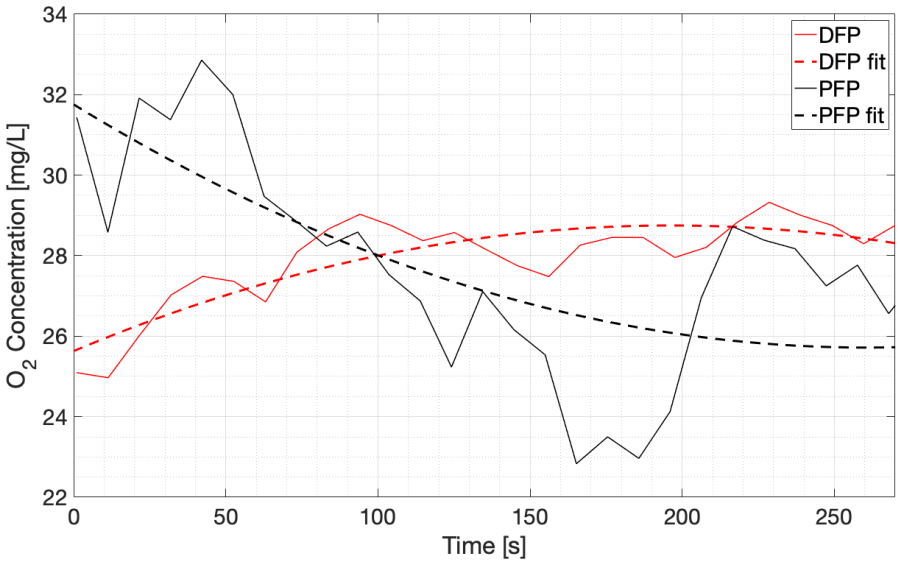

Fig. 4.29 Oxygen concentration profile measured in the 270 s following the MOLNDs sample heating by means of AC magnetic field up to DFP (red lines) and PFP (black lines) boiling points. The dashed lines represent the second order fit of the measurement data.

Table 4.4 % uncertainties of the measurements of the oxygen concentration in MOLNDs solution evaluated at each temperature considered.

Sample		Percentage Uncertainty (%)			
Core	Coating	$\mathbf{u_{37°C}}$	$\mathbf{u_{45°C}}$	$\mathbf{u_{48°C}}$	$\mathbf{u_{51°C}}$
DFP	**Chitosan**	4.0	6.4	4.1	5.4
	Dextran	6.3	6.0	5.4	4.2
	PVA	6.2	3.8	4.3	5.2
		$\mathbf{u_{25°C}}$	$\mathbf{u_{27°C}}$	$\mathbf{u_{29°C}}$	$\mathbf{u_{37°C}}$
PFP	**Chitosan**	9.0	8.0	9.4	9.0
	Dextran	5.3	9.4	9.2	9.6
	PVA	7.2	8.6	5.7	6.9

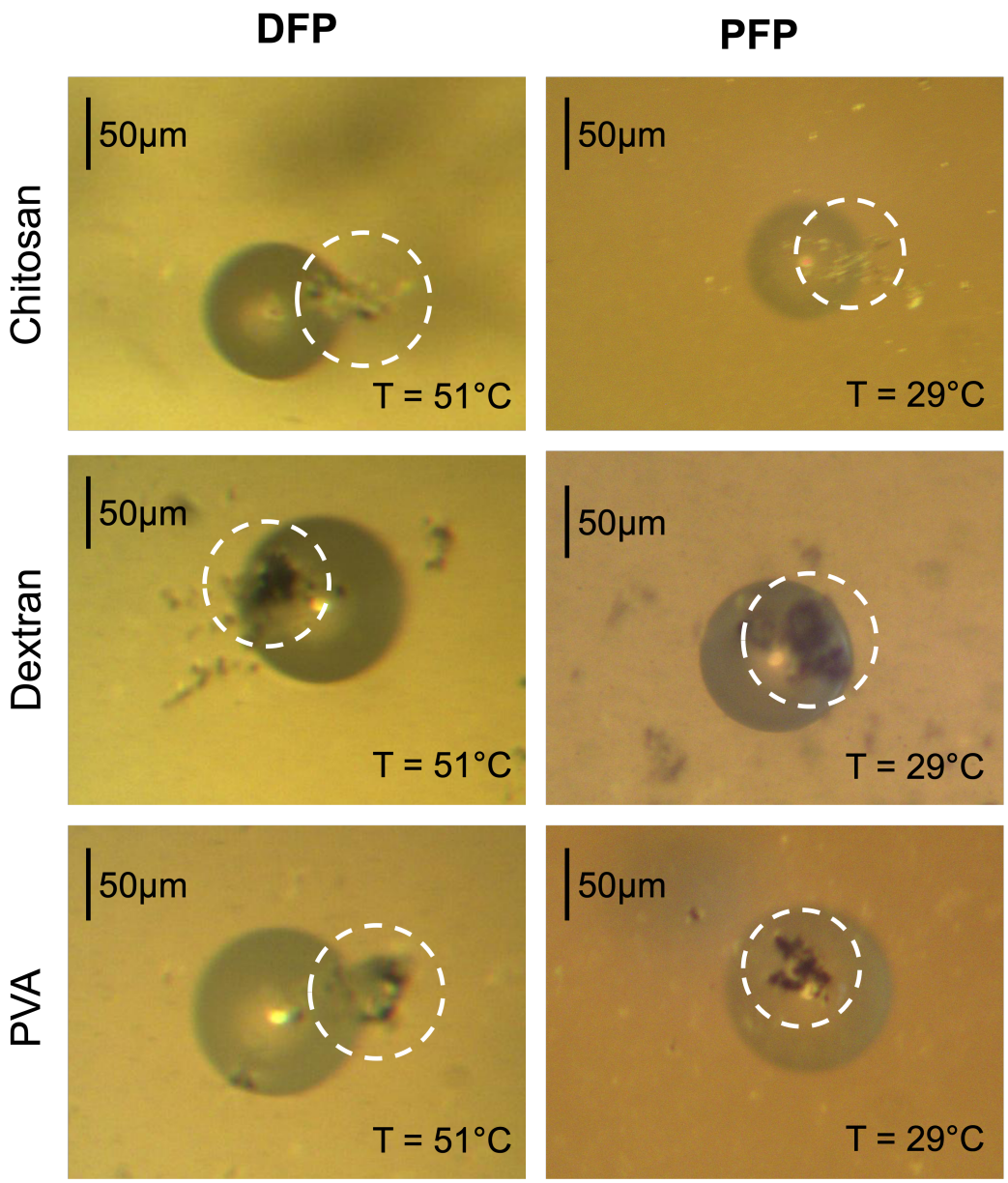

Fig. 4.30 Optical images of DFP- and PFP-MOLNDs after been subjected to an AC magnetic field, demonstrating the occurred MDV.

Chapter 5

Conclusions and Outlooks

This project aimed to develop and study sono-sensitive nanosystems able to release oxygen by means of an external stimulus. To this purpose, different types of perfluorocarbon-based phase-shift OLNDs have been synthesized. The mechanism behind the oxygen release is due to their interaction with US. When excited by an acoustic field, OLNDs undergo first acoustic droplet vaporization (ADV) passing from liquid nanodroplets to gaseous microbubbles, and then cavitation, oscillating close to their resonance dimension (stable cavitation) and finally collapsing (inertial cavitation). The controlled oxygen release happens during the oscillation step, while inertial cavitation leads to a violent collapse characterized by an uncontrolled temperature and pressure increases, dangerous for the surrounding environment. OLNDs have shown different interesting properties, from biocompatibility, inertness and stability, up to cheapness, synthesis simplicity and high release performances. Cavitation is a complex and tricky mechanism and its dynamics still represent a challenging debated field. From this, the necessity to give a contribution to the characterization of the phenomena behind the oxygen release induced by acoustic cavitation.

This work has been divided into two main sections, the first part more focused on the characterization of the signals emitted during the interaction between US and sono-sensitive carriers, while the second aimed to broaden the potential of OLNDs to be sensitive also to other external stimuli, such as the magnetic field.

In the first part of this work, three different sonocarriers have been used, two different DFP-based OLNDs, using PVA or chitosan as polymeric shell, and ZnO nanoparticles. The final goal was to build up a customized setup capable to monitor the response of the carriers to US stimuli through different sensors. Specifically, a PCD sensor, an ecographic probe and a high-speed camera where implemented in order to capture the acoustic, ecographic and optical signals, respectively, emitted by the carriers while flowing inside a channel drawn into a phantom made of materials able to mimic the acoustic properties of human soft tissues.
From the PCD analysis, information about stable cavitation can be extracted looking at the peaks present into the FFT spectra acquired. Samples ware excited at different acoustic pressures and the results were compared with the spectra obtained from pure water excitation, used as reference sample. Water demonstrated only the presence of a moderate main peak at the driven frequency of the US transducer also for high acoustic pressures, meaning that no bubbles are forming and oscillating into the solution. On the contrary, spectra captured during carriers excitation showed a fundamental peak whose amplitude noticeably increases with the rise of the acoustic pressure, and also the appearance of ultra-harmonics, related to non-linear oscillation phenomena. This confirmed the enhancement of stable cavitation events in presence of sonosensitive carriers into the solution.
Looking at the broadband noise, information about inertial cavitation could be obtained. Specifically, integrating the spectra above the entire frequency range acquired, without considering the contribution of the peaks, allowed to evaluate the CNP parameter, a numerical indicator of the amount of collapsing bubbles. The noise, in fact, is a consequence of the shock waves produced during the final bubble implosion. As for the stable cavitation, the pure water analysis demonstrated quasi-zero results for CNP at each acoustic pressure, confirming the absence also of inertial cavitation. Conversely, as the acoustic pressure increases, carriers show a significant increase of the parameter. From these two analysis, the working pressure range could be defined for each carrier in order to enable stable cavitation events and to avoid to enter the inertial regime. Chitosan-coated OLNDs demonstrated a shift of this range towards higher pressures, compared to the other two systems. This is due to the fact that chitosan provides a more rigid structure to the OLNDs shell respect to PVA. ZnO NPs, behaving as cavitation nuclei, generate bubbles starting from the gas molecules trapped in their structure, therefore they are not provided of a polymeric shell.
Ecographic imaging was used to obtain a real-time monitoring of the bubbles forma-

tion and oscillation inside the channel at different acoustic pressures. The analysis confirmed the absence of cavitation phenomena in case of water and a strong dependence on the pressure induced in case of the other carriers. At high acoustic pressures, indeed, an intense bubble formation was clearly visible inside the channel for all the three samples. Evaluating the intensity variation over time of the light spots during US excitation, inside a defined ROI within the channel, results coherent to the ones related to FFT spectra analysis could be obtained. This allowed to quantitatively characterized the same phenomenon - stable cavitation - using two different approaches. Also some qualitative information about inertial cavitation could be extracted by this approach. At the same pressures at which CNP analysis showed an increment of the bubbles collapse activity, some intense light spots, typical of the presence of air, in this case due by the bubble implosion, were detected by the ecographic probe.

Finally, the high-speed camera frames demonstrated the possibility to understand the bubbles group behavior related to each sample under the excitation of an acoustic field. In particular, PVA-coated OLNDs were characterized by a more intensive agglomeration and merging trend, compared to chitosan-based ones, due to an intensification of the attractive forces which characterize the cavitation phenomena and lead to the consequent bubbles collapse. Bubbles derived from ZnO NPs, on the contrary, demonstrated to be more prone to undergo the coalescence process, being their structure less stable.

The optical section of the setup demonstrated some limitations in achieving a recording speed high enough to appreciate single bubbles dynamics. For this reason, a second setup to improve the optical imaging section was proposed, gaining the possibility to obtain higher magnifications by means of different objective lens and to reach a recording frame rate one order of magnitude higher than the previous setup (up to 10000 fps), thanks to exploitation of a more intense light source. Through this enhanced setup, some statistics on the bubbles life times and streaming velocities were evaluated as a function of the working acoustic pressure. Furthermore, thanks to the degree of freedom gained on the image magnification, coalescence phenomena between adjacent bubbles could be recorded and investigated. Although some information has been extracted from this setup, the recording rate is not yet high enough to appreciate dynamics on single bubbles oscillation and collapse. However, it resulted a promising starting point to further increase the acquisition rate, trying to couple and synchronize the bubble oscillating frequency with the light source in

strobe modality.

The second part of this research was focused on the development of dual-stimuli responsive OLNDs in order to overcome the limits of US field in reaching deeper regions of the human body. To this aim, magnetic Fe_3O_4 NPs were bound on the nanodroplets surface obtaining the so-called MOLNDs. These new kind of platforms have been already studied as carriers used to perform US-based imaging during magnetic hypothermia for cancer cells treatment, but their potential as alternative oxygen delivery systems triggered by magnetic field was investigated. The idea is to exploit the interaction between the nanoparticles and an AC magnetic field to induce a local heat on the nanodroplets surface able to induce MDV for enabling the oxygen release.
First, an process for optimizing MOLNDs preparation was proposed, using DFP and PFP as perfluorocarbon cores, characterized by a boiling temperature of ≈ 29 °C and ≈ 51°C respectively, and chitosan, dextran and PVA as polymeric shells, obtaining in this way six different samples. The first analysis performed regarded the characterization of the physico-chemical properties of the new platforms. The shape and structure was investigated through scanning and transmission electron microscopies, obtaining also a first assessment of the bounding of the particles on the droplets surfaces. Also the hydrodynamic mean diameter and ζ potential were measured, observing an increment of the carriers size and a worsening of the colloidal stability due to the presence of the nanoparticles. ζ potential analysis, moreover, demonstrated that chitosan-OLNDs and Fe_3O_4 NPs have opposite sign electrostatic potential, so expecting a better attraction, and consequentially bonding, compared to the other coatings. The influence of the NPs was also evaluated on the acoustic response. Through an US transducer, OLNDs and MOLNDs were excited while flowing into a channel and it was found that the particles behave in the solution as scattering points for the acoustic field, leading to a further increase of the local pressure and thus to an enhancement of the cavitation activity.
At this point, two different setups were implemented in order to assess the magnetic functionalization, evaluating the influence of a permanent magnet inducing a static magnetic field. The first used the ecographic probe in order to monitor the trajectories of US-activated MOLNDs in the presence and absence of the magnet. Results showed a preferential and significantly accelerated motion when the magnet was placed in the sample proximity. The second approach measured the variations in the

streaming velocity and steering angles due to the presence of the static magnetic field during the sample flow in a microfluidic channel controlled by a microfluidic pump at constant pressure. All the results, therefore, demonstrated the magnetic response of the carriers to a static field, meaning that carriers were actually magnetic.
To complete the study, the measurement of MOLNDs oxygen release induced by an alternating magnetic field was conducted. Through a fiber optic probe, the temperature of the solution was monitored while an AC magnetic field excited the samples. When specific temperatures were reached, depending on the PFC boiling point, the oxygen concentration into the solution was measured for 5 minutes. All the results were then compared with the oxygen release profiles obtained by US-activated OLNDs. Furthermore, in order to ensure that the release was due to MDV mechanism, the samples were observed at an optical microscope, through which the presence of vaporized bubbles was revealed. The comparison between acoustic and magnetic stimuli for the oxygen release demonstrated MDV as promising therapeutic approach, comparable in its performances to the acoustic traditional method. From the measurements on the two different cores, it came out how the DFP-based MOLNDs are more suitable for biomedical applications compared to PFP-based ones. At the human body temperature (37 °C), in fact, the latter would spontaneously undergo MDV process, loosing the control on the oxygen release because of the low boiling temperature (29 °C). Thanks to the higher boiling point (51 °C), on the other hand, DFP-based MOLNDs can be activated only through the interaction with an alternating magnetic field.
Considering the coatings, it could be noticed a more efficient release profile of chitosan-coated MOLNDs thanks to its more rigid nature compared to dextran and PVA. Already at 45 °C, chitosan-shelled samples provided an increase of the oxygen concentration in the solution. This result is in good agreement with the higher functionalization rate performed by chitosan and previously explained.
Starting from the interesting results obtained up to now, a series of possible works are going to be developed to further improve MOLNDs efficacy and performances. In particular, the next step relies the exploitation of the micropump already used for the functionalization assessment also for the sample synthesis. Designing a customized microfluidic chip, droplets can be, in fact, prepared in a more controlled way, overcoming the limitations in the size distribution proper of the homogenization-based methods. In this way it is expected to optimize all the results already performed, minimizing from a metrological point of view the measurement uncertainties and

increasing the release control.
Moreover, the use of this kind of synthesis approach could allow to directly integrate the magnetic nanoparticles functionalization step in one of the droplet synthesis procedure. An idea is to incorporate them within the core solution, in order to get a control on the amount of particles encapsulated in each droplet, avoiding their waste. Also in-vitro study are planned to be conducted to investigate the cytotoxicity and biocompatibility of MOLNDs and to evaluate the cells response to their contact.

References

[1] Avanti Europe AG. Understanding drug delivery routes. https://www.avanti-europe.ch/understanding-drug-delivery-routes/, 2020.

[2] S. Adepu and S. Ramakrishna. Controlled drug delivery systems: current status and future directions. *Molecules*, 26(19):5905, 2021.

[3] W. Zhang, Y. Shi, S. Abd Shukor, A. Vijayakumaran, S. Vlatakis, M. Wright, and M. Thanou. Phase-shift nanodroplets as an emerging sonoresponsive nanomaterial for imaging and drug delivery applications. *Nanoscale*, 2022.

[4] T. Leong, M. Ashokkumar, and S. Kentish. The fundamentals of power ultrasound-a review. 2011.

[5] R.E. Apfel. Acoustic cavitation prediction. *The Journal of the Acoustical Society of America*, 69(6):1624–1633, 1981.

[6] J. Jiao, Y. He, K. Yasui, S. E Kentish, M. Ashokkumar, R. Manasseh, and J. Lee. Influence of acoustic pressure and bubble sizes on the coalescence of two contacting bubbles in an acoustic field. *Ultrasonics sonochemistry*, 22:70–77, 2015.

[7] J.R. Waldram. The theory of thermodynamics. *The Theory of Thermodynamics*, 1985.

[8] P.A. Mountford and M.A. Borden. On the thermodynamics and kinetics of superheated fluorocarbon phase-change agents. *Advances in colloid and interface science*, 237:15–27, 2016.

[9] A. Troia, V. Cauda, G. Canavese, A. Ancona, F. Zagallo, G. Leonetti, and S. Galati. Novel contrast agents and increasing tools for radicals generation in low intensity ultrasound based on porous oxides. In *Proceedings of Meetings on Acoustics ICU*, volume 38, page 020015. Acoustical Society of America, 2019.

[10] M. Vassallo, D. Martella, G. Barrera, F. Celegato, M. Coisson, R. Ferrero, E.S. Olivetti, A. Troia, H. Sozeri, C. Parmeggiani, D. S. Wiersma, P. Tiberto, and A. Manzin. Improvement of hyperthermia properties of iron oxide nanoparticles by surface coating. *ACS Omega*, 8(2):2143–2154, 2023.

[11] P. Couvreur. Nanoparticles in drug delivery: past, present and future. *Advanced drug delivery reviews*, 65(1):21–23, 2013.

[12] M.J. Mitchell, M.M. Billingsley, R.M. Haley, M.E. Wechsler, N.A. Peppas, and R. Langer. Engineering precision nanoparticles for drug delivery. *Nature Reviews Drug Discovery*, 20(2):101–124, 2021.

[13] L. Kou, Y.D. Bhutia, Q. Yao, Z. He, J. Sun, and V. Ganapathy. Transporter-guided delivery of nanoparticles to improve drug permeation across cellular barriers and drug exposure to selective cell types. *Frontiers in pharmacology*, 9:27, 2018.

[14] F.S. Collins and H. Varmus. A new initiative on precision medicine. *New England journal of medicine*, 372(9):793–795, 2015.

[15] P. Verma, A.S. Thakur, K. Deshmukh, A.K. Jha, and S. Verma. Routes of drug administration. *International Journal of Pharmaceutical Studies and Research*, 1(1):54–59, 2010.

[16] R. Langer. Drug delivery and targeting. *Nature*, 392(6679 Suppl):5–10, 1998.

[17] S.P. Chaudhari and P.S. Patil. Pharmaceutical excipients: a review. *Int J Adv Pharm Biol Chem*, 1(1):21–34, 2012.

[18] K. K. Jain. An overview of drug delivery systems. *Drug delivery systems*, pages 1–54, 2020.

[19] S.S. Jambhekar and P.J. Breen. *Basic pharmacokinetics*, volume 76. Pharmaceutical press London, 2009.

[20] J. K. Seydel and M. Wiese. *Drug-membrane interactions: analysis, drug distribution, modeling*. John Wiley & Sons, 2009.

[21] J.R. Gillette. Factors affecting drug metabolism. *Annals of the New York Academy of Sciences*, 179(1):43–66, 1971.

[22] S. Ekins, B.J. Ring, J. Grace, D.J. McRobie-Belle, and S.A. Wrighton. Present and future in vitro approaches for drug metabolism. *Journal of pharmacological and toxicological methods*, 44(1):313–324, 2000.

[23] R. Langer. New methods of drug delivery. *Science*, 249(4976):1527–1533, 1990.

[24] M. P. Paarakh, P. A. Jose, C.M. Setty, and G.P. Christoper. Release kinetics–concepts and applications. *Int. J. Pharm. Res. Technol*, 8(1):12–20, 2018.

[25] S. Habet. Narrow therapeutic index drugs: clinical pharmacology perspective. *Journal of Pharmacy and Pharmacology*, 73(10):1285–1291, 2021.

[26] S.M. Huang, J.J.L. Lertora, and Arthur J. Atkinson Jr. *Principles of clinical pharmacology*. Academic Press, 2012.

[27] O.S. Fenton, K.N. Olafson, P.S. Pillai, M.J. Mitchell, and R. Langer. Advances in biomaterials for drug delivery. *Advanced Materials*, 30(29):1705328, 2018.

[28] A.P. Singh, A. Biswas, A. Shukla, and P. Maiti. Targeted therapy in chronic diseases using nanomaterial-based drug delivery vehicles. *Signal transduction and targeted therapy*, 4(1):1–21, 2019.

[29] B.P. Gupta, N. Thakur, N.P. Jain, J. Banweer, and S. Jain. Osmotically controlled drug delivery system with associated drugs. *Journal of Pharmacy & Pharmaceutical Sciences*, 13(4):571–588, 2010.

[30] Z. Wang and R.A. Shmeis. Dissolution controlled drug delivery systems. *Design of controlled release drug delivery systems. United States: McGraw-Hill*, pages 139–72, 2006.

[31] J. Siepmann, R.A. Siegel, M.J. Rathbone, et al. *Fundamentals and applications of controlled release drug delivery*, volume 3, pages 127–152. Springer, 2012.

[32] J. Siepmann and F. Siepmann. Modeling of diffusion controlled drug delivery. *Journal of controlled release*, 161(2):351–362, 2012.

[33] S. Srikonda, P. Kotamraj, and B. Barclay. Osmotic controlled drug delivery systems. *Design of Controlled Release Drug Delivery Systems*, page 203, 2006.

[34] J. Siepmann, R.A. Siegel, M.J. Rathbone, et al. *Fundamentals and applications of controlled release drug delivery*, volume 3, pages 153–150. Springer, 2012.

[35] J. Kopeček. Polymer–drug conjugates: Origins, progress to date and future directions. *Advanced drug delivery reviews*, 65(1):49–59, 2013.

[36] C.M. Wells, M. Harris, L. Choi, V.P. Murali, F. D. Guerra, and J.A. Jennings. Stimuli-responsive drug release from smart polymers. *Journal of functional biomaterials*, 10(3):34, 2019.

[37] S.O. Adeosun, M.O. Ilomuanya, O.P. Gbenebor, M.O. Dada, and C.C. Odili. Biomaterials for drug delivery: sources, classification, synthesis, processing, and applications. *Advanced functional materials*, pages 141–167, 2020.

[38] S. Mura, J. Nicolas, and P. Couvreur. Stimuli-responsive nanocarriers for drug delivery. *Nature materials*, 12(11):991–1003, 2013.

[39] A. Raza, T. Rasheed, F. Nabeel, U. Hayat, M. Bilal, and H.M.N. Iqbal. Endogenous and exogenous stimuli-responsive drug delivery systems for programmed site-specific release. *Molecules*, 24(6):1117, 2019.

[40] Z. Deng, Z. Zhen, X. Hu, S. Wu, Z. Xu, and P.K. Chu. Hollow chitosan–silica nanospheres as ph-sensitive targeted delivery carriers in breast cancer therapy. *Biomaterials*, 32(21):4976–4986, 2011.

[41] K.H. Min, J.H. Kim, S.M. Bae, H. Shin, M. S. Kim, S. Park, H. Lee, R.W. Park, I.S. Kim, K. Kim, et al. Tumoral acidic ph-responsive mpeg-poly (β-amino ester) polymeric micelles for cancer targeting therapy. *Journal of Controlled Release*, 144(2):259–266, 2010.

[42] G.H. Gao, M.J. Park, Y. Li, G.H. Im, J.-H. Kim, H.N. Kim, J.W. Lee, P. Jeon, O.Y. Bang, J.H. Lee, et al. The use of ph-sensitive positively charged polymeric micelles for protein delivery. *Biomaterials*, 33(35):9157–9164, 2012.

[43] E.S. Lee, Z. Gao, D. Kim, K. Park, I.C. Kwon, and Y.H. Bae. Super ph-sensitive multifunctional polymeric micelle for tumor phe specific tat exposure and multidrug resistance. *Journal of Controlled Release*, 129(3):228–236, 2008.

[44] E. Koren, A. Apte, A. Jani, and V.P. Torchilin. Multifunctional pegylated 2c5-immunoliposomes containing ph-sensitive bonds and tat peptide for enhanced tumor cell internalization and cytotoxicity. *Journal of controlled release*, 160(2):264–273, 2012.

[45] M. Upreti, A. Jyoti, and P. Sethi. Tumor microenvironment and nanotherapeutics. *Translational cancer research*, 2(4):309–319, 2013.

[46] Q. Hu, P.S. Katti, and Z. Gu. Enzyme-responsive nanomaterials for controlled drug delivery. *Nanoscale*, 6(21):12273–12286, 2014.

[47] E. Fleige, M. A Quadir, and R. Haag. Stimuli-responsive polymeric nanocarriers for the controlled transport of active compounds: concepts and applications. *Advanced drug delivery reviews*, 64(9):866–884, 2012.

[48] C. Zhang, D. Pan, J. Li, J. Hu, A. Bains, N. Guys, H. Zhu, Xiaohui Li, K. Luo, Q. Gong, et al. Enzyme-responsive peptide dendrimer-gemcitabine conjugate as a controlled-release drug delivery vehicle with enhanced antitumor efficacy. *Acta biomaterialia*, 55:153–162, 2017.

[49] F. Meng, W.E. Hennink, and Z. Zhong. Reduction-sensitive polymers and bioconjugates for biomedical applications. *Biomaterials*, 30(12):2180–2198, 2009.

[50] G.K. Such, Y. Yan, A.P.R. Johnston, S.T. Gunawan, and F. Caruso. Interfacing materials science and biology for drug carrier design. *Advanced Materials*, 27(14):2278–2297, 2015.

[51] G. Wu, Y.Z. Fang, S. Yang, J. R Lupton, and N.D. Turner. Glutathione metabolism and its implications for health. *The Journal of nutrition*, 134(3):489–492, 2004.

[52] M. Bikram and J.L. West. Thermo-responsive systems for controlled drug delivery. *Expert opinion on drug delivery*, 5(10):1077–1091, 2008.

[53] D.G. Dastidar and G. Chakrabarti. Thermoresponsive drug delivery systems, characterization and application. In *Applications of Targeted Nano Drugs and Delivery Systems*, pages 133–155. Elsevier, 2019.

[54] C.S. Linsley and B.M. Wu. Recent advances in light-responsive on-demand drug-delivery systems. *Therapeutic delivery*, 8(2):89–107, 2017.

[55] W. Zhao, Y. Zhao, Q. Wang, T. Liu, J. Sun, and R. Zhang. Remote light-responsive nanocarriers for controlled drug delivery: Advances and perspectives. *Small*, 15(45):1903060, 2019.

[56] W. Park, B.C. Bae, and K. Na. A highly tumor-specific light-triggerable drug carrier responds to hypoxic tumor conditions for effective tumor treatment. *Biomaterials*, 77:227–234, 2016.

[57] P. Alonso-Cristobal, O. Oton-Fernandez, D. Mendez-Gonzalez, J.F. Díaz, E. Lopez-Cabarcos, I. Barasoain, and J. Rubio-Retama. Synthesis, characterization, and application in hela cells of an nir light responsive doxorubicin delivery system based on nayf4: Yb, tm@ sio2-peg nanoparticles. *ACS applied materials & interfaces*, 7(27):14992–14999, 2015.

[58] A. Higuchi, A. Hamamura, Y. Shindo, H. Kitamura, B.O. Yoon, T. Mori, T. Uyama, and A. Umezawa. Photon-modulated changes of cell attachments on poly (spiropyran-co-methyl methacrylate) membranes. *Biomacromolecules*, 5(5):1770–1774, 2004.

[59] S. Son, E. Shin, and B.S. Kim. Light-responsive micelles of spiropyran initiated hyperbranched polyglycerol for smart drug delivery. *Biomacromolecules*, 15(2):628–634, 2014.

[60] S.O. Poelma, S.S. Oh, S. Helmy, A.S. Knight, G.L. Burnett, H.T. Soh, C.J. Hawker, and J.. de Alaniz. Controlled drug release to cancer cells from modular one-photon visible light-responsive micellar system. *Chemical Communications*, 52(69):10525–10528, 2016.

[61] M.C. Chen, M.H. Ling, K.W. Wang, Z.W. Lin, B.H. Lai, and D.H. Chen. Near-infrared light-responsive composite microneedles for on-demand transdermal drug delivery. *Biomacromolecules*, 16(5):1598–1607, 2015.

[62] D. Wang and S. Wu. Red-light-responsive supramolecular valves for photo-controlled drug release from mesoporous nanoparticles. *Langmuir*, 32(2):632–636, 2016.

[63] S. Laurent, Si. Dutz, U.O. Häfeli, and M. Mahmoudi. Magnetic fluid hyperthermia: focus on superparamagnetic iron oxide nanoparticles. *Advances in colloid and interface science*, 166(1-2):8–23, 2011.

[64] G.K. Thirunavukkarasu, K. Cherukula, H. Lee, Y.Y. Jeong, I.K. Park, and J.Y. Lee. Magnetic field-inducible drug-eluting nanoparticles for image-guided thermo-chemotherapy. *Biomaterials*, 180:240–252, 2018.

[65] S. Jacob, A.B Nair, J. Shah, N. Sreeharsha, S. Gupta, and P. Shinu. Emerging role of hydrogels in drug delivery systems, tissue engineering and wound management. *Pharmaceutics*, 13(3):357, 2021.

[66] V. Pillay, T.S. Tsai, Y.E. Choonara, L.C. du Toit, P. Kumar, G. Modi, D. Naidoo, L.K. Tomar, C. Tyagi, and V.M.K. Ndesendo. A review of integrating electroactive polymers as responsive systems for specialized drug delivery applications. *Journal of Biomedical Materials Research Part A*, 102(6):2039–2054, 2014.

[67] H. Lee, W. Hong, S. Jeon, Y. Choi, and Y. Cho. Electroactive polypyrrole nanowire arrays: synergistic effect of cancer treatment by on-demand drug release and photothermal therapy. *Langmuir*, 31(14):4264–4269, 2015.

[68] Z. Atoufi, P. Zarrintaj, G.H. Motlagh, A. Amiri, Z. Bagher, and S.K. Kamrava. A novel bio electro active alginate-aniline tetramer/agarose scaffold for tissue engineering: synthesis, characterization, drug release and cell culture study. *Journal of Biomaterials science, Polymer edition*, 28(15):1617–1638, 2017.

[69] R. Jia, L. Teng, L. Gao, T. Su, L. Fu, Z. Qiu, and Y. Bi. Advances in multiple stimuli-responsive drug-delivery systems for cancer therapy. *International Journal of Nanomedicine*, 16:1525, 2021.

[70] X. Fu, L. Hosta-Rigau, R. Chandrawati, and J. Cui. Multi-stimuli-responsive polymer particles, films, and hydrogels for drug delivery. *Chem*, 4(9):2084–2107, 2018.

[71] L. Wei, J. Chen, and J. Ding. Sequentially stimuli-responsive anticancer nanomedicines, 2021.

[72] A. Carovac, F. Smajlovic, and D. Junuzovic. Application of ultrasound in medicine. *Acta Informatica Medica*, 19(3):168, 2011.

[73] P.N.T. Wells. Ultrasound imaging. *Physics in Medicine & Biology*, 51(13):R83, 2006.

[74] E.P. Stride and C.C. Coussios. Cavitation and contrast: The use of bubbles in ultrasound imaging and therapy. *Proceedings of the Institution of Mechanical Engineers, Part H: Journal of Engineering in Medicine*, 224(2):171–191, 2010.

[75] M.L. James and S.S. Gambhir. A molecular imaging primer: modalities, imaging agents, and applications. *Physiological reviews*, 92(2):897–965, 2012.

[76] A. Zlitni and S.S. Gambhir. Molecular imaging agents for ultrasound. *Current opinion in chemical biology*, 45:113–120, 2018.

[77] D. Cosgrove and C. Harvey. Clinical uses of microbubbles in diagnosis and treatment. *Medical & biological engineering & computing*, 47(8):813–826, 2009.

[78] K.H. Martin and P.A. Dayton. Current status and prospects for microbubbles in ultrasound theranostics. *Wiley Interdisciplinary Reviews: Nanomedicine and Nanobiotechnology*, 5(4):329–345, 2013.

[79] W.L. Nyborg. Biological effects of ultrasound: development of safety guidelines. part ii: general review. *Ultrasound in medicine & biology*, 27(3):301–333, 2001.

[80] Wi.G. Pitt, G.A. Husseini, and B.J. Staples. Ultrasonic drug delivery–a general review. *Expert opinion on drug delivery*, 1(1):37–56, 2004.

[81] H. Chen, X. Zhou, Y. Gao, B. Zheng, F. Tang, and J. Huang. Recent progress in development of new sonosensitizers for sonodynamic cancer therapy. *Drug discovery today*, 19(4):502–509, 2014.

[82] D. Costley, C. Mc Ewan, C. Fowley, A.P. McHale, J. Atchison, N. Nomikou, and J.F. Callan. Treating cancer with sonodynamic therapy: a review. *International Journal of Hyperthermia*, 31(2):107–117, 2015.

[83] N.L. Oleinick, R.L. Morris, and I. Belichenko. The role of apoptosis in response to photodynamic therapy: what, where, why, and how. *Photochemical & Photobiological Sciences*, 1(1):1–21, 2002.

[84] D. Kessel, J. Lo, R.l Jeffers, J.B. Fowlkes, and C. Cain. Modes of photodynamic vs. sonodynamic cytotoxicity. *Journal of Photochemistry and Photobiology B: Biology*, 28(3):219–221, 1995.

[85] M. Redza-Dutordoir and D.A. Averill-Bates. Activation of apoptosis signalling pathways by reactive oxygen species. *Biochimica et Biophysica Acta (BBA)-Molecular Cell Research*, 1863(12):2977–2992, 2016.

[86] P. Tharkar, R. Varanasi, W.S.F. Wong, C.T. Jin, and W. Chrzanowski. Nano-enhanced drug delivery and therapeutic ultrasound for cancer treatment and beyond. *Frontiers in Bioengineering and Biotechnology*, 7:324, 2019.

[87] A. Jain, A.and Tiwari, A. Verma, and S.K. Jain. Ultrasound-based triggered drug delivery to tumors. *Drug delivery and translational research*, 8(1):150–164, 2018.

[88] K. Entzian and A. Aigner. Drug delivery by ultrasound-responsive nanocarriers for cancer treatment. *Pharmaceutics*, 13(8):1135, 2021.

[89] S.M. Asil, J. Ahlawat, G.G. Barroso, and M. Narayan. Nanomaterial based drug delivery systems for the treatment of neurodegenerative diseases. *Biomaterials science*, 8(15):4109–4128, 2020.

[90] A. Bisazza, P. Giustetto, I. Rolfo, A.and Caniggia, S. Balbis, C. Guiot, and R. Cavalli. Microbubble-mediated oxygen delivery to hypoxic tissues as a new therapeutic device. In *2008 30th Annual International Conference of the IEEE Engineering in Medicine and Biology Society*, pages 2067–2070. IEEE, 2008.

[91] C. Magnetto, M. Prato, A. Khadjavi, G. Giribaldi, I. Fenoglio, J. Jose, G.R. Gulino, F. Cavallo, E. Quaglino, E. Benintende, et al. Ultrasound-activated decafluoropentane-cored and chitosan-shelled nanodroplets for oxygen delivery to hypoxic cutaneous tissues. *RSC advances*, 4(72):38433–38441, 2014.

[92] X. Song, L. Feng, C. Liang, K. Yang, and Z. Liu. Ultrasound triggered tumor oxygenation with oxygen-shuttle nanoperfluorocarbon to overcome hypoxia-associated resistance in cancer therapies. *Nano letters*, 16(10):6145–6153, 2016.

[93] M. Xavierselvan, J. Cook, J. Duong, N. Diaz, K. Homan, and S. Mallidi. Photoacoustic nanodroplets for oxygen enhanced photodynamic therapy of cancer. *Photoacoustics*, 25:100306, 2022.

[94] E.G. Schutt, D.H. Klein, R.M. Mattrey, and J.G. Riess. Injectable microbubbles as contrast agents for diagnostic ultrasound imaging: the key role of perfluorochemicals. *Angewandte Chemie International Edition*, 42(28):3218–3235, 2003.

[95] H. Lea-Banks, S.K. Wu, H. Lee, and K. Hynynen. Ultrasound-triggered oxygen-loaded nanodroplets enhance and monitor cerebral damage from sonodynamic therapy. *Nanotheranostics*, 6(4):376, 2022.

[96] M. Prato, C. Magnetto, J. Jose, A. Khadjavi, F. Cavallo, E. Quaglino, A. Panariti, I. Rivolta, E. Benintende, G. Varetto, M. Argenziano, A. Troia, R. Cavalli, and C. Guiot. 2h, 3h-decafluoropentane-based nanodroplets: new perspectives for oxygen delivery to hypoxic cutaneous tissues. *PLoS One*, 10(3):e0119769, 2015.

[97] J.J. Kwan, M. Kaya, M.A. Borden, and P.A. Dayton. Theranostic oxygen delivery using ultrasound and microbubbles. *Theranostics*, 2(12):1174, 2012.

[98] R. Cavalli, A. Bisazza, P. Giustetto, A Civra, D. Lembo, G Trotta, C. Guiot, and M. Trotta. Preparation and characterization of dextran nanobubbles for oxygen delivery. *Int. J. Pharm.*, 381(2):160–165, 2009.

[99] R. Cavalli, A. Bisazza, A. Rolfo, S. Balbis, D. Madonnaripa, I. Caniggia, and C. Guiot. Ultrasound-mediated oxygen delivery from chitosan nanobubbles. *Int. J. Pharm.*, 378(1-2):215–217, 2009.

[100] EP Stride and CC Coussios. Cavitation and contrast: the use of bubbles in ultrasound imaging and therapy. *P I MECH ENG E-J PRO*, 224(2):171–191, 2010.

[101] P.S. Sheeran, S.H. Luois, L.B. Mullin, T.O. Matsunaga, and P.A. Dayton. Design of ultrasonically-activatable nanoparticles using low boiling point perfluorocarbons. *Biomaterials*, 33(11):3262–3269, 2012.

[102] O.D. Kripfgans, J .B. Fowlkes, D.L. Miller, O.P. Eldevik, and P.L. Carson. Acoustic droplet vaporization for therapeutic and diagnostic applications. *Ultrasound in medicine & biology*, 26(7):1177–1189, 2000.

[103] E. Stride, T. Segers, G. Lajoinie, S. Cherkaoui, T. Bettinger, M. Versluis, and M. Borden. Microbubble agents: New directions. *Ultrasound in medicine & biology*, 46(6):1326–1343, 2020.

[104] E.A. Neppiras. Acoustic cavitation. *Physics Reports*, 61(3):159–251, 1980.

[105] W.G. Pitt, R.N. Singh, K.X. Perez, G.A. Husseini, and D.R. Jack. Phase transitions of perfluorocarbon nanoemulsion induced with ultrasound: A mathematical model. *Ultrasonics sonochemistry*, 21(2):879–891, 2014.

[106] T. Lacour, M. Guédra, T. Valier-Brasier, and F. Coulouvrat. A model for acoustic vaporization dynamics of a bubble/droplet system encapsulated within a hyperelastic shell. *The Journal of the Acoustical Society of America*, 143(1):23–37, 2018.

[107] P.S. Sheeran, N. Matsuura, M.A. Borden, R. Williams, T.O. Matsunaga, P.N. Burns, and P.A. Dayton. Methods of generating submicrometer phase-shift perfluorocarbon droplets for applications in medical ultrasonography. *IEEE transactions on ultrasonics, ferroelectrics, and frequency control*, 64(1):252–263, 2016.

[108] C. Mannaris, C. Yang, D. Carugo, J. Owen, J.Y. Lee, S. Nwokeoha, A. Seth, and B.M. Teo. Acoustically responsive polydopamine nanodroplets: a novel theranostic agent. *Ultrasonics sonochemistry*, 60:104782, 2020.

[109] A.L.Y. Kee and B.M. Teo. Biomedical applications of acoustically responsive phase shift nanodroplets: Current status and future directions. *Ultrasonics sonochemistry*, 56:37–45, 2019.

[110] S. Ferri, Q. Wu, A. De Grazia, A. Polydorou, J.P. May, E. Stride, N.D. Evans, and D. Carugo. Tailoring the size of ultrasound responsive lipid-shelled nanodroplets by varying production parameters and environmental conditions. *Ultrasonics sonochemistry*, 73:105482, 2021.

[111] P.S. Sheeran, V.P. Wong, S. Luois, R.J. McFarland, W.D. Ross, S. Feingold, T.O. Matsunaga, and P.A. Dayton. Decafluorobutane as a phase-change contrast agent for low-energy extravascular ultrasonic imaging. *Ultrasound in medicine & biology*, 37(9):1518–1530, 2011.

[112] P.S. Sheeran, S. Luois, P.A. Dayton, and T.O. Matsunaga. Formulation and acoustic studies of a new phase-shift agent for diagnostic and therapeutic ultrasound. *Langmuir*, 27(17):10412–10420, 2011.

[113] O. Couture, P.D. Bevan, E. Cherin, K. Cheung, P.N. Burns, and F.S. Foster. Investigating perfluorohexane particles with high-frequency ultrasound. *Ultrasound in medicine & biology*, 32(1):73–82, 2006.

[114] P. Zhang and T. Porter. An in vitro study of a phase-shift nanoemulsion: a potential nucleation agent for bubble-enhanced hifu tumor ablation. *Ultrasound in medicine & biology*, 36(11):1856–1866, 2010.

[115] H. Xu, B.W. Zeiger, and K.S. Suslick. Sonochemical synthesis of nanomaterials. *Chemical Society Reviews*, 42(7):2555–2567, 2013.

[116] E.M. Strohm, I. Gorelikov, N. Matsuura, and M.C. Kolios. Modeling photoacoustic spectral features of micron-sized particles. *Physics in Medicine & Biology*, 59(19):5795, 2014.

[117] J.A. Kopechek, P. Zhang, M.T. Burgess, and T.M. Porter. Synthesis of phase-shift nanoemulsions with narrow size distributions for acoustic droplet vaporization and bubble-enhanced ultrasound-mediated ablation. *JoVE (Journal of Visualized Experiments)*, (67):e4308, 2012.

[118] P.A Mountford, S.R Sirsi, and M.A. Borden. Condensation phase diagrams for lipid-coated perfluorobutane microbubbles. *Langmuir*, 30(21):6209–6218, 2014.

[119] T.D. Martz, D. Bardin, P.S. Sheeran, A.P. Lee, and P.A. Dayton. Microfluidic generation of acoustically active nanodroplets. *Small*, 8(12):1876–1879, 2012.

[120] R. Melich, P. Bussat, L. Morici, A. Vivien, E. Gaud, T. Bettinger, and S. Cherkaoui. Microfluidic preparation of various perfluorocarbon nanodroplets: Characterization and determination of acoustic droplet vaporization (adv) threshold. *International Journal of Pharmaceutics*, 587:119651, 2020.

[121] S. Khizar, N. Zine, A. Errachid, N. Jaffrezic-Renault, and A. Elaissari. Microfluidic-based nanoparticle synthesis and their potential applications. *Electrophoresis*, 43(7-8):819–838, 2022.

[122] E. Strohm, M. Rui, I. Gorelikov, N. Matsuura, and M. Kolios. Vaporization of perfluorocarbon droplets using optical irradiation. *Biomedical Optics Express*, 2(6):1432–1442, 2011.

[123] Ş.H. Şanlıer, G. Ak, H. Yılmaz, Ü. F. Ünal, A.and Bozkaya, G. Tanıyan, Y. Yıldırım, and G. Y Türkyılmaz. Development of ultrasound-triggered and magnetic-targeted nanobubble system for dual-drug delivery. *J. Pharm. Sci.*, 108(3):1272–1283, 2019.

[124] Z. Teng, R. Wang, Y. Zhou, M. Kolios, Y. Wang, N. Zhang, Z. Wang, Y. Zheng, and G. Lu. A magnetic droplet vaporization approach using perfluorohexane-encapsulated magnetic mesoporous particles for ultrasound imaging and tumor ablation. *Biomaterials*, 134:43–50, 2017.

[125] J. Wang, W. Zhang, Z. Xie, X. Wang, Y. Luo, W. Jiang, Y. Liu, Z. Wang, H. Ran, W. Song, et al. Magnetic nanodroplets for enhanced deep penetration of solid tumors and simultaneous magnetothermal-sensitized immunotherapy against tumor proliferation and metastasis. *Advanced Healthcare Materials*, page 2201399, 2022.

[126] S.A. Ansari, E. Ficiarà, F. D'Agata, R. Cavalli, L. Nasi, F. Casoli, F. Albertini, and C. Guiot. Step-by-step design of new theranostic nanoformulations: Multifunctional nanovectors for radio-chemo-hyperthermic therapy under physical targeting. *Molecules*, 26(15):4591, 2021.

[127] E. Ficiarà, S.A. Ansari, M. Argenziano, L. Cangemi, C. Monge, R. Cavalli, and F. D'Agata. Beyond oncological hyperthermia: physically drivable magnetic nanobubbles as novel multipurpose theranostic carriers in the central nervous system. *Molecules*, 25(9):2104, 2020.

[128] S. Zullino, M. Argenziano, S. Ansari, R. Ciprian, L. Nasi, F. Albertini, R. Cavalli, and C. Guiot. Superparamagnetic oxygen-loaded nanobubbles to enhance tumor oxygenation during hyperthermia. *Frontiers in Pharmacology*, 10:1001, 2019.

[129] A. Khadjavi, I. Stura, M. Prato, V. G. Minero, A. Panariti, I. Rivolta, G. R. Gulino, F. Bessone, G. Giribaldi, E. Quaglino, et al. 'in vitro','in vivo'and 'in silico'investigation of the anticancer effectiveness of oxygen-loaded chitosan-shelled nanodroplets as potential drug vector. *Pharm. Res.*, 35.

[130] A. Lipovsky, Z. Tzitrinovich, H. Friedmann, G. Applerot, A. Gedanken, and R. Lubart. Epr study of visible light-induced ros generation by nanoparticles of zno. *The Journal of Physical Chemistry C*, 113(36):15997–16001, 2009.

[131] H. Mirzaei and M. Darroudi. Zinc oxide nanoparticles: Biological synthesis and biomedical applications. *Ceramics International*, 43(1):907–914, 2017.

[132] V. Cauda, R. Gazia, S. Porro, S. Stassi, G. Canavese, I. Roppolo, and A. Chiolerio. Nanostructured zno materials: Synthesis, properties and applications. *Handbook of Nanomaterials Properties*, pages 137–177, 2014.

[133] K. Yasui. *Fundamentals of Acoustic Cavitation and Sonochemistry*, pages 1–29. Springer Netherlands, 2011.

[134] J.D.N. Cheeke. *Fundamentals and applications of ultrasonic waves*, pages 128–138. Boca Raton, FL, 2002.

[135] H. Maris and S. Balibar. Negative pressures and cavitation in liquid helium. *Physics Today*, 53(2):29, 2000.

[136] K.S. Suslick and D.J. Flannigan. Inside a collapsing bubble: sonoluminescence and the conditions during cavitation. *Annu. Rev. Phys. Chem.*, 59:659–683, 2008.

[137] R. Pecha and B. Gompf. Microimplosions: cavitation collapse and shock wave emission on a nanosecond time scale. *Physical review letters*, 84(6):1328, 2000.

[138] K.R. Weninger, C.G. Camara, and S.J. Putterman. Observation of bubble dynamics within luminescent cavitation clouds: Sonoluminescence at the nano-scale. *Physical Review E*, 63(1):016310, 2000.

[139] J. Holzfuss, M. Rüggeberg, and A. Billo. Shock wave emissions of a sonoluminescing bubble. *Physical review letters*, 81(24):5434, 1998.

[140] P. Riesz and T. Kondo. Free radical formation induced by ultrasound and its biological implications. *Free Radical Biology and Medicine*, 13(3):247–270, 1992.

[141] D.H. Peregrine. The acoustic bubble. by tg leighton. academic press, 1994. 613 pp.£ 95. isbn 0-12-441920-8. *Journal of Fluid Mechanics*, 272:407–408, 1994.

[142] R.E. Apfel. The role of impurities in cavitation-threshold determination. *The Journal of the Acoustical Society of America*, 48(5B):1179–1186, 1970.

[143] K. Yasui. Influence of ultrasonic frequency on multibubble sonoluminescence. *The Journal of the Acoustical Society of America*, 112(4):1405–1413, 2002.

[144] N. Bremond, M. Arora, S.M. Dammer, and D. Lohse. Interaction of cavitation bubbles on a wall. *Physics of fluids*, 18(12):121505, 2006.

[145] M.L. Calvisi, O. Lindau, J.R. Blake, and A.J. Szeri. Shape stability and violent collapse of microbubbles in acoustic traveling waves. *Physics of Fluids*, 19(4):047101, 2007.

[146] W. Wang, W. Chen, M. Lu, and R. Wei. Bubble oscillations driven by aspherical ultrasound in liquid. *The Journal of the Acoustical Society of America*, 114(4):1898–1904, 2003.

[147] F.R. Young. *Cavitation*. World Scientific, 1999.

[148] J. Lee, T. Tuziuti, K. Yasui, S. Kentish, F. Grieser, M. Ashokkumar, and Y. Iida. Influence of surface-active solutes on the coalescence, clustering, and fragmentation of acoustic bubbles confined in a microspace. *The Journal of Physical Chemistry C*, 111(51):19015–19023, 2007.

[149] R. Löfstedt, B.P. Barber, and S.J. Putterman. Toward a hydrodynamic theory of sonoluminescence. *Physics of Fluids A: Fluid Dynamics*, 5(11):2911–2928, 1993.

[150] W. Lauterborn and T. Kurz. Physics of bubble oscillations. *Reports on progress in physics*, 73(10):106501, 2010.

[151] L. Rayleigh. Viii. on the pressure developed in a liquid during the collapse of a spherical cavity. *The London, Edinburgh, and Dublin Philosophical Magazine and Journal of Science*, 34(200):94–98, 1917.

[152] M.S. Plesset and A. Prosperetti. Bubble dynamics and cavitation. *Annual review of fluid mechanics*, 9(1):145–185, 1977.

[153] W. Lauterborn. Numerical investigation of nonlinear oscillations of gas bubbles in liquids. *The Journal of the Acoustical Society of America*, 59(2):283–293, 1976.

[154] M.S. Plesset. The dynamics of cavitation bubbles. 1949.

[155] B.E. Noltingk and E.A. Neppiras. Cavitation produced by ultrasonics. *Proceedings of the Physical Society. Section B*, 63(9):674, 1950.

[156] F.R. Gilmore. The growth or collapse of a spherical bubble in a viscous compressible liquid. 1952.

[157] J.B. Keller and M. Miksis. Bubble oscillations of large amplitude. *The Journal of the Acoustical Society of America*, 68(2):628–633, 1980.

[158] S. Popinet and S. Zaleski. Bubble collapse near a solid boundary: a numerical study of the influence of viscosity. *Journal of fluid mechanics*, 464:137–163, 2002.

[159] M.H. Safar. Comment on papers concerning rectified diffusion of cavitation bubbles. *The Journal of the Acoustical Society of America*, 43(5):1188–1189, 1968.

[160] F.G. Blake. The onset of cavitation in liquids. *Tech. Memo.*, (12), 1949.

[161] L.A. Crum. Measurements of the growth of air bubbles by rectified diffusion. *The Journal of the Acoustical Society of America*, 68(1):203–211, 1980.

[162] A. Eller and H.G. Flynn. Rectified diffusion during nonlinear pulsations of cavitation bubbles. *The Journal of the Acoustical Society of America*, 37(3):493–503, 1965.

[163] M.M. Fyrillas and A.J. Szeri. Dissolution or growth of soluble spherical oscillating bubbles. *Journal of Fluid Mechanics*, 277:381–407, 1994.

[164] M.M. Fyrillas and A.J. Szeri. Surfactant dynamics and rectified diffusion of microbubbles. *Journal of Fluid Mechanics*, 311:361–378, 1996.

[165] M. Minnaert XVI. On musical air-bubbles and the sounds of running water, london edinburgh dublin philos. mag. *J. Sci*, 16:235–248, 1933.

[166] R.V. Chaudhari and H. Hofmann. Coalescence of gas bubbles in liquids. *Reviews in Chemical Engineering*, 10(2):131–190, 1994.

[167] D. Sunartio, M. Ashokkumar, and F. Grieser. Study of the coalescence of acoustic bubbles as a function of frequency, power, and water-soluble additives. *Journal of the American Chemical Society*, 129(18):6031–6036, 2007.

[168] E.B. Flint and K.S. Suslick. The temperature of cavitation. *Science*, 253(5026):1397–1399, 1991.

[169] M. Ashokkumar and T.J. Mason. Sonochemistry. *Kirk-Othmer Encyclopedia of Chemical Technology*, 2000.

[170] K. Makino, M. M Mossoba, and P. Riesz. Formation of and in aqueous solutions by ultrasound using clinical equipment. *Radiation research*, 96(2):416–421, 1983.

[171] R.E. Apfel. Activatable infusable dispersions containing drops of a superheated liquid for methods of therapy and diagnosis, November 24 1998. US Patent 5,840,276.

[172] M. Zhang, M.L. Fabiilli, K.J. Haworth, F. Padilla, S.D. Swanson, O.D. Kripfgans, P.L. Carson, and J.B. Fowlkes. Acoustic droplet vaporization for enhancement of thermal ablation by high intensity focused ultrasound. *Academic radiology*, 18(9):1123–1132, 2011.

[173] K. Kawabata, N. Sugita, H. Yoshikawa, T. Azuma, and S. Umemura. Nanoparticles with multiple perfluorocarbons for controllable ultrasonically induced phase shifting. *Japanese journal of applied physics*, 44(6S):4548, 2005.

[174] V.P. Carey. *Liquid-vapor phase-change phenomena: an introduction to the thermophysics of vaporization and condensation processes in heat transfer equipment*. CRC Press, 2020.

[175] R.L. Scott and P.H. van Konynenburg. Static properties of solutions. van der waals and related models for hydrocarbon mixtures. *Discussions of the Faraday society*, 49:87–97, 1970.

[176] C.Y. Lin and W.G. Pitt. Acoustic droplet vaporization in biology and medicine. *BioMed research international*, 2013, 2013.

[177] L.N. Long, M.M. Micci, and B.C. Wong. Molecular dynamics simulations of droplet evaporation. *Computer Physics Communications*, 96(2-3):167–172, 1996.

[178] J.N. Israelachvili. *Intermolecular and surface forces*. Academic press, 2011.

[179] F. Reif. *Fundamentals of statistical and thermal physics*. Waveland Press, 2009.

[180] R. Wiebe and V.L. Gaddy. The solubility of carbon dioxide in water at various temperatures from 12 to 40 and at pressures to 500 atmospheres. critical phenomena. *Journal of the American Chemical Society*, 62(4):815–817, 1940.

[181] J.J. Kwan and M.A. Borden. Lipid monolayer dilatational mechanics during microbubble gas exchange. *Soft Matter*, 8(17):4756–4766, 2012.

[182] G.W. Thomson. The antoine equation for vapor-pressure data. *Chemical reviews*, 38(1):1–39, 1946.

[183] R.H. Dieck. *Measurement uncertainty: methods and applications*. ISA, 2007.

[184] L. Kirkup and R.B. Frenkel. *An introduction to uncertainty in measurement: using the GUM (guide to the expression of uncertainty in measurement)*. Cambridge University Press, 2006.

[185] International Organization for Standardization. *Guide to the Expression of Uncertainty in Measurement*. 1st ed., Geneva, 1993.

[186] BIPM, IEC, IFCC, ILAC, ISO, IUPAC, IUPAP, and OIML. International vocabulary of metrology - basic and general concepts and associated terms (vim). http://web.archive.org/web/20080207010024/http://www.808multimedia.com/winnt/kernel.htm, 2012.

[187] A. Troia, R. Cuccaro, and A. Schiavi. Independent tuning of acoustic and mechanical properties of phantoms for biomedical applications of ultrasound. *Biomedical Physics & Engineering Express*, 3(2):025011, 2017.

[188] J. Frohly, S. Labouret, C. Bruneel, I. Looten-Baquet, and R. Torguet. Ultrasonic cavitation monitoring by acoustic noise power measurement. *The Journal of the Acoustical Society of America*, 108(5):2012–2020, 2000.

[189] C A Schneider, W S Rasband, and K W Eliceiri. Nih image to imagej: 25 years of image analysis. *Nat. methods*, 9(7):671–675, 2012.

[190] A.E. Dunn, D.J. Dunn, M. Lim, C. Boyer, and N.T.K. Thanh. Recent developments in the design of nanomaterials for photothermal and magnetic hyperthermia induced controllable drug delivery. *Nanoscience*, 2:225–254, 2013.

[191] D. Prokopiou, M. Pissas, G. Fibbi, F. Margheri, B. Kalska-Szostko, G. Papanastasiou, M. Jansen, J. Wang, A. Laurenzana, and E. Efthimiadou. Synthesis and characterization of modified magnetic nanoparticles as theranostic agents: In vitro safety assessment in healthy cells. *Toxicology in Vitro*, 72:105094, 2021.

[192] Y. Huang, J.C. Hsu, H. Koo, and D.P. Cormode. Repurposing ferumoxytol: Diagnostic and therapeutic applications of an fda-approved nanoparticle. *Theranostics*, 12(2):796, 2022.

[193] R.R. Wildeboer, P. Southern, and Q.A. Pankhurst. On the reliable measurement of specific absorption rates and intrinsic loss parameters in magnetic hyperthermia materials. *Journal of Physics D: Applied Physics*, 47(49):495003, 2014.

[194] S. Tong, C.A. Quinto, L. Zhang, P. Mohindra, and G. Bao. Size-dependent heating of magnetic iron oxide nanoparticles. *ACS nano*, 11(7):6808–6816, 2017.

[195] E.C. Abenojar, S. Wickramasinghe, J. Bas-Concepcion, and A.C.S. Samia. Structural effects on the magnetic hyperthermia properties of iron oxide nanoparticles. *Progress in Natural Science: Materials International*, 26(5):440–448, 2016.

[196] N.A. Usov, M.S. Nesmeyanov, E.M. Gubanova, and N.B. Epshtein. Heating ability of magnetic nanoparticles with cubic and combined anisotropy. *Beilstein Journal of Nanotechnology*, 10(1):305–314, 2019.

[197] D. Cabrera, J. Camarero, D. Ortega, and F.J. Teran. Influence of the aggregation, concentration, and viscosity on the nanomagnetism of iron oxide nanoparticle colloids for magnetic hyperthermia. *Journal of Nanoparticle Research*, 17(3):121, 2015.

[198] G. Salas, J. Camarero, D. Cabrera, He. Takacs, M. Varela, R. Ludwig, H. Dahring, I. Hilger, R. Miranda, M.d.P. Morales, et al. Modulation of magnetic heating via dipolar magnetic interactions in monodisperse and crystalline iron oxide nanoparticles. *The Journal of Physical Chemistry C*, 118(34):19985–19994, 2014.

[199] G. Barrera, P. Allia, and P. Tiberto. Dipolar interactions among magnetite nanoparticles for magnetic hyperthermia: a rate-equation approach. *Nanoscale*, 13(7):4103–4121, 2021.

Appendix A

Fe_3O_4 Nanoparticles

In the biomedical research field iron oxide nanoparticles are subjected to strong interest and intense studies as magnetic nanomaterials thanks to their promising properties, such as chemical stability and high biocompatibility in terms of safety and body clearance [190–192]. Their main application relies on taking advantaged of the interaction between NPs and an AC magnetic field, resulting in the liberation of thermal energy caused by hysteresis losses. The ability of NPs to produce heat is usually expressed by means the specific loss power (SLP), that represents the power dissipated per unit mass [193] and is strictly dependent on material properties, dimensions, shape and state of aggregation [194–199].
Fe_3O_4 NPs used in this work have been characterized in terms of structural, morphological and dimensional properties through XRD, TEM imaging and DLS characterization. Results are shown in Figure A.1.

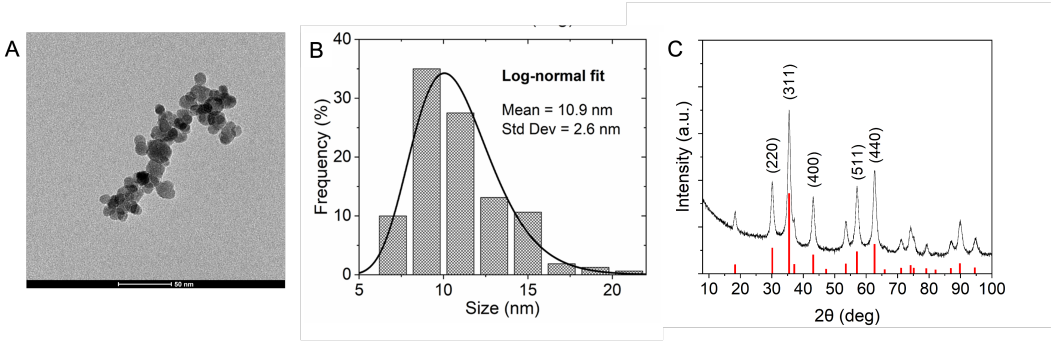

Fig. A.1 A) Representative TEM picture, B) size distribution (derived from statistics on TEM images), C) and XRD pattern of Fe_3O_4 NPs [10].

Figure A.1 A) depicts a representative TEM image of Fe_3O_4 NPs, showing a quasi-spherical shape of the particles and a strong uniformity in their sizes, as also demonstrated by the distribution reported in Figure A.1 B). XRD pattern is shown in Figure A.1 C) and reveals a crystalline phase with main diffraction peaks typical of the cubic spinel structure of magnetite.

Magnetic properties of the iron oxide NPs are shown in Figure A.2. The static hysteresis loop of dry sample measured at room temperature can be appreciated in Figure A.2 A), demonstrating the interacting superparamagnetic behavior of the nanoparticles. Figure A.2 B) shows the dynamic minor hysteresis loops at different

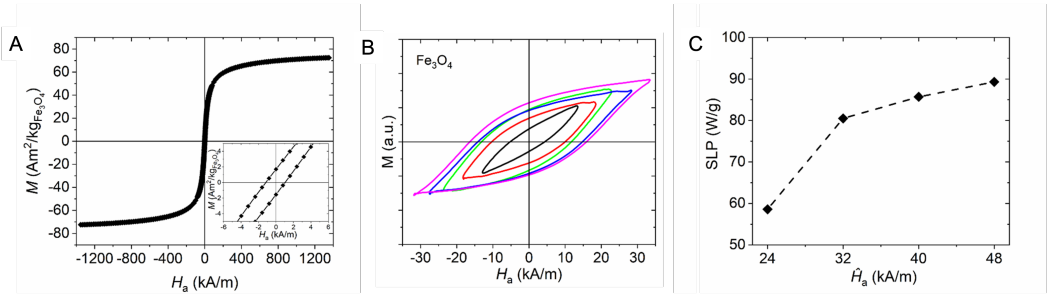

Fig. A.2 Magnetic properties of Fe_3O_4 nanoparticles are shown [10]. A) $M(H)$ curve of the nanoparticles at room temperature in dry form, with a portion of the hysteresis loop zoomed to highlight the coercivity. B) Dynamic minor hysteresis loops of the nanoparticles for a magnetic field with a peak amplitude $\hat{H}_a$ ranging from 13 kA m^{-1} to 32 kA m^{-1} and a fixed frequency of 69 kHz. C) Specific loss power (SLP) values for Fe_3O_4 NPs at different peak amplitudes of the AC magnetic field, with a fixed frequency of 100 kHz.

peak amplitudes of the AC magnetic field with a frequency of 69 kHz. It can be noticed how the dynamic hysteresis loop area is strictly dependent on the applied field amplitude, stronger the field wider the area. As a consequence, the heating efficiency results higher at 32 kA m^{-1}. Figure A.2 C) represents SLP values of nanoparticles at different peak amplitudes of AC magnetic field with a frequency of 100 kHz, confirming the direct proportionality between the peak amplitude and the effective release of energy in terms of heat.